AN ABSTRACT OF THE THESIS OF

Joshua A. Robinson for the degree of Master of Science in Nuclear Engineering presented on February 13, 2009.

Title: Design, Construction, and Characterization of a Prompt Gamma Activation Analysis Facility at the Oregon State University TRIGA® Reactor.

Abstract approved:

---

Michael R Hartman

In this work a prompt gamma neutron activation analysis (PGNAA) facility has been designed, built, and characterized at the Oregon State University TRIGA® reactor. PGNAA is a technique used to determine the presence and quantity of trace elements such as boron, hydrogen and carbon which are more difficult to detect with other neutron analysis methods. In PGNAA, isotopes are subjected to a neutron beam, resulting in the formation of an unstable compound nucleus. The compound nucleus immediately decays, producing a series of gamma-rays, whose energies are distinctive to each element. These gamma-rays are then measured using an HPGe detector to determine the elemental composition of the sample.

The measured thermal and epithermal neutron fluxes of the PGNAA facility at Oregon State University are $2.81 \times 10^{7} \pm 5.13 \times 10^{5}\ \mathrm{cm^{-2}\ s^{-1}}$, and $1.70 \times 10^{4} \pm 3.11 \times 10^{2}\mathrm{cm^{-2}\ s^{-1}}$ respectively. This gives the facility a cadmium ratio of 106. Measured detection limits for boron, chlorine, and potassium in SRM 1571 orchard leaf standard were, $5.6 \times 10^{-4}\ \mathrm{mg/g}$, $8.2 \times 10^{-2}\ \mathrm{mg/g}$, and $1.0\ \mathrm{mg/g}$ respectively. Also, the detection limit for hydrogen in high-density polyethylene is, $6.8 \times 10^{-2}\ \mathrm{mg/g}$ . Detection limits for additional elements are presented in this work.

# Design, Construction, and Characterization of a Prompt Gamma Activation Analysis Facility at the Oregon State University TRIGA® Reactor

by
Joshua A. Robinson

A THESIS

Submitted to

Oregon State University

in partial fulfillment of
the requirements for the
degree of

Master of Science

Presented February 13, 2009
Commencement June 2009

Master of Science thesis of Joshua A. Robinson
presented on February 13, 2009.

APROVED:

Major Professor, representing Nuclear Engineering

Head of the Department of Nuclear Engineering and Radiation Health Physics

Dean the of Graduate School

I Understand that my thesis will become part of the permanent collection of Oregon State University libraries. My signature below authorizes release of my thesis to any reader upon request.

Joshua A. Robinson, Author

# ACKNOWLEGMENTS

First I would like to thank Dr. Hartman for his guidance and help, and for giving me the opportunity to work on this project. It has been a joy to work with him and his knowledge in this area has been extremely valuable to this project. I would also like to thank Dr. Reese and the reactor operators for working with us and providing the necessary reactor time to install and characterize the facility.

I also am very thankful for my wife and all she has done at home taking care of our three small children (Joseph, Jonathan, and Daniel) while I have been working on this project. Her hard work and encouragement has been a very significant part of this project.

Lastly I would like to thank my Dad, and my brothers and sisters for their support and encouragement.

# TABLE OF CONTENTS

TABLE OF CONTENTS (Continued)

Page

# LIST OF FIGURES

# LIST OF FIGURES (Continued)

Figure Page

LIST OF FIGURES (Continued)

Figure Page

# LIST OF FIGURES (Continued)

Figure Page

# LIST OF FIGURES (Continued)

Figure Page

# LIST OF TABLES

# 1. Introduction

To expand the experimental capabilities of the Oregon State University TRIGA® Reactor, a facility for Prompt Gamma Neutron Activation Analysis (PGNAA) has been constructed. PGNAA is a nondestructive means of conducting elemental analysis on materials through neutron capture interactions. These neutron capture reactions produce compound nuclei in an excited state which de-excite almost instantaneously through the emission of gamma-rays of discreet energy. The energy spectrum of the gamma-rays is characteristic of the emitting nuclide, and the number of gamma rays at the specific energies is directly proportional to the quantity of the emitting isotope. There are in principle at least 80 elements which can be measured using PGNAA (G. L. Molnar, 2000). However since the detection limits for PGNAA are dependent on the capture cross sections of the specific elements the quantities of materials that are detectable will vary. PGNAA is especially useful for elements such as B, C, H, N, Ca, Cd, and Gd, which are hardly or not at all detectable using instrumental neutron activation analysis (INAA).

Prior to this facility, the only technique available to researchers at Oregon State University for nuclear analysis methods was INAA. INAA involves placing the samples of interest within or very close to the core of the reactor to expose them to very high neutron fields in order to produce radioactive product nuclei from the elements within the sample. The elements and amounts of the materials present are then determined by measuring the activity and the energy of decay gammas from the samples after the samples are removed from the core.

PGNAA has many advantages in comparison to INAA. As already mentioned above, there are many elements which do not produce significant amounts of activity to be practically measured using INAA. For most samples, PGNAA does not require any material removal or structural damage to the sample. Large pieces of materials such as pottery can be analyzed which would be too large to place in the reactor (Keisuke Sueki, 1996). There is practically none or very little radioactivity created within the samples. The results are generally much faster than INAA since measurements are taken in real-time during irradiation. There is no effect on the criticality of the reactor because the samples are irradiated outside of the bioshield of the reactor. In addition, the samples can be recounted to obtain better statistics since there is generally no damage to the samples. Whereas with INAA, the samples can be quite radioactive, depending upon the elements within the sample due to the much higher integrated flux exposure of the samples. The samples may be damaged due to much higher radiation exposure and heat associated with INAA. There are more limitations on what can be irradiated since they are placed within the core of the reactor due to size and possible reactivity additions to the reactor.

## 2. Theory of PGNAA

When a nucleus absorbs a neutron, a compound nucleus is formed with excitation energy equal to the binding energy ($BE_{neutron}$) of the neutron plus the kinetic energy of the neutron ($K_{Neutron}$). For about 80% of the stable nuclei the binding energy ranges from 6-10 MeV.

$$Excitation\ Energy = K_{Neutron} + BE_{Neutron} \qquad (2.1)$$

The excitation energy is rapidly shared among several nucleons followed by almost instantaneous decay (~$10^{-13}$ to $10^{-14}$ s) with the following possible reaction products.

1) Inelastic scattering, in which the neutron is emitted along with one or more gammas.
2) Radiative capture (n,$\gamma$), in which one or more capture gammas are emitted.
3) Similar to radiative capture except particles are emitted e.g., (n,$\alpha$), (n,p), (n,d), (n,n') …, (n,2n).
4) Fission or if enough energy spallation or evaporation.

(Binney, Fall 2006)

Of the four processes, radiative capture is the most common form of decay for compound nuclei formed by the absorption of a thermal neutron, and it is the fundamental process for PGNAA. Similar to the Bohr atomic theory for the atom, the nucleus has discrete energy levels. When the nucleus is in an excited state, the excitation energy is shared among several of the nucleons within the nucleus. These nucleons almost instantaneously go through a series of discreet energy transitions to get to the ground state. The transitions, starting at the capture state, are called primary

transitions, two or more transitions are called secondary transitions, and the final transitions reaching the ground state are called ground-state transitions. For each transition a gamma ray is released with energy equal to the energy of the transition ($E_T$) minus the recoil-energy ($E_R$) of the nucleus.

$$
\begin{aligned}
&E_\gamma = E_T - E_R \\
&\text{where,} \quad E_R = \frac{p^2}{2M} \\
&\qquad\qquad = \frac{E_\gamma^2}{2Mc^2} \ \text{since, } \mathrm{E}^2 = P^2c^2 + m^2c^4 \ \text{(Relitivistic relation between energy and momentum)} \\
&\text{and , } P = \text{Momentum, } M = \text{ mass of nucleus, and } c = \text{ speed of light.}
\end{aligned}
\tag{2.2}
$$

For radiative capture, the recoil energy can be as high as several keV for light elements but is typically less than 0.1% of the transition energy for most elements (Audi, 2003). Thus, as the nucleons return to the ground state, the energy released is discrete and characteristic of the nuclear energy levels within the nucleus, and since the energy levels of the nuclei are characteristically different for different element, the gammas released from radiative capture, which range from 50 keV to greater than 10 MeV, are distinct for differing elements.

For PGAA, it is important to consider radiative capture of both thermal neutrons and epithermal neutrons. For thermal neutrons, the energies of the capture states are very sharply defined due to low kinetic energy of the neutrons. Thus, the probability of decay through various transitions is essentially constant, and therefore the distribution of the gammas produced is essentially constant. This is important for determining information such as quantities of elements through PGNAA.

For epithermal neutrons, the increased kinetic energy of the neutrons results in greater excitation energy of the compound nucleus. For these higher exited states the transition to the ground state tends to be less-well defined, often resulting in an increase or change in the number of different energy gammas released due to de-excitation through different discrete energy levels of the nucleus. Thus for most applications, it is desirable to reduce the epithermal component of the beam as much as possible.

## 3. PGNAA Literature review (Development of PGNAA and PGNAA Facilities)

Neutron radioactive capture, which is the mechanism for PGNAA, was first observed when high energy gamma rays were measured during the irradiation of paraffin wax and liquid hydrogen using a Polonium-Beryllium neutron source (Lea, 1934). This was identified to be due to neutron capture followed by the emission of energy in the form of gamma rays equal to the binding energy of the nucleus (E. Amaldi, 1935). Since then, capture gamma rays have been studied extensively, resulting in the measurement of capture gamma rays for a large number of isotopes using gamma spectroscopy.

Prior to 1962, gamma spectroscopy was conducted primarily using magnetic gamma spectrometers, diffraction spectrometers, and scintillation spectrometers. Magnetic and diffraction spectrometers had a resolution of 0.3 to 0.8%, however they had a very low counting efficiency of $10^{-5}$ to $10^{-7}$ counts per gamma quanta incident on the spectrometer. This low efficiency resulted in the necessity to use large sample sizes of approximately 1 kg and place the samples next to the core of the reactor in order to obtain a higher neutron flux. On the other hand, scintillation spectrometers had a very good counting efficiency with a very poor resolution of ~8% for 0.7 MeV and 20 % for 0.1 MeV (L. V. Groshev, 1959). A compilation of the gamma rays measured for specific isotopes up until this time using these methods can be found in the following references, (L. V. Groshev, 1959), (G. A. Bartholomew, 1967), and (R. C. Greenwood, 1965). These studies contributed significantly to the knowledge of the nuclear energy levels, properties of isotopes, and provided much of the data necessary

for PGNAA. However these methods were not practical for PGNAA because of their poor counting efficiencies.

The first studies using PGNAA for elemental analysis were conducted using sodium iodide scintillation spectroscopy. Even though sodium iodide detectors provide good sensitivity their poor resolution made it difficult to differentiate between the different gamma energies, and the background. Hamermesh and Hummel solved the background problem by taking a series of four measurements (Hamermesh Bernard, 1952). The measurement taken were,

1. Source in—no cadmium in beam
2. Source in—cadmium in beam
3. Source out—no cadmium in beam
4. Source out—cadmium in beam

The first measurement taken in the beam provided the sample spectrum along with the background caused by fast neutrons and gammas from the core of the reactor. The second provided a spectrum with only the effect from fast neutrons and gamma rays with an added effect from the cadmium. The third provided a pure background spectrum. And the fourth provided a background with the effect of the cadmium. Thus, the sample spectrum alone was determined by combining the four spectra in the following order: 1-2-(3-4). Using this method, Hamermesh and Hummel were able to obtain spectra for the most prominent gamma energies for elements Z=17-30 and Z=45-57. Lussie and Brownlee (W. G. Lussie, 1965) showed that this method could be used successfully to measure moisture content in calcium nitrate from hydrogen

capture gamma rays, hydrogen content in paraffin and polystyrene, and could possibly be used for isotopic analysis of at least three of the four stable-iron isotopes.

The problems with this method were that it neglected delayed-gamma build up, and it assumed the beam was constant throughout the series of measurements. These problems were addressed by Isenhour and Morrison by using a modulation technique. This technique involved a cadmium chopper operating at about 1000 revolutions per second, and a detection system which was synchronized to record two spectra. One spectra was taken when the chopper was in the beam and another was taken when the chopper was out of the beam. The neutron source for this facility was extracted from a tangential beam port of a 100 kw Mark II Reactor at Cornell University. A collimator with boral and graphite was used to collimate the beam to 1.25 inches in diameter at the sample position. This facility was among the first PGNAA facilities using a collimated beam from a reactor. It had a thermal flux of $1.7\times10^{6}$ neutrons/cm$^{2}$-s (T. L. Isenhour, 1966).

Another early, reactor-based PGNAA facility was built at the University of Washington's 100 kW nuclear reactor (UWNR) (Lambard et. al.). This facility initially employed a sodium iodide detector and a beam chopper similar to one used by Isenhour and Morrison at Cornell University (T. L. Isenhour, 1966). The collimated beam in this facility was improved significantly by the use of a quartz filter to reduce the fast neutron and gamma component of the beam. Even though this facility had detection limits on the 100 ppm level for elements with large capture cross section such as boron and cadmium, it was limited by the poor resolution of the sodium iodide detector.

As mentioned above, one of the major limiting factors of the early PGNAA facilities was the resolution of the available detectors. This, however, changed when the first lithium drifted germanium [Ge(Li)] detectors were produced in 1962. These detectors had efficiencies of approximately 0.3-0.8%, as opposed to the sodium iodide detectors which were approximately 8-20%. One of the first applications of a Ge(Li) detector with a PGNAA facility was at the University of Washington Research reactor by Lambard and Isenhour who compared the results of two Ge(Li) detectors (a planer detector from Isotopes Inc., and a Coaxial from Ortec) to that of a NaI(Tl) detector (Lambar & Isenhour, 1968). The significantly better resolution which was obtained by using the Ge(Li), as opposed to the NaI(Tl) detector, made it possible to use PGNAA practically and efficiently for a much wider range of elements.

Since the implementation of Ge(Li) detector, PGNAA has been implemented successfully at over 40 research reactors throughout the world (Molnar, 2004). There are typically two approaches which have been taken as far as the sample and detector positioning with respect to the reactor. The simplest and most common involves collimating the neutron beam and bringing it outside the biological shield of the reactor. The detector is then surrounded by shielding and placed $90^{o}$ to the neutron beam with a flight path from the sample to the detector. A less common approach, which was implemented at the Los Alamos Omega West Reactor, involved placing the sample next to the core with a collimator used to extract the neutron capture gamma rays to the detector outside the biological shield (Jurney & Motz, 1966). The advantage of the later configuration is that the sample is exposed to a much higher neutron flux which produces a much higher capture gamma flux. However, since the

sample to detector distance is much greater, this added benefit is mostly canceled out by the geometric attenuation of the capture gamma rays. This method also has the disadvantage that depending on the type of sample, the sample may be damaged by the higher neutron flux.

Among some of the best PGNAA facilities are the state-of-the-art facilities at the National Institute of Standards and Technology (NIST), Budapest, and the University of Texas. The facilities at NIST include a thermal PGNAA facility and a cold PGNAA facility. The thermal PGNAA facility at NIST has a neutron beam which is extracted vertically from the NIST research reactor from a region within the $D_2O$ approximately 0.5m from the nearest fuel element (Anderson et. al., 1981). This facility was originally built in the late 1970's, and had a beam which was collimated through a series of lead, borated polyethylene, and $^6Li_2CO_3$ collimators. The resulting neutron beam in this facility had a measured thermal flux of $2 \times 10^8\,\mathrm{cm^{-2}\,s^{-1}}$ and a epithermal flux of $1.1 \times 10^5\mathrm{cm^{-2}\,s^{-1}}$ . The collimator, beam tubes, and sample chamber were all designed such that they could be filled with gas such as helium to eliminate gamma production from constituents of the air such as nitrogen and oxygen. The final beam stop was made of polystyrene doped with 2% natural $Li_2CO_3$ surrounded by welded steel plates to hold it in place. The detector used was a Ge(Li) detector which was surrounded by a NaI(Tl) detector for Compton suppression.

Since the initial installation of this facility, several changes have been made which greatly enhanced the detection capabilities. First, the reactor was upgraded from 10MW to 20MW in 1985 (Kapetka, Rowe, & Williams, 2005). Second and more significantly, was a major redesign of the facility which was completed in 2001

(Mackey et. al., 2004). Part of the redesign involved the addition of a sapphire crystal in the beam shutter, resulting in a reduction of a factor of 5 for the fast neutron fluence, a factor of 5-10 reduction in the low-energy gamma fluence, and only a factor of 1.13 reduction in the thermal neutron fluence. A new beam stop was built containing borated polyethylene, lead, and lithoflex (a $^{6}Li_2F$-doped polymer). Aluminum support structure was used to reduce the background from high energy gammas, which were produced by the steel in the original beam stop. The beam tubes, which were originally made of acrylic tubes, $Li_2CO_3$, and paraffin, and the sample chamber which was made of acrylic and $B_4C$ cast in polystyrene-polyester resin, were all replaced with aluminum lined with lithoflex. These changes were made primarily to reduce the background count rates for hydrogen and boron. The detector system was also replaced with a detector with higher efficiency and better resolution, and the NaI(Tl) detector used for Compton suppression was replaced with a Bismuth germinate (BGO) scintillation detector to eliminate gamma-rays from sodium and iodide. The reported thermal neutron flux for the new system was $3.0 \times 10^{8}$ $cm^{-2}$ $s^{-1}$ with epithermal flux of $1.1 \times 10^{5}$ $cm^{-2}$ $s^{-1}$ with a relatively uniform beam diameter of approximately 2.0 cm. Overall the sensitivities of the new instrument were 5-50% better than that of the old instrument.

The cold PGNAA facility at NIST utilizes a cold-neutron-source, which is produced in a vessel containing hydrogen near the core of the reactor and filtered through 127mm Be and 178mm single crystal Bi, both of which are cooled to 77K. The neutron beam which is essentially free of fast neutrons and gamma-rays, travels through a guide tube to the PGNAA station. The flux at the sample position measured

with Au foils is $1.5 \times 10^8\ \mathrm{cm}^{-2}\ \mathrm{s}^{-1}$ . The advantage of this facility over thermal PGNAA facilities is that it has higher sensitivities in part due to the higher absorption cross section and the lower background count rates due to the absences of fast neutron and gamma-rays in the beam.

The PGNAA facility at the University of Texas and the facility in Budapest have reported thermal neutron fluxes of $5.3 \times 10^6\ \mathrm{cm}^{-2}\ \mathrm{s}^{-1}$ and $5.0 \times 10^7\ \mathrm{cm}^{-2}\ \mathrm{s}^{-1}$ respectively (Revey et. al., 2004) (Belgya, Revay, & Molnar, 2004). The reactor at the University Texas is a 1.1 MW Mark II TRIGA® reactor, and the reactor at the Budapest facility is a 10 MW tank type light water cooled reactor (KFKI Atomic Energy Research Institute, 2000).

Of the four, the thermal PGNAA neutron facility at NIST was used as a guide for the design and construction of the PGNAA facility at Oregon State University. However, as far as neutron fluxes, the University of Texas facility was a better representation of expected fluxes since the reactor power and type are very similar to that of the 1.1 MW reactor at OSU.

# 4. Design and Analysis of Materials and components

## *4.1. Reactor and Beam Port #4 (Oregon State University, 2008)*

The Oregon State University reactor is a natural convection cooled 1 MW (licensed 1.1-MW) TRIGA® pool reactor. Until August 2008, the reactor core was fueled with high-enriched uranium/zirconium hydride fuel elements. In August 2008, the reactor was refueled with low-enriched uranium fuel. The core of the reactor is surrounded by a graphite reflector and is located near the bottom of a water-filled aluminum tank 6 ½ feet in diameter and 20 ½ feet deep which is shielded radial by 10.2 inches of graphite, 2 inches of lead, 1 ½ feet of water, and over 8 feet of concrete.

The Reactor is equipped with four beam ports which penetrate the reactor bioshield and reactor tank to the reflector region of the core. Beam port #1 and #2 are radial beam ports which terminate at the outer edge of the graphite reflector. Beam port # 3 is tangential to the outer edge of the core and is dedicated to a neutron radiography facility. Beam port #4 is a radial piercing beam port which penetrates through the graphite reflector and terminates at the outer edge of the reactor core as illustrated in Figure 4-1.

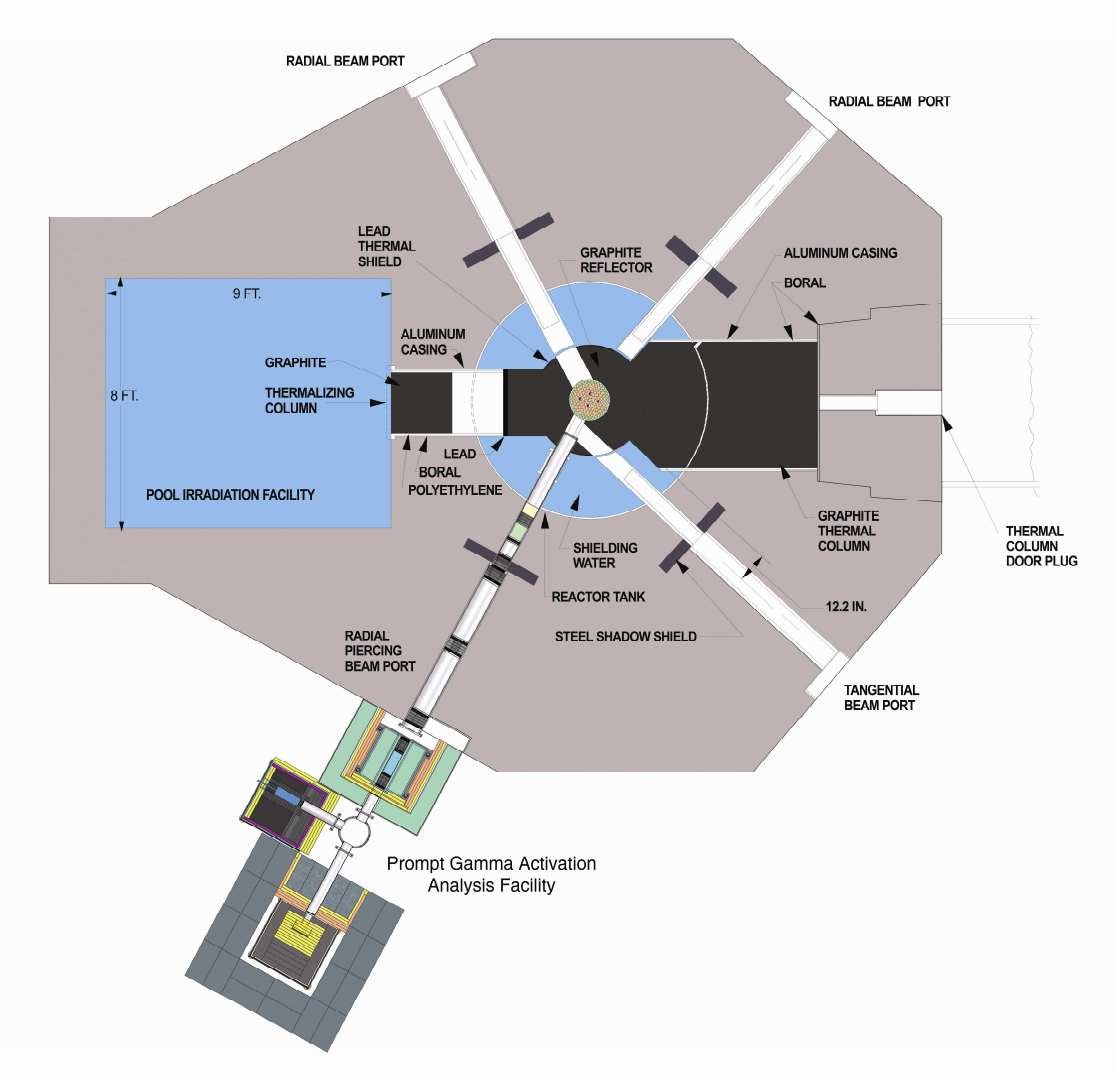


**Figure 4-1 Horizontal Section of the OSTR**

Due to water leakage within the graphite reflector, beam ports #1 and #2 have a reduced flux, leaving beam port #4 as the only available beam port suitable for the PGNAA Facility. As described above, beam port #4 is a piercing beam port which looks directly at the core. Beam port #4 is situated directly in front of element locations G-12 and G-13. Before the fuel change, these locations were occupied by fuel elements as shown in Figure 4-2, however during the fuel change these elements were replaced with graphite elements as shown in Figure 4-3. The advantage of this

beam port is that it has a very high thermal flux due to its proximity to core. However since it is situated directly in front of the core it also has a very high fast-neutron and gamma component streaming down the beam port as well. Thus, for the PGNAA facility it was important to include appropriate beam filtering to minimize the fast-neutrons and gammas while still maintaining a high thermal flux. The materials used for this are described in the following section.

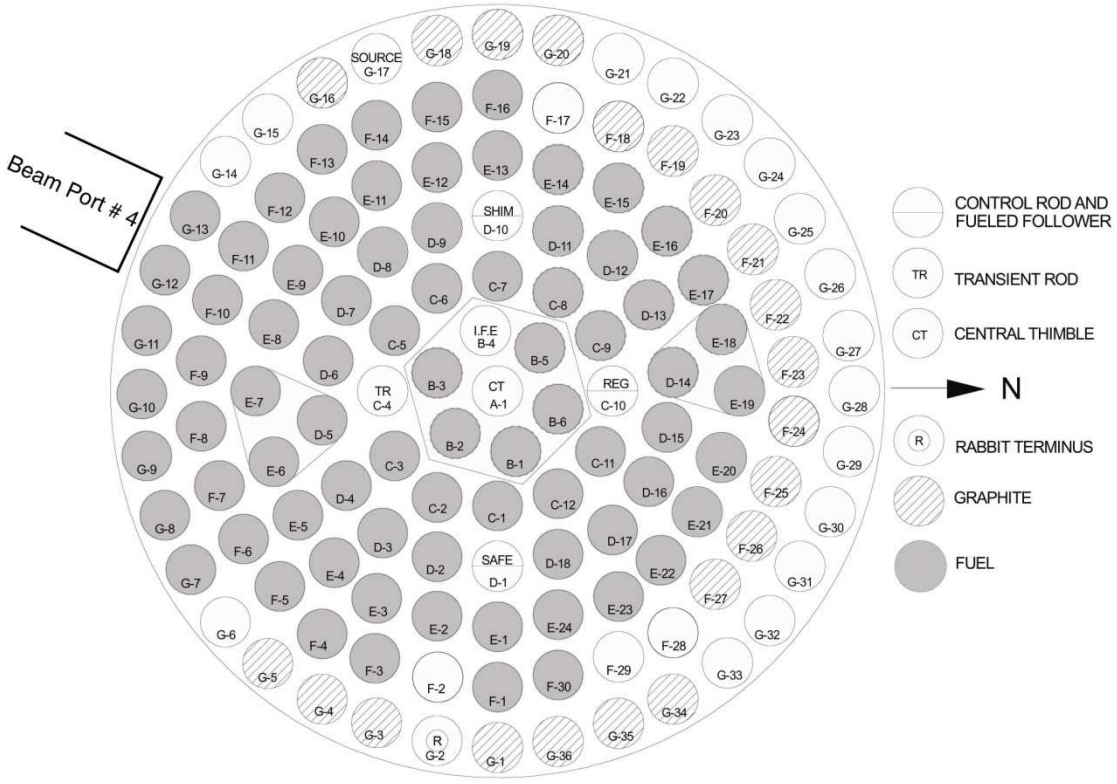


**Figure 4-2: HEU core configuration**

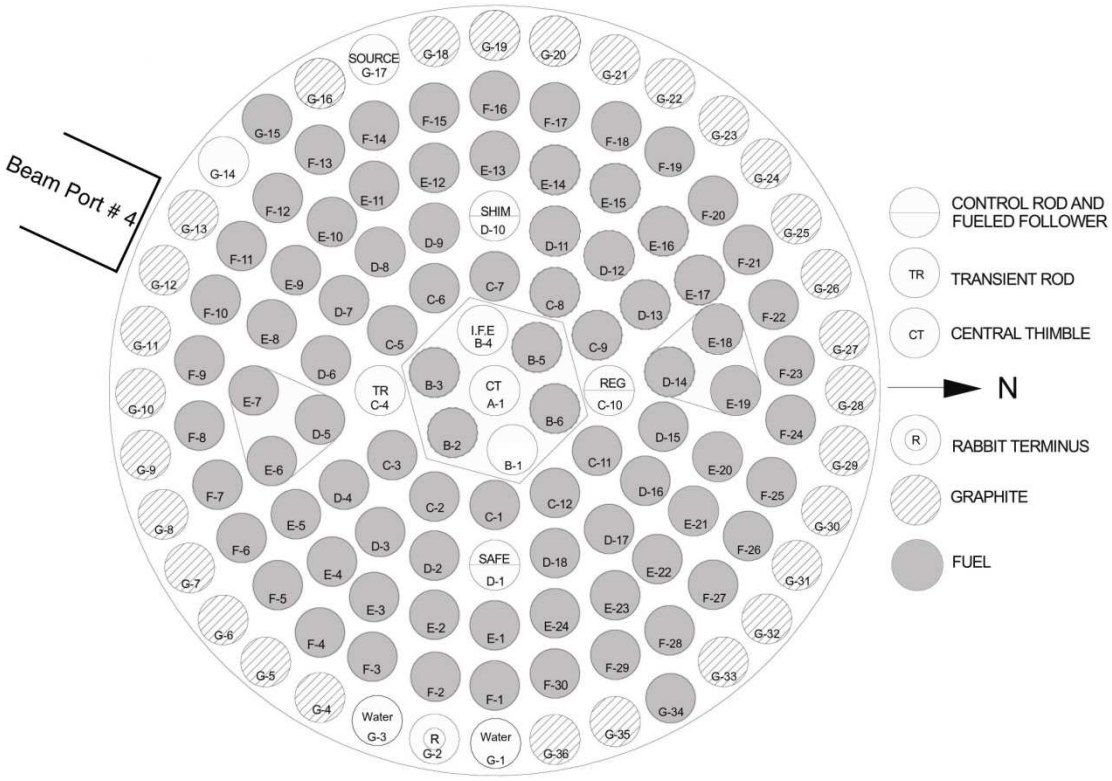


**Figure 4-3: LEU core configuration**

## *4.2. Description of facility*

The main components of the OSTR PGNAA facility are the collimator, the beam shutter, the sample chamber, the beam stop, and the high purity germanium detector housed inside of a large gamma and neutron shield, as illustrated in Figure 4-4.

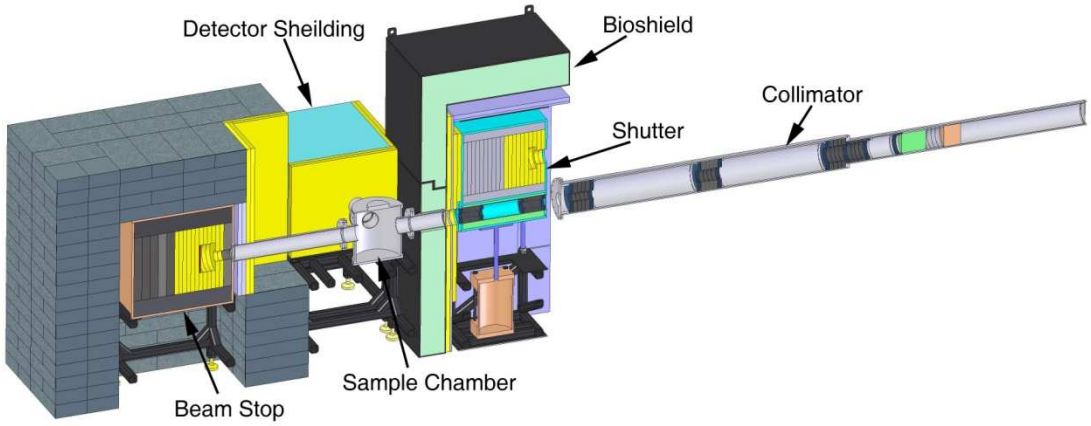


**Figure 4-4: Schematic illustration of PGNAA facility**

The collimator, which is installed in beam port #4 of the OSTR, consists of a welded aluminum tubing shell designed to slide into the beam port. The collimator contains lead and boral rings to collimate the neutron beam to a 2 cm uniform diameter within the center of the beam at the sample location, and a bismuth and sapphire filter, which serves to reduce the gamma and fast neutron component of the extracted neutron beam. There are also aluminum thin-windows on both ends of the collimator, allowing it be evacuated or back filled with gas such as helium to reduce gamma production from air within the collimator. The aluminum thin-window on the reactor side is welded in place while the aluminum thin-window on the exit side is

bolted on with an o-ring sealed flange, allowing easy access to the materials within the collimator.

Following the collimator is a shutter, which is a movable beam stop used to stop the neutron beam before it enters the sample chamber when the facility is not in use. This shutter is also surrounded by a biological shield, which greatly reduces the gamma and neutron levels emanating from the shutter and scatter from between the shutter and the collimator.

The sample chamber for the facility houses the sample while it is being irradiated. It is constructed entirely out of aluminum and allows the neutron beam to pass through the center of the chamber with very little interaction with materials other than those in the sample of interest. The sample chamber is also designed to allow for a clear path from the sample to the detector at an angle of $90^{o}$ to the incoming beam.

Since for PGNAA, the sample is counted while it is being irradiated, it is important that the high-purity germanium detector be well shielded from radiation other than those photons created by neutron capture interactions within the sample. Equally important is that the detector be as close to the sample as possible to increase the geometric efficiency. These two constraints require a tradeoff between efficiency and background levels around the detector. For this facility, the detector is placed approximately 60 cm from the sample with a large amount of borated polyethylene and lead surrounding the detector.

The final component of the facility is the beam stop, which is used to stop the beam when the shutter is open. The design of this beam stop is very similar to the shutter. Both beam stops were modeled in Monte Carlo N-Particle Transport Code (MCNP) to

get approximate shielding configurations within the beam stop (Los Alamos National Laboratory, 2003).

All of the components in the facility which house the neutron beam, with the exception of the beam stops, are designed such that they can be evacuated or back-filled with helium to reduce neutron interactions with constituents of the air such as nitrogen. These interactions would increase background levels around the facility and therefore decrease the signal-to-noise ratio of the detector.

### *4.3. Material preparations*

Within both the beam stop and the detector shielding there is a lithium fluoride disk. These disks are used to reduce the production of neutron capture gamma rays from the boron in the surrounding polyethylene, and to protect the detector from neutron damage. A further discussion of this is provided in the sections pertaining to these individual components. These lithium fluoride disks were produced from natural isotopic precipitated crystalline reagent grade lithium fluoride. The procedure closely followed the published work of Svikis (Svikis, 1963). Several attempts were made before a procedure was found that would produce these disks without cracking to the point which they were unusable. A detailed description of the procedure from the paper is described below.

(Part 1)

**Preparation of Volume-Stable and Dense LiF Aggregate:**

(1) Prepare LiF slips in 2000-gram batches consisting of a weighted ration of LiF and water of 1:1. Slightly warm mixture and gently stir to obtain adequate deaeration.

(2) Using 7 ½ by 4 ¼ by 1 ¼ plaster of Paris Mold, slowly pour slips into molds completely filling each mold. After 10 to 15 minutes, when casting are sufficiently dry invert molds to release castings.

(3) Cut the resulting LiF tiles into small cubes , allow to air dry for 24 hours, and then oven-dry for about five hours at 90$^{o}$C.

(4) Place oven dried cubes on coarse pure alumina grains in a fireclay tray and sinter in an electric laboratory furnace at a heating rate of 170$^{o}$C per hour until

a maximum temperature of 700$^{o}$C is reached. After the maximum temperature has been reached continue to heat at this temperature for 1 to 2 hours.

(Part 2)

**Preparation of Graded LiF Aggregate:**

(1) Take the aggregate from part 2; crush, screen, and grade by mixing four particle size fractions as follows:

| Mesh (Tyler) | Percent |
|---|---|
| - 8 + 10 | 14 |
| - 10 +20 | 36 |
| - 20 + 65 | 15 |
| - 65 | 35 |

(2) Dry-mix graded aggregate for about five minutes, then add 4 percent (based on dry weight of mixture) of a 5% solution of dextrin, and wet mix for another five minutes.

(3) Form into desired shapes by pressing at 8000 psi, allow to dry at room temperature (27$^{o}$C) over night (12hrs), and then oven dry at 90$^{o}$C for about 18 hours.

(4) Heat at 35$^{o}$C per hour to 800$^{o}$C, and maintain the maximum temperature for five hours.

The resulting material should be able to be machined into desired shapes. The bulk density of the material should be about 2.24 g/ml which is 85% theoretical.

It was indicated from the paper that the density could be increased by adding a small amount of raw lithium fluoride powder. However, this increases the chance of cracking.

For the first attempt to produce the lithium fluoride disks, the lithium fluoride was slip-cast into the desired shapes and sintered using (part 1) of the procedure as a guide. This resulted in a significant amount of shrinkage of the disk, which caused it to break into many pieces. In order to correct this, the lithium fluoride was reground in a vibratory mill, pressed into the desired shapes, and re-sintered as described in (part 2) of the procedure. The result of this was much better, however there was still some shrinkage which produced minimal carking along the edges. This shrinkage was thought to be caused by grinding the lithium fluoride too long in the vibratory mill, resulting in a to small grain size. This led to a third attempt, in which the lithium fluoride was ground with a mortar and pestle in order to maintain a larger grain size. The results of this processing were quite satisfactory with almost no shrinkage or cracking. There was a little breakage on the outside edges due insufficient pressing. In future attempts, if the lithium fluoride is uniformly distributed within the press this should be eliminated. The results for all three attempts can be seen in Figure 4-5.

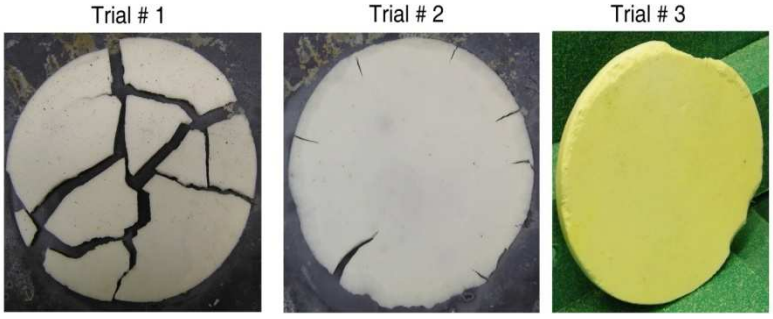


**Figure 4-5: Lithium Fluoride Results, Trial #1 was the first attempt without regrinding and pressing, trial # 2 was the second attempt with regrinding using the vibratory mill and pressing, and trial # 3 was the final attempt regrinding with the mortar and pestle and pressing.**

### *4.4. Collimator*

The collimator for the PGNAA facility was designed with the following objectives: reduce the fast neutron and photon components of the beam in beam port # 4, while still maintaining a high thermal neutron flux, and to collimate the neutron beam to a 2 cm diameter 1 meter out from the downstream end of the collimator.

The shell of the collimator was made of schedule 40 aluminum pipe with aluminum thin-windows on both ends, allowing it to be evacuated or filled with helium to reduce production of gammas and attenuation of the thermal neutrons due to interactions with air. Large-grain poly-crystalline bismuth and single-crystal sapphire are the primary components within the collimator which reduce the fast neutron and gamma components of the beam. The beam is collimated through a series of lead and boral disks with tapered apertures to remove the photons and thermal neutrons present outside the profile of the desired collimated beam. The collimator is illustrated in Figure 4-6 and Figure 4-7.

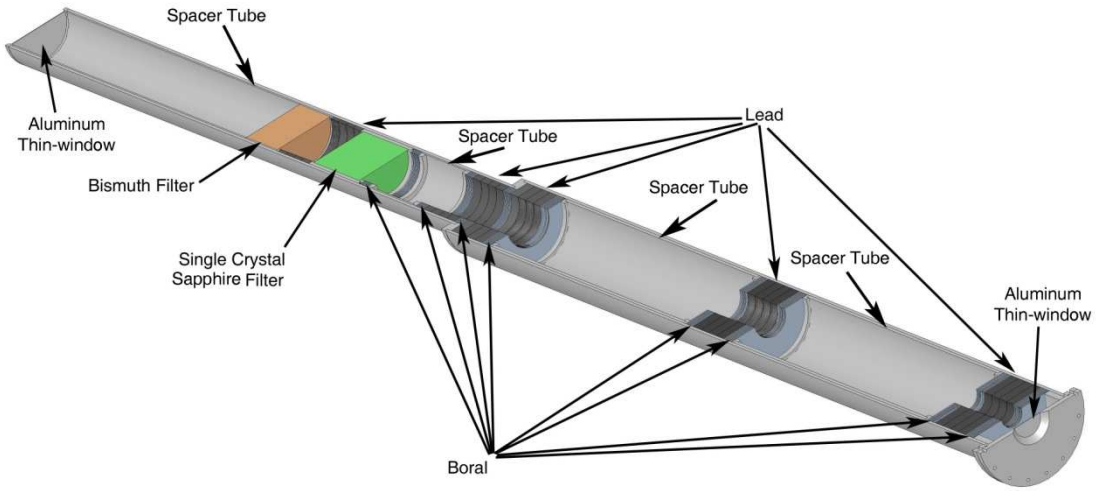


**Figure 4-6: Cross sectional illustration of PGAA collimator with internal components**

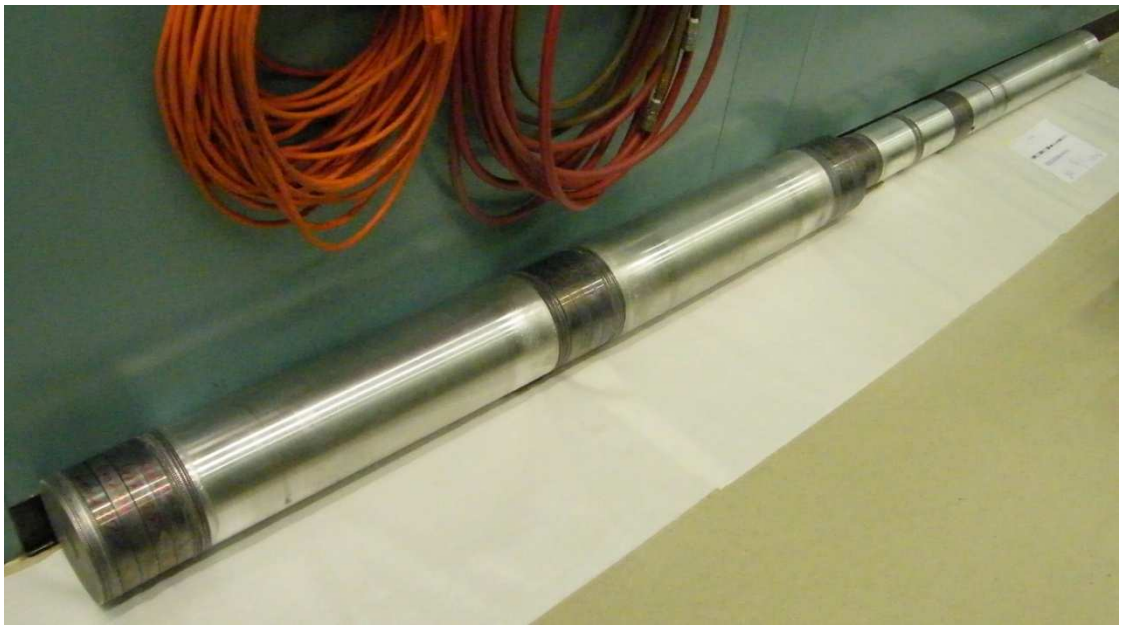

**Figure 4-7: Internal components of PGNAA Collimator**

Because the source which enters the collimator is essentially an isotropic plane source, it is important to consider both the umbra and the penumbra in the design of the beam collimation. The umbra is the focused part of the beam, and the penumbra is the part of the beam which spreads out from the last point of collimation. As far as the sample is concerned the umbra is the important, most intense part of the beam. However, if the penumbra spreads out too much it will interact with the materials around the sample, such as the beam tubes, and increase background levels around the facility. For this reason lead and boral collimator rings were extended into the shutter beam tube as illustrated in Figure 4-8.

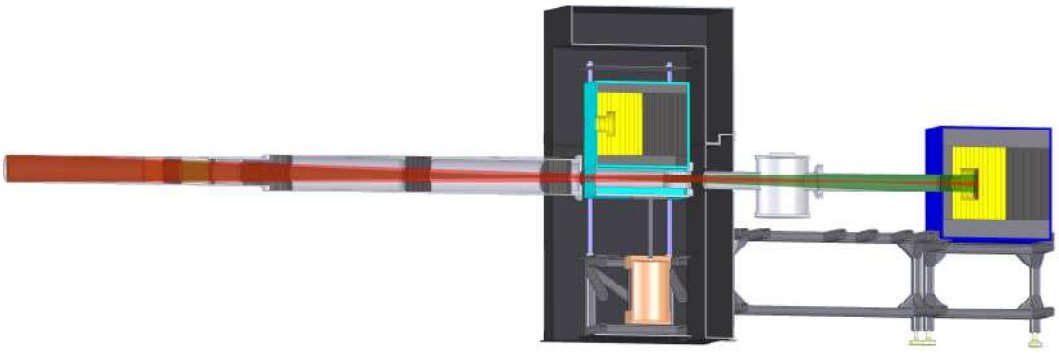

**Figure 4-8: Illustration of major components in facility with predicted beam. The umbra is shown in red and the penumbra is shown in green.**

Large-grain, poly-crystalline bismuth was used because of its large absorption cross section for gammas and its relatively good transmittance of thermal neutrons (M. Adib, 2002). The bismuth in the collimator is 15 cm in diameter and 10.12 cm in length. It was made by placing bismuth in a cylindrical aluminum container and putting it in a muffle furnace above its melting point of 271.4 degrees Celsius. After it was fully melted, the furnace was turned down to about 250 degrees Celsius, and the bismuth was left in the oven for about four days to anneal. This was done to allow crystals growth during solidifications. The bismuth was then removed from the oven and the bottom of the aluminum can was machined off as well as the top of the bismuth to remove any imperfections on both ends. After the bismuth filter was completed, a radiograph image was taken with the OSTR Neutron Radiography Facility. Since the intensity of the radiograph image is directly related to the neutron flux, the transmission of the bismuth was determined by comparing the intensity of the image of the bismuth to the intensity of the image outside the bismuth. These results showed the bismuth filter to have a 28% transmittance for thermal neutrons, as seen in Table 4-1. There were some variations in intensity across the center of the radiograph

of the bismuth, which can be seen in Figure 4-9, which are most likely due to the variations within the crystal orientation and structure within the filter.

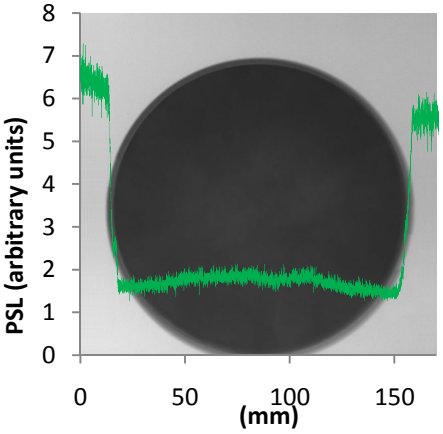


**Figure: 4-9 Bismuth radiograph with profile of intensity**

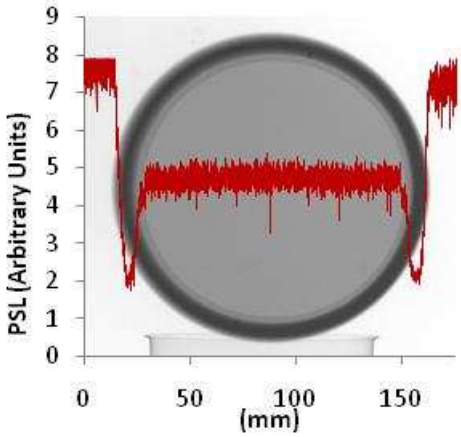


**Figure: 4-10 Sapphire Radiograph with profile of intensity**

A single-crystal sapphire filter is used to reduce the fast-neutron component of the beam. Fast-neutrons are strongly attenuated by the sapphire due to scattering collisions from the wavelength dependent cross section which is low for thermal neutrons but strongly increases for epithermal and fast neutrons, providing that the crystal is oriented with the correct axis parallel to the incoming neutron beam(G. shirane, 2002); (Sears, 1989). This filter is composed of three cylindrical shaped single-crystal sapphire pieces obtained from (Crystal Systems, 2007) with 15 cm diameters and approximate lengths of 64 mm, 46 mm, and 40 mm, which add up to a total filter thickness of 150 mm. The crystal structure is oriented with the $0001 \pm 30'$ axis parallel to the incoming neutron beam. A 150 mm thick single crystal sapphire filter with the 0001 axis parallel to the incoming neutron beam should transmit approximately 70% of the thermal neutrons and 3% of the fast neutrons (I. E. Stamatelatos, 2000). Radiographs were taken, similar to what was done with the bismuth, to determine the transmittance of single-crystals using the OSTR Radiography Facility, for which the

neutron beam is mostly comprised of thermal neutrons (Gadd, 2007). This gave a transmittance for all three crystals combined of 66.05 ± 0.14%, which is tabulated in Table 4-1. The radiograph image in Figure 4-10 also shows a very uniform neutron transmission across the center of the single crystal sapphire, which is expected due to the high-quality of the crystals. The sharp dip in transmittance on the outside of the radiograph is due to the aluminum holder in which the sapphire is held. The sapphire filter and holder are shown in Figure 4-11.

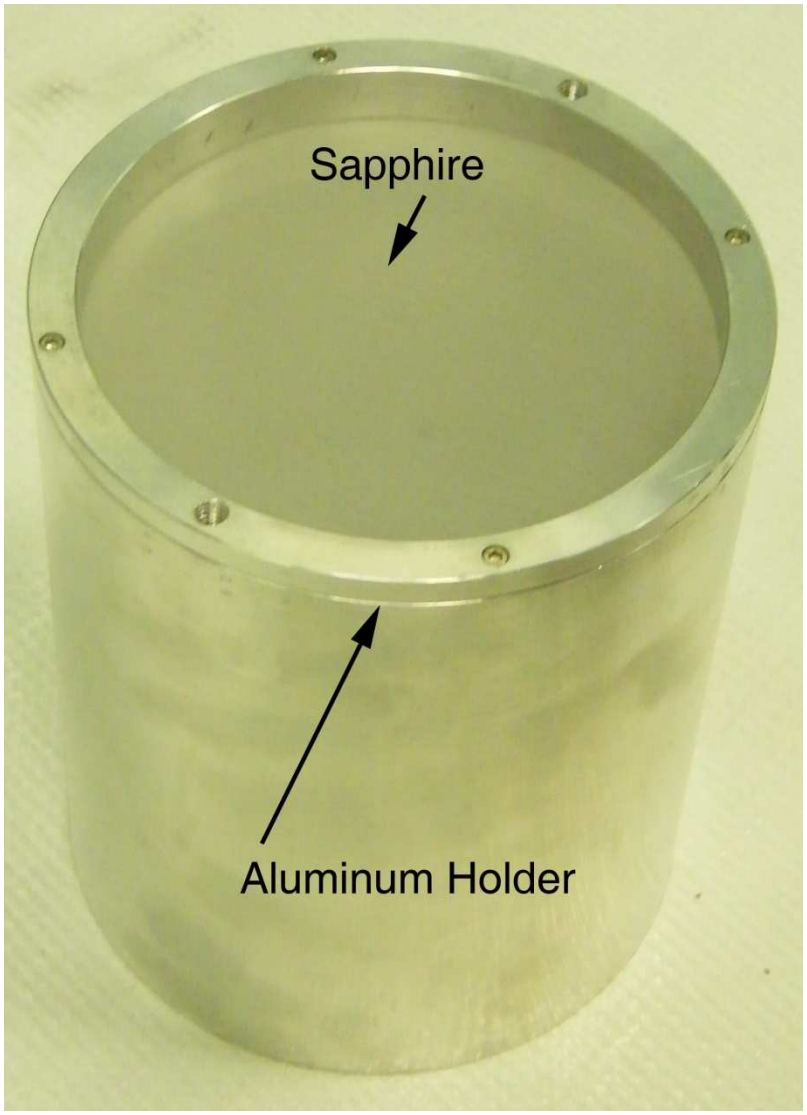


**Figure 4-11: Sapphire crystal in aluminum holder**

**Table 4-1 Sapphire and Bismuth Radiograph results**

| Crystal # | Thickness | Percent Transmittance | Standard Deviation |
|---|---|---|---|
| Sapphire 1 | 6.4 cm | 80.39 | 0.22 |
| Sapphire 2 | 4.6 cm | 90.08 | 0.23 |
| Sapphire 3 | 4.0 cm | 92.39 | 0.19 |
| Sapphire 1, 2, and 3 | 15.0 cm | 66.05 | 0.14 |
| Bismuth | 10.2 cm | 27.98 | 0.06 |
| Bismuth & Sapphire* | | 18.49 | 0.06 |

*Determined from combining results from Sapphire and Bismuth

Using the Monte Carlo N-Particle Transport code developed by Los Alamos National Laboratory (MCNP), an isotropic disk source was used to model the neutron and photon flux entering the collimator from the core of the reactor. The model was run with a series of increasing energies for both neutrons and photons so that the transmission of the collimator could be obtained given an arbitrary energy spectrum of the incident source. Runs were also completed with and without the sapphire and bismuth in order to quantify their effects. The energies for neutrons below the thermal region were neglected because MCNP does not have cross sections for crystalline sapphire and bismuth. However for fast neutrons and photons, the effects of the sapphire and bismuth are independent of the crystal structure. Aside from the materials in the collimator for beam shaping and filtering, it was assumed that the collimator would be filled with helium to reduce attenuation and gamma production with constituents of the air. Thus, all empty space within the collimator was modeled as helium. It was also assumed that the space surrounding the collimator was filled with water. This is not a bad assumption since the first foot of the collimator next to the core is surrounded by water and the rest is surrounded by concrete. Also, neutrons

which scatter back from the outside region are far enough outside the line of collimation that they will not contribute significantly to the flux exiting the collimator.

MCNP is a code which uses random walk processes to determine particle densities within a problem. This is done by simulating the propagation of the particles through the defined problem using random numbers and the probability of possible interactions to determining the fate of each particle. Surfaces, cells, materials, weighting parameters, and source parameters are all defined in an input deck generated by the user, which tells the code the physical parameters of the problem. When a MCNP problem is run the code uses a database, based on the materials and the type of particle generated by the source (i.e., neutron or photon) to determine the probability for the possible interaction the particle may have throughout the problem. Providing the above parameters are defined correctly, the statistical parameters should be very close to the intended problem. Thus, provided enough histories (number of partials generated by the code) are run the answer determined by the code is very close to reality.

When a particle is simulated within the code, the direction, location, and energy are all randomly determined based on the users input parameters for the source. The particle is then propagated through the problem, where the distance traveled between interactions and the type of interactions are determined from the cross sections of the materials within the problem, which are determined by the user input for the material and cell definitions. After an interaction is simulated, the particle may be continued with a new direction and energy, or discontinued depending on the type of interaction.

In the event for which a particle is discontinued, a new particle is started form the source. This process is continued until the specified number of histories has been run.

Within the problem, there are user defined tallies where information about the particles which reach a specified location within the problem are tallied. The MCNP model of the collimator is a deep penetration problem. This results in the necessity for a very large number of particle histories to propagate enough particles to the tallies, in order to get an acceptable statistical error. For these types of problems, it is possible to employ variance reduction techniques to allow some of the particles to continue and or be split into more particles with a reduced weight when interactions are simulated and they propagate through the problem. The reduced weight is calculated such that the contribution the particle makes if it reaches a tally is reduced to account for the non-analog tracking. Providing variance reduction is used correctly, it can increase the number of particles reaching the tallies and provide a better relative error for the final answer.

In one type of variance reduction, the problem can be divided into a large number of cells and the particles which cross the boundaries can be split into several particles to account for the particles which have been lost. In the case of the collimator, it was necessary to divide the model into 1 cm thick cells and use substantial geometry splitting in which importances are assigned to each cell in order to get a significant number of particles reaching the end tallies. The MCNP model for the collimator is illustrated in Figure 4-12.

When using importances in MCNP, each cell is assigned an importance, $I$, on the INP input card. When a particle of weight $W$ leaves a cell of importance, $I$, and enters

a cell of higher importance *I',* and if *I* and *I'* are integers, the particle is split into *n* identical particles with weight *W/n* where *n* is equal to *I'/I*. If *I* and *I'* are not integers, then the splitting is done probabilistically so that the expected number of splits is equal to *I'/I.* However, if a particle of weight *W* leaves a cell of importance *I* and enters a cell of lower importance *I'*, then Russian roulette is played and the particle is discontinued with a probability of *1-(I'/I)* or continued in the same direction with a probability of *I'/I* with a weight (*W)(I'/I).* (X-5 Monte Carlo Team, 2005)

When using importances, the importance should increase from cell to cell in the direction of the tally region and should decrease in directions away from the tally region where they do not significantly contribute to the tally. As a general rule, the importances should be adjusted such that the number of particles moving from the source to the tally region remain relatively constant and close to the total number of histories run. By putting PRINT 126 in the source card of the MCNP deck, MCNP will produce a table with the information about the tracks entering, population, collision, flux, and weighting for each cell. Thus by running a trial run with all importances equal to 1, it easy to see from the tracks entering each cell how to adjust the importances. For the case of the collimator, it was necessary to iterate on several trial runs to find the optimum importance level for each cell.

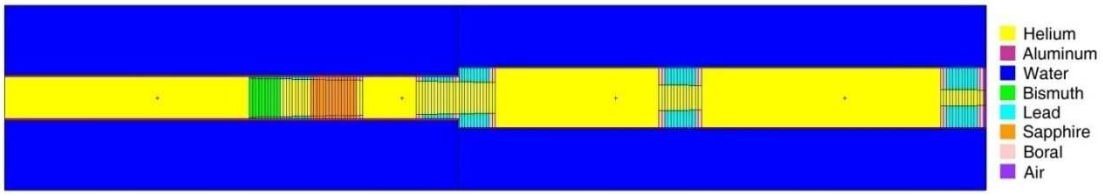


**Figure 4-12 MCNP model of collimator**

MCNP models of the collimator were run to obtain results for the fraction of transmitted neutrons as a function of energy in the collimated beam with and without the sapphire filter and/or bismuth filters (Figure 4-13). The results without the sapphire or bismuth are entirely geometric attenuation since there is very little interaction within the helium. The rounded hump in the region of 1 to 2 MeV in the results with only bismuth is due to the dip in the cross section in this energy region as illustrated in Figure 4-14. Similarly, the dip in the transmission for the results with the sapphire around 3 to 4 MeV is due to an increase in the cross section of oxygen in this region as illustrated in Figure 4-15.

Even though the bismuth filter was primarily chosen to reduce the gamma component of the beam, it is also fairly effective in reducing the fast-neutron component as well. The MCNP results showed there was a reduction in the fast neutron flux by about one order of magnitude with the bismuth and 2 orders of magnitude with the sapphire as shown in Figure 4-13. As mentioned before, the MCNP results are only valid for neutrons outside the thermal region and were used primarily for shielding considerations. The overall transmission in the neutron flux around 2 MeV in the MCNP results for the collimator is around $10^{-6}$. This was considered to be a conservative estimate given that the average fission neutrons is born at around 2 MeV, with a predominate energy of approximately 0.7 MeV (Duderstadt & Hamilton, 1976). Thus, if the source strength were $10^{12}$ neutrons/cm$^2$/s, this would leave a flux of approximately $10^6$ neutrons/cm$^2$/s of 2 MeV neutrons which would need to be shielded with the shutter beam stop or the final beam stop when the facility was in use.

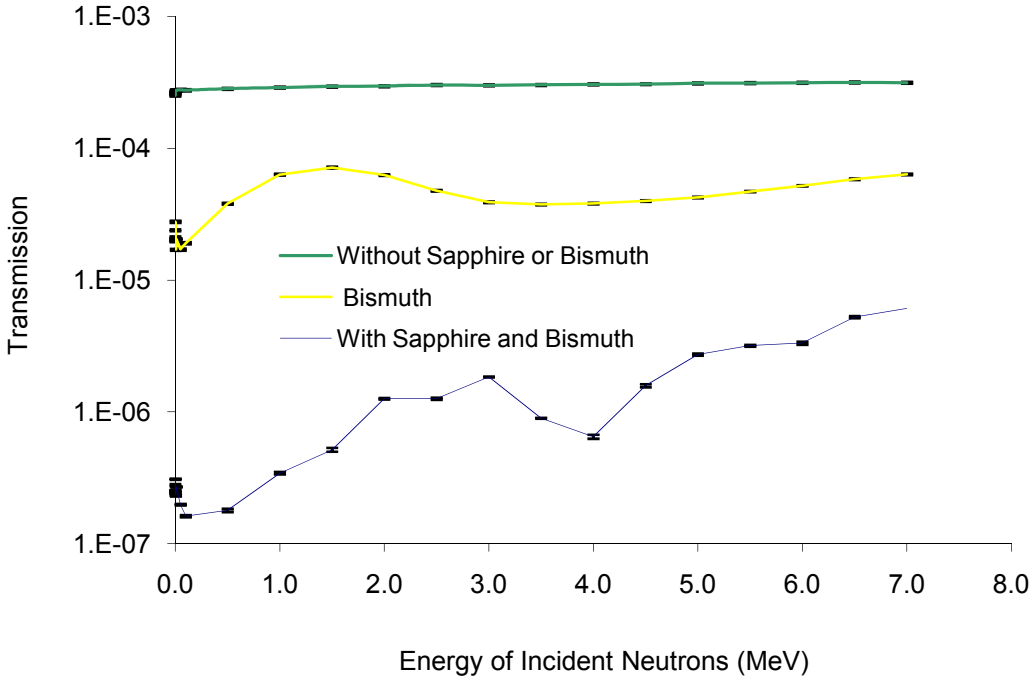


**Figure 4-13 Neutron transmission as a function of Energy inside collimated beam (MCNP Results)**

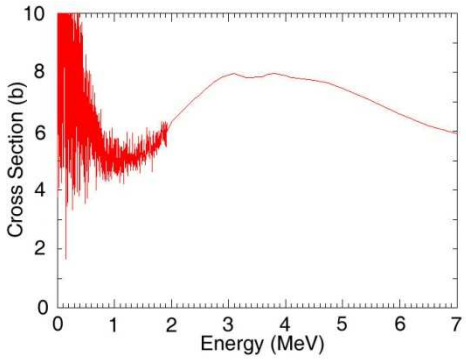


**Figure 4-14: Bismuth total neutron cross section (ENDFPLOT: online graph plot for neutron cross section, 2008)**

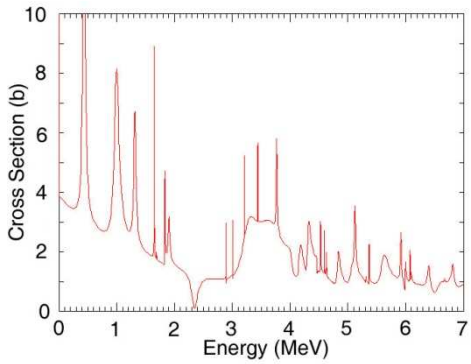


**Figure 4-15: Oxygen Total neutron cross section (ENDFPLOT: online graph plot for neutron cross section, 2008)**

The MCNP results for the photon transmission of the collimator as a function of energy for both the sapphire and the bismuth had a comparable reduction in the photon

flux for both, with the sapphire being slightly greater in the higher energy regions as shown in Figure 4-16. Thus, in principal the thermal neutron flux could be maximized by using only sapphire and achieve the same reduction on the photon transmission. This, however, was not done because of the add expense of extra sapphire, and the transmission of fast neutrons with the bismuth and sapphire was considered to be satisfactory.

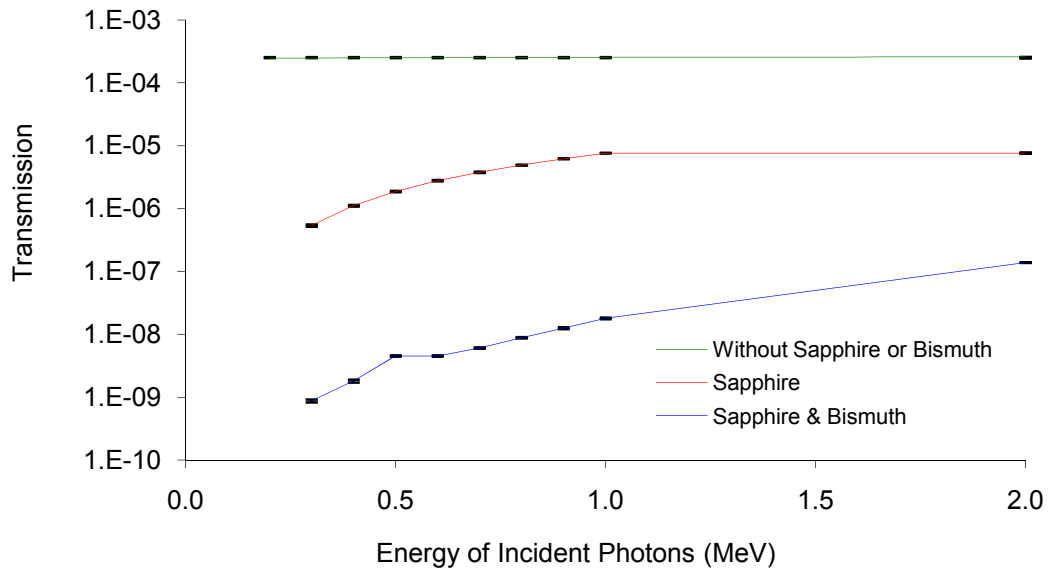


**4-16 Photon transmission as a Function of Energy (MCNP Results)**

### *4.5. Shutter and Beam stop*

The purpose of the PGAA shutter is to stop the neutron beam exiting the collimator when the facility is not in use. The beam stop is used to stop the beam when the shutter is open. Thus, it is necessary to have a stationary beam stop and a shutter which can be efficiently and quickly moved into and out of position. In order to satisfy these criteria, the beam stop, consisting of an aluminum box filled with lead and 5% borated polyethylene, was mounted on an air cylinder with linear rod bearings for guides. To open the beam, air is applied to the cylinder and the beam stop is lifted out of position. When the cylinder is vented, the beam stop falls to its closed position due to gravity alone. The advantage of this design is that it can be closed in the event of a loss of power and there are no mechanical components which are likely to fail which could leave the shutter in an open position. A similar beam stop, which is mounted on a stationary steel stand is used as the final beam stop when the shutter is open. The beam stop and the shutter are both shown in Figure 4-17 during their installation.

**Figure 4-17: Shutter and Beam-stop during installation**

The shutter beam stop and the final beam stop both needed to be designed to reduce the maximum neutron and gamma doses exiting the collimator to an acceptable level

so there would be no exposed high-radiation areas around the facility. This means that the radiation level 30 cm from any exposed surface of the facility must not exceed 100 mrem/ hr for both the gamma and neutrons doses combined (10 CFR 20.1003) and in practice must be much lower to not affect the PGNAA measurement or other experiments in the area.

Since the beam exiting the collimator would be fairly well collimated, it was assumed that both beam stops would need an equivalent amount of shielding. With the exception of less shielding for the back scatter from the shutter because this was not as great a concern since this would be directed back into the reactor bioshield. Also it was assumed that there would be scattering around the shutter during transition and thus there would need to be a bioshield surrounding the shutter to minimize this scattered radiation. Considering all these things and keeping in mind that the shutter needs to move up and down, the shutter was built with the same amount of shielding for penetration of radiation as the final beam stop, however in order to reduce the size and weight it was built with less shielding on the outside edges and a scatter chamber with less depth.

Both beam stops were designed with 6 inches of 5% borated polyethylene and 10 inches of lead from the front to the back as shown in Figure 4-18 and Figure 4-19.

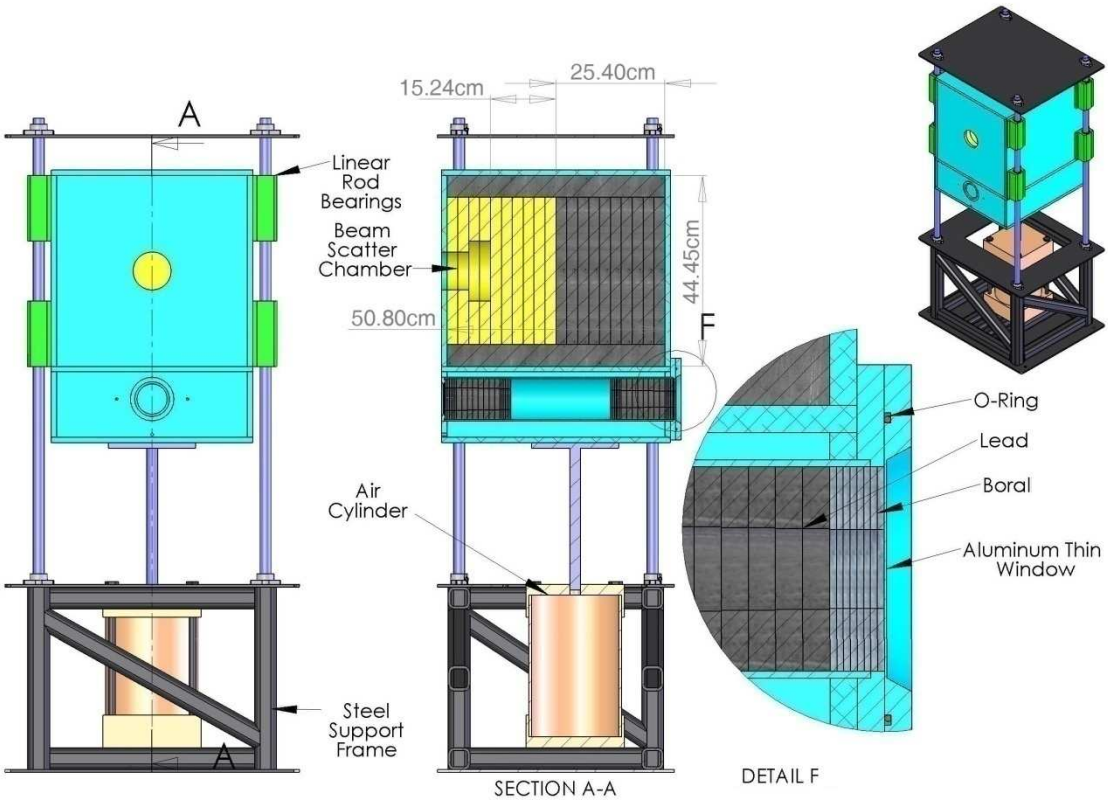


**Figure 4-18: Shutter Assembly**

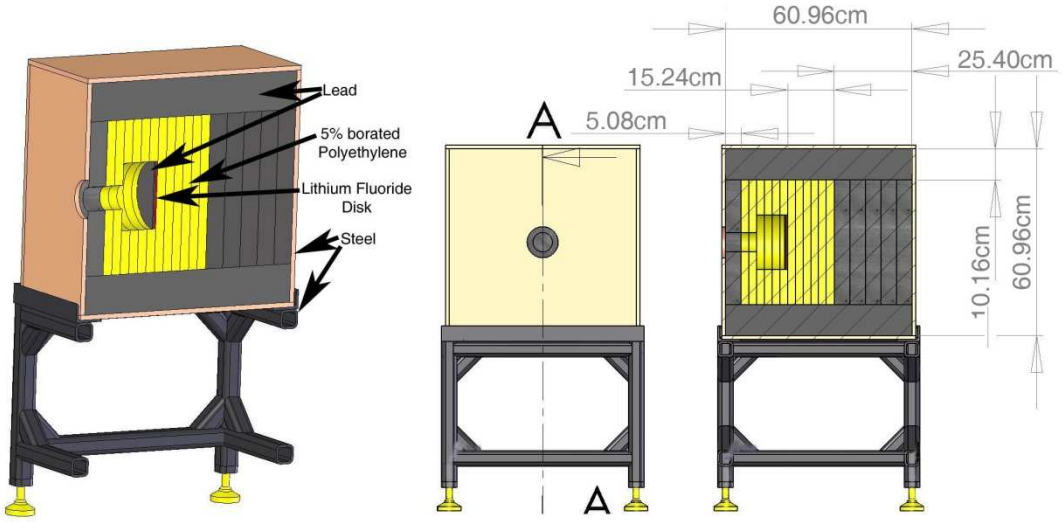


**Figure 4-19: Final Beam stop**

However, the top, bottom, and sides of the shutter beam stop have 2 inches less lead, and 1 ¼ inches less 5% borated polyethylene. Also, the final beam stop scatter chamber is deeper and has two inches of lead on the front, as well as a lithium fluoride disk and a lead disk at the back of the scatter chamber. The two inches of lead on the front of the final beam stop, and the lithium fluoride and lead disks are there to reduce the gamma dose levels which scatter back from the beam stop. This was especially important since gammas which scatter back from the final beam stop will increase the background levels around the PGNAA sample and detector.

The lithium fluoride disk used in the beam stop was made of naturally isotopic lithium which has abundances of 7.40% $^{6}$Li and 92.60% $^{7}$Li. The (n,$\alpha$) reaction is the primary reaction for thermal neutrons with $^{6}$Li, in which an alpha particle and tritium nucleus are produced. The advantage of $^{6}$Li is that the cross-section for (n,$\gamma$) reaction is very low in comparison to the (n,$\alpha$) reaction as shown in Figure 4-20 and Figure 4-21, and thus there is very little increase in the gamma background as opposed to boron which has large (n,$\gamma$) cross section. The disadvantage of $^{7}$Li is that it has a very low capture cross-section for the (n,$\gamma$) reaction with a magnitude very close to the cross section of the (n,$\gamma$) reaction for $^{6}$Li as shown in Figure 4-22 and Figure 4-23. Thus, $^{7}$Li is not the best material for the removal of thermal neutrons. Figure 4-23 is a plot of the total cross-section for $^{7}$Li which is primarily due to elastic scattering. Thus, because of the relatively low (n,$\gamma$) reaction for $^{7}$Li it was decided that natural abundance lithium fluoride would be acceptable initially, future plans include replacement with $^{6}$Li.

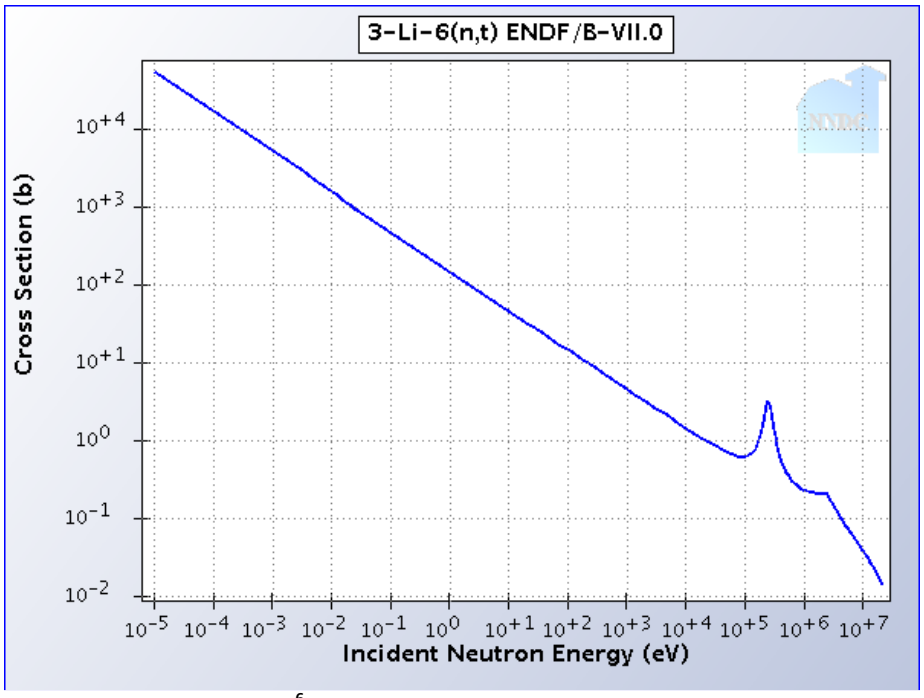


**Figure 4-20 Cross-section for $^{6}$Li (n,$\alpha$) Reaction (Brookhaven National Laboratory, 2008)**

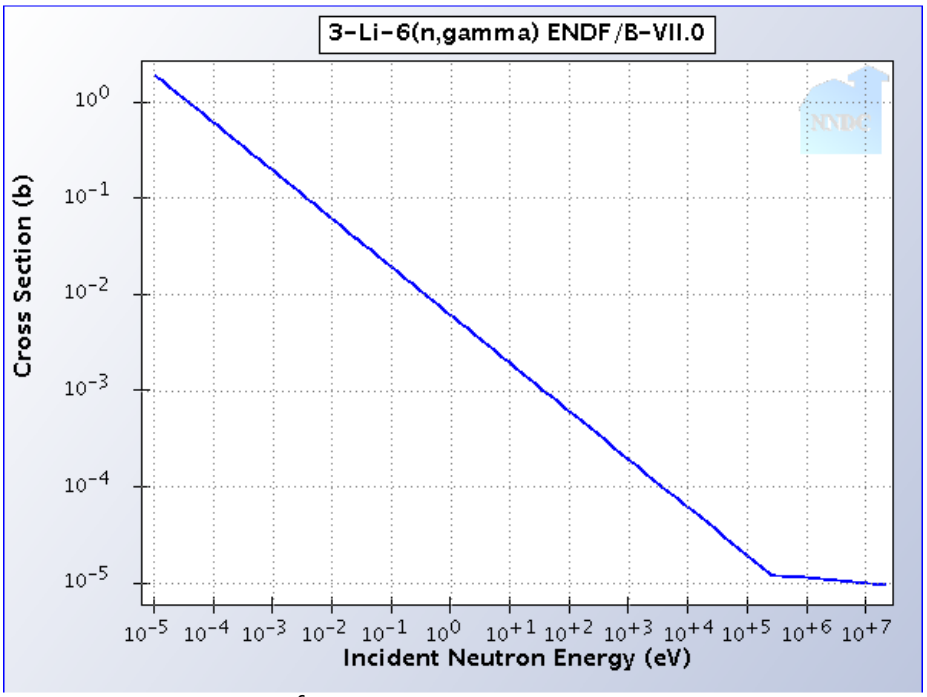


**Figure 4-21 Cross-section for $^{6}$Li (n,$\gamma$) Reaction (Brookhaven National Laboratory, 2008)**

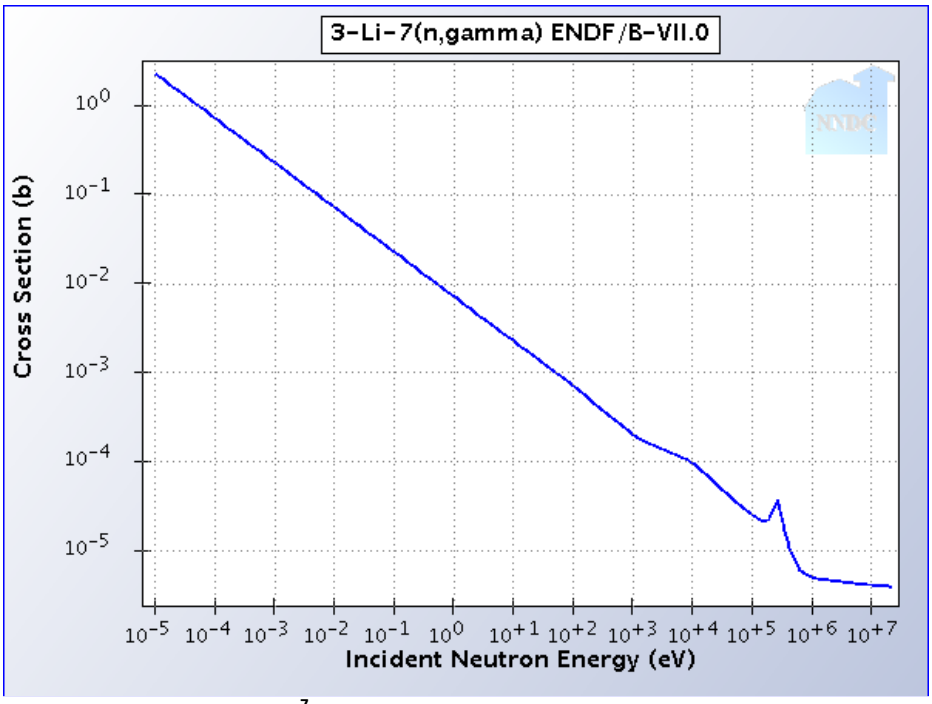


**Figure 4-22 Cross-section for $^{7}$Li (n,$\gamma$) Reaction (Brookhaven National Laboratory, 2008)**

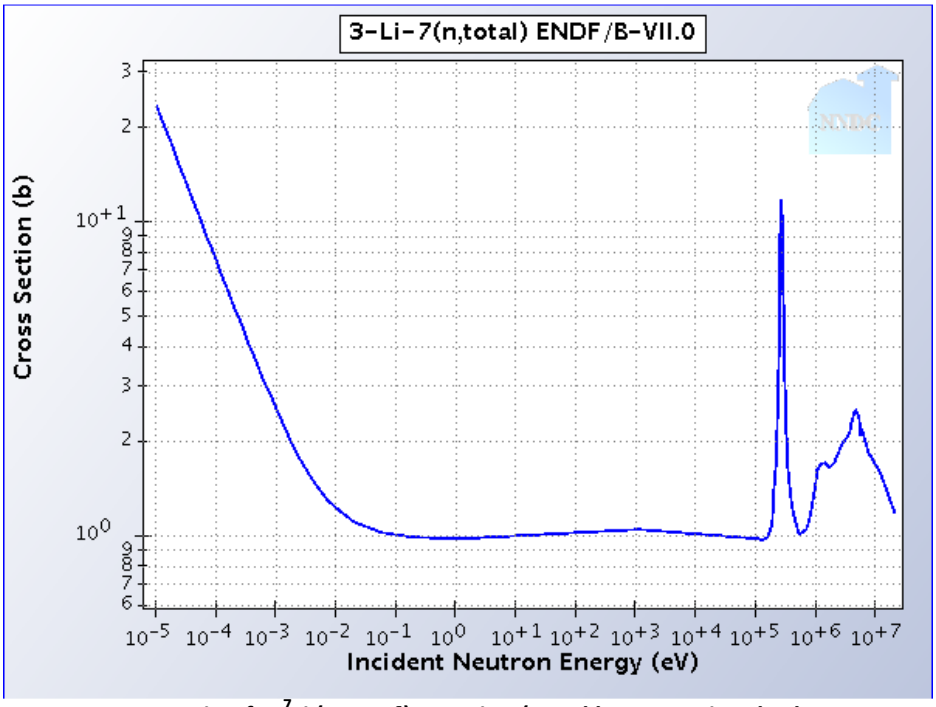


**Figure 4-23 Cross-section for $^{7}$Li (n, total) Reaction (Brookhaven National Laboratory, 2008)**

The quantities of lead and borated polyethylene, the percent boron content in the polyethylene, the geometric configuration, and the effects of the lead disk were determined from the material properties and MCNP simulations.

There were two standard options of 5% and 30% boron content by weight. It was found that the neutron transmission for the beam stop with 5% borated polyethylene was approximately 50% less than that of the 30% borated polyethylene for 2 MeV neutrons (see Table 4-2). There was no significant change observed to the photon transmission (see Table 4-3). These results are not surprising since the neutrons must be thermalized in order to increase the probability of neutron capture within the boron. If too much boron is added to the polyethylene, there will be less polyethylene and therefore less thermalization of the neutrons. Since fast neutrons were of more concern, it was decided that the 5% polyethylene was better suited for this application.

**Table 4-2: Beam stop MCNP results with 2 MeV neutrons**

| | 5 % boron | Variance | 30% boron | Variance |
|---|---|---|---|---|
| **Fraction Exiting** | 4.51E-04 | 0.0104 | 7.81E-04 | 0.0082 |
| **Fraction Scattering Back** | 7.43E-03 | 0.0447 | 7.68E-03 | 0.0438 |

**Table 4-3: Beam stop MCNP results with 2 MeV Photons**

| | 5 % boron | Variance | 30% boron | Variance |
|---|---|---|---|---|
| **Fraction Exiting** | 1.20E-07 | 0.0042 | 1.20E-07 | 0.0042 |
| **Fraction Scattering Back** | 2.19E-05 | 0.0194 | 2.19E-05 | 0.0194 |

The lead disk, which was placed at the front of the scatter chamber of the beam stop as shown in Figure 4-19, reduces the photons which scatter back from the beam stop.

MCNP predicted that the lead disk reduced the photons which scattered back by about 80% (see Table 4-4). This suggests that some of the photons which scatter back from the polyethylene are being attenuated or scattered by the lead disk.

**Table 4-4: Beam stop MCNP results for 1 MeV photons with and without lead disk**

| | Without lead | MCNP Variance | With lead | Variance |
|---|---|---|---|---|
| **Fraction Exiting** | 1.45E-04 | 0.0159 | 2.73E-05 | 0.035 |

For the neutrons it was assumed that the maximum flux exiting the reactor was $10^{12}$ neutrons/cm$^2$/s and that the energy of the neutrons were 2 MeV. However, for the photons, the flux in beam port # 4 was not very well known, so the materials used in the beam plug were used as a rough guide of how much gamma shielding would be needed in the beam stop while taking into account the reduction from the materials which would be in the collimator.

As mentioned in section 4.4, the neutron transmission for the collimator as determined by MCNP was approximately $10^{-6}$ for 2 MeV neutrons. And since the transmission using MCNP of the beam stop was determined to be $4.5\times10^{-4}$ for 2 MeV neutrons, this would give a total transmission of the collimator and beam stop of approximately $4.5\times10^{-10}$. Assuming that the flux entering the beam port is $10^{12}$ neutrons/cm$^2$/s of 2MeV neutrons, the total flux exiting the beam stop would be approximately 450 neutrons/cm$^2$/s. In order to be conservative it was assumed that the exiting flux was entirely composed of 2MeV neutrons. Also, the dose conversion

factors for 2MeV neutrons is 1.43E-04 (rem/hr)/(n/cm$^2$-s) based on ICRP-21 dose conversion factors (X-5 Monte Carlo Team, 2005). Using this conversion factor and the estimated MCNP result of 450 neutrons/cm$^2$/s, the estimated dose rate exiting the beam stop was calculated to be 64 mrem/hr. This value does not include geometric attenuation between the beam stop and the end of the collimator, which reduces the flux to about 60 percent of that which is exiting the collimator. This would suggest a dose exiting the beam stop of about 40 mrem/hr.

As mentioned above, the photon flux was not very well known, so the existing beam plug of beam port #4 was used as a guide to judge whether the photon shielding would be sufficient. The existing beam plug was made up of a combination of lead, wood, and concrete which was the equivalent of about 10 tenth-value layers for 2MeV photons as shown in Table 4-5. Also at 1 MW the photon dose exiting the beam plug was very close to background levels of about 1-2 mrem/hr. Using the same analysis for the materials within the collimator and the beam stop, the shielding was determined to be approximately 9 tenth-value layers thick for 2 MeV photons. Assuming that the 1-2 mrem/hr measured dose exiting the beam plug at 1MW was due to radiation exiting the beam port, this would suggests a dose of 10-20 mrem/hr gamma dose exiting the beam stop, due to one tenth value layer less than that which was in the beam plug.

**Table 4-5: Material thicknesses of beam plug in Beam port #4 and tenth value layers for 2 MeV photons**

| | # of tenth value thickness |
|---|---|
| **5 in lead** | 2.88 |
| **4 ft concrete** | 5.46 |
| **4 ft wood** | 1.78 |
| **Total** | 10.11 |

**Table 4-6: Material thicknesses of collimator and beam stop and tenth value layers for 2 MeV photons**

| | # of tenth value thickness |
|---|---|
| **10 in lead** | 5.76 |
| **6 in polyethylene** | 0.312 |
| **4 in bismuth** | 1.97 |
| **6 in sapphire** | 1.15 |
| **Total** | 9.19 |

After installation of the shutter and beam stop, it was found that the neutron radiation levels were higher than expected, resulting in a high radiation area around the beam stop and shutter (section 5). In order to correct this concrete blocks were added around three sides and the top of the final beam stop and polyethylene and borated polyethylene were added to the forth side facing the sample chamber. The polyethylene was added after the detector was installed to reduce the scattered neutron dose to the detector. This shielding added 15 inches of concrete on the back and sides of the beam stop, 13 ½ inches of concrete on the top, and 3 inches of regular polyethylene, along with 2 inches of borated polyethylene on the front as shown in Figure 4-24.

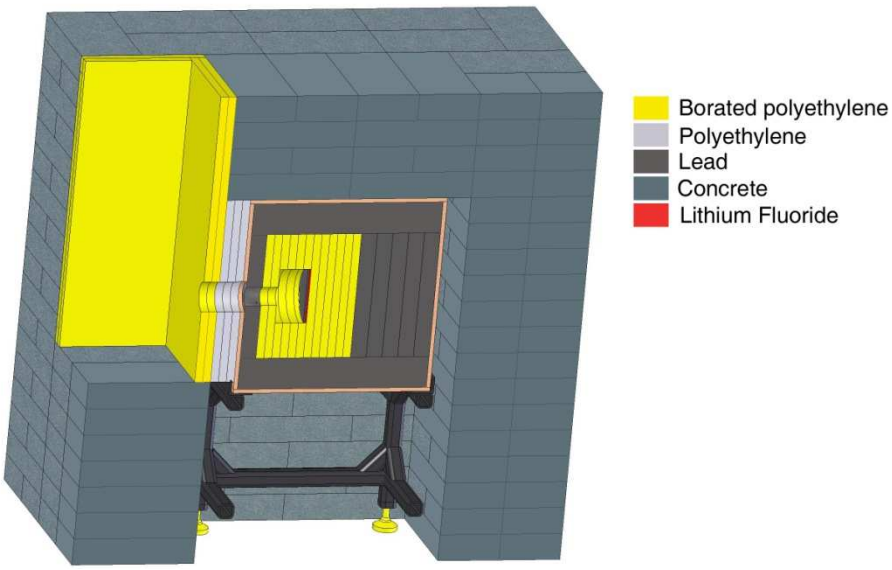


**Figure 4-24 : Beam stop with added shielding**

This added shielding resulted in background levels for both neutron and gamma dose rates exiting the back side of the concrete increasing to 20 mrem/hr for neutron and 5 mR/hr for gamma on the sides closest to the sample chamber. These radiation measurements, as well as others taken during and after the installation of the facility are discussed in section 5.

In the case of the shutter, elevated neutron doses were addressed with a removable bioshield. The design and MCNP analysis of this bioshield is discussed in the following section.

### *4.6. Shutter Bioshield*

It was found that a bioshield was necessary to reduce the neutron radiation levels to a point where they were acceptable for a personal standpoint, and to reduce background levels around the detector. These elevated radiation levels where primarily from scatter off the last set of lead collimator rings at the end of the collimator, as well as the final collimation in the shutter beam tube, and a higher fast neutron flux than expected (section 4.5). This bioshield at several stages during its installation is shown in Figure 4-25

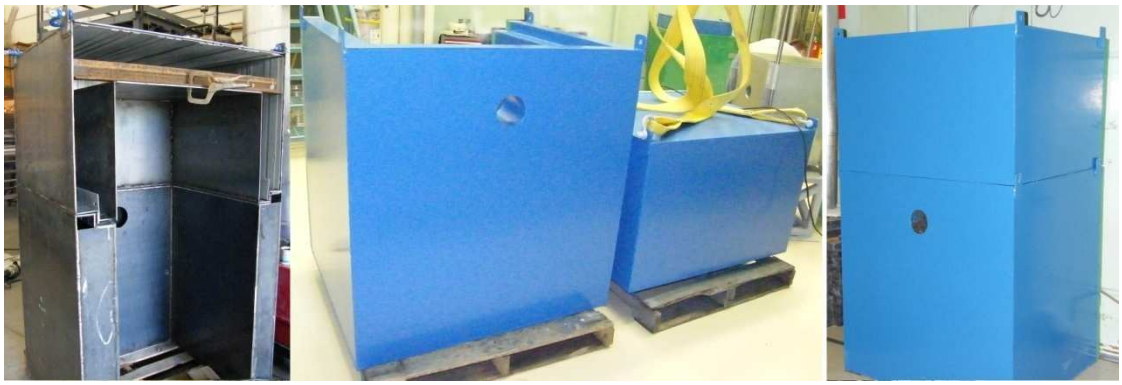

**Figure 4-25: Shutter Bioshield during and after installation**

The design of the bioshield was analyzed with MCNP simulations consisted of a two part steel shell which was lined on the inside of all the outside surfaces with 1/8 in of boral sheeting and then filled with paraffin. This resulted in ½ inch of steel, 6 inches of paraffin and 1/8 inch of boral surrounding all three exposed sides of the bioshield. The top was the same with the exception that there was an additional 2 inches of paraffin adding up to a total of 8 inches as shown in Figure 4-26. The steel shell provides some attenuation of gamma rays. However, its primary purpose was to provide structural support to the shield and to contain the paraffin while it solidified after being melted and poured into the shield. Paraffin was used to thermalize fast

neutrons and the boral was used to capture the thermalized neutrons. Polyethylene was also considered, but it was found that paraffin was considerably less expensive and since the carbon and hydrogen content and density of paraffin and polyethylene are very close, their ability to thermalize neutrons is essentially the same.

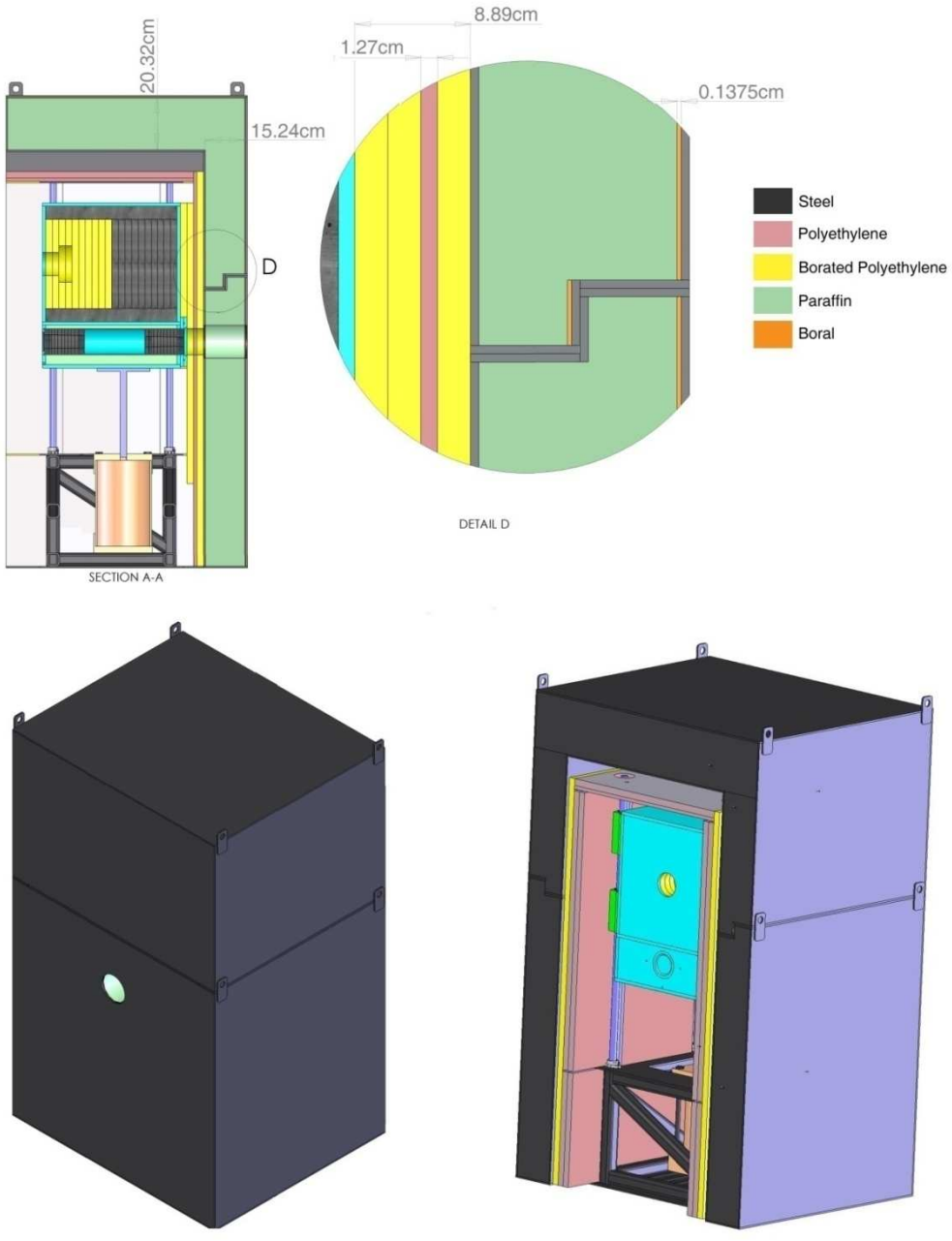


**Figure 4-26: Shutter Bioshield**

The MCNP models were used to analyze the effects of the bioshield design. This was done by modeling the shutter beam stop both with and without the bioshield. The source term for the MCNP model consisted of a 2 MeV neutron beam with a 2.5 in diameter entering the beam stop. The neutron energy of 2 MeV was chosen because this was considered to be the most restrictive energy, and thus it was assumed that the majority of the neutrons entering the shutter beam stop would not be greater than this energy.

Because the flux of the beam entering the shutter beam stop was not known, the MCNP model without the bioshield was used to equate the measured doses, with the results for the MCNP model with the bioshield. The measured dose exiting the shutter from Table 5-2 was divided by the dose output from MCNP for the same shutter configuration. After this all the doses outputted from MCNP were multiplied by this conversion factor to get the approximate doses for the beam entering the shutter beam stop.

A diagram of the geometry used in the MCNP model and the corrected doses outputted from MCNP are displayed in Figure 4-27 and Figure 4-28. The model used in Figure 4-28 has an additional 3 inches of borated polyethylene added to the shutter beam stop. This was done to minimize the dose to the experimenter's hands while changing samples in the sample chamber, which is placed immediately after the bioshield.

Based on the MCNP result presented in Figure 4-27, and Figure 4-28 it was decided to add 2 inches of borated polyethylene to the shutter beam stop. Based on these results, it would be expected that the neutron dose rate exiting the beam path of

the bioshield would be about 25 mrem/hr. The measured neutron dose rate after installation of the bioshield with the added 2 inches of polyethylene was 30 mrem/hr. This value was reduced even further by additional shielding which was added inside the shutter bioshield in an attempt to further reduce the neutron dose around the detector. This shielding consisted of an additional 3 to 4 inches of polyethylene surrounding the shutter, which reduced the dose rate in the sample chamber with the shutter closed to 2mR/hr gamma and 12 mrem/hr neutron. Overall, the effect of the added shielding reduced the radiation levels around the bioshield by a factor of 2 to 3.

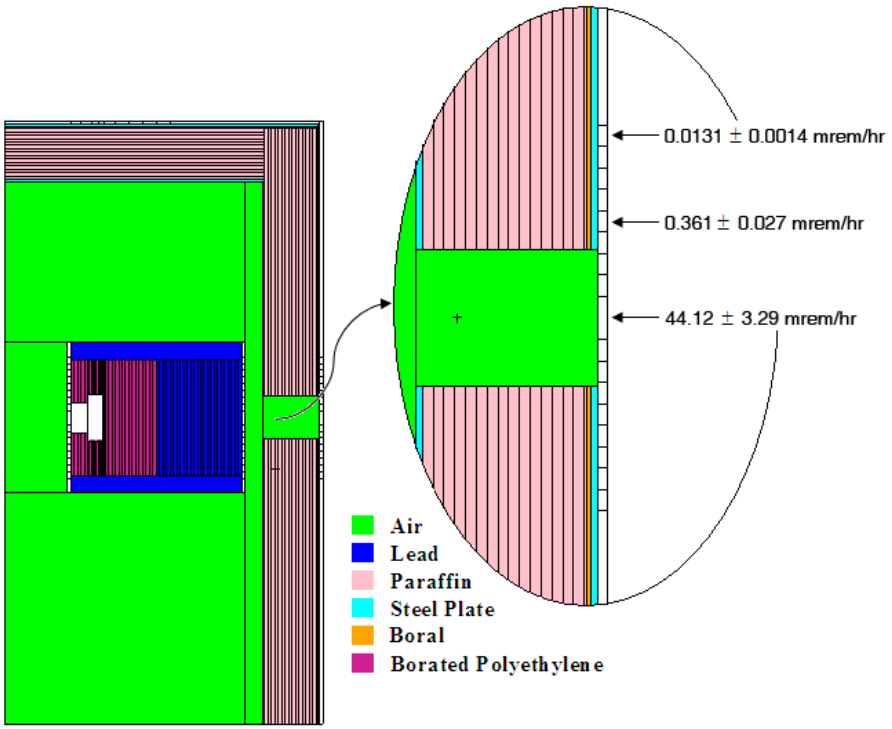


**Figure 4-27: Bioshield neutron MCNP dose results without added borated polyethylene on shutter beam stop, 2.0MeV beam with 2.5in diameter entering shutter beam stop (Doses based on 200mrem/hr exiting center of shutter)**

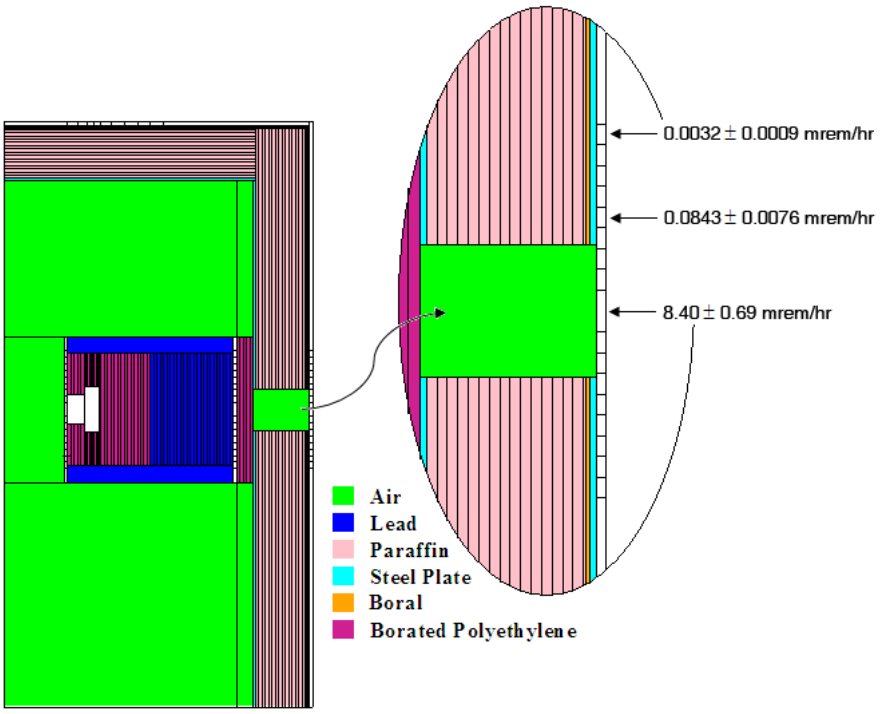


**Figure 4-28: Bioshield neutron MCNP dose results with added borated polyethylene on shutter beam stop, 2.0MeV beam with 2.5in diameter entering shutter beam stop (Doses based on 200mrem/hr exiting center of shutter)**

## 4.7. Sample Chamber and sample holder

The sample chamber is where the samples are housed while they are irradiated. Since the sample chamber is exposed to radiation scattered out of the beam primarily by the sample itself, and much of the sample chamber is in direct line-of-sight to the detector, it should be made of a material which does not generate a significant gamma-ray background around the facility and does not become activated with prolonged exposure to radiation. The gamma-rays produced by the sample chamber should be easily distinguishable from those of the sample itself. Yet another important constraint is that the sample chamber must be able to hold up to atmospheric pressure when it is evacuated. To accommodate the design criteria, the sample chamber was built out of aluminum. Not only is aluminum durable, easy to machine and manufacture into almost any shape, it has a relatively low absorption cross section for thermal-neutrons and there are no long-lived radioactive isotopes generated when it is exposed to high neutron or gamma radiation. Also, the gamma-rays which are produced by neutron capture of aluminum are for the largely of energies which are easily distinguished from those of other elements. It should be noted however, that if aluminum is among, or the analyte within the sample, then very careful consideration will need to be taken in order to correctly subtract the signal produced by the aluminum in the sample chamber.

The sample chamber for this facility was made out of an aluminum cylinder of approximately 30 cm in diameter and 33 cm in length. Both ends which serve as the top and bottom of the sample chamber are equipped with round aluminum plates machined such that they are partially recessed into to the cylinder, and a vacuum tight seal is accomplished by o-rings which are seated in both ends of the cylinder, as shown in Figure 4-29.


**Figure 4-29: PGNAA Sample Chamber**

The beam tubes extending from the sample chamber to the bioshield, beam stop, and detector are all connected to the sample chamber by o-ring sealed flanges, and the ends of these tubes are all sealed by aluminum-thin windows welded directly to the tube.

The sample holder is designed to hold the sample in the beam while minimizing interaction of the beam with the sample holder itself. This is accomplished by a

rectangular shaped aluminum U machined out of piece of approximately 0.6cm thick aluminum plate whose posts are positioned on either side of the beam and situated such that the sample is held at a 45$^{o}$ angle to the beam. This positions the posts out of line of sight of the detector and minimizes self shielding for thin disk shaped samples. Shown in Figure 4-30, the sample holder is held in place by a vertical aluminum post with two aluminum pegs on one side and a piece of spring steel on the other side. This system allows for easy removal of the holder which is necessary for precise positioning of the samples on the holder. The sample is typically sealed in a Teflon® film which is stretched between or suspended from Teflon® line stretched between the two posts.


**Figure 4-30: Sample holder setup with sample**

Teflon® is used because the capture-cross sections for fluorine and carbon are quite low, resulting in only a few additional discrete gamma energies in a measured spectrum.

### *4.8. Detector and, Detector shielding*

Depending on the decay schemes of the compound nuclei produced during PGNAA from the isotopes within the sample of interest and the number of different isotopes within the sample, there often are a large number of discrete gamma energies which need to be distinguished. These gamma energies range from around 50 keV to 10 MeV, and depending on the isotopes, many of these energies may be separated by only few keV. High-purity germanium detectors (HPGe) are well suited for PGAA because of their very good energy resolution. The detector chosen for the facility was a HPGe with a resolution of 1.73 keV and a relative efficiency of 36.50 % at 1.33 MeV. A complete list of the specifications for this detector is presented in Table 4-7.

Because of the elevated radiation levels around the facility it is necessary that the detector be well-shielded from both gammas and neutrons in order to increase the signal-to-noise ratio and to protect the detector from neutrons which damage the crystal structure, leading to a degraded performance. Shown in Figure 4-31, the detector is surrounded by a large amount of lead and borated polyethylene. The lead is used to reduce the gamma background, and borated polyethylene is used to reduce the neutron background.

The amount of each material was determined by experimenting with different shielding configurations. Initially the detector was surrounded by 3 inches of paraffin, 2 inches of borated polyethylene, and 4 inches of lead. The survey meters used to measure the neutron and gamma dose rates would not fit in the detector position with the lead in place so measurements were taken without the lead. These measured doses without the lead were 3 mR/hr for gamma and 2 mrem/hr for neutron. In order to evaluate this configuration, background spectra were taken with shutter open, both

with and without the sample chamber evacuated. The dead time for these spectra was about 10-12% with a high background count rate, showing pronounced hydrogen and aluminum peaks from interactions within the aluminum and polyethylene as shown in Figure 4-32. Based upon these spectra and radiation measurements which showed that the majority of the neutron flux was coming from the beam line, the detector shielding was modified to have the configuration shown in Figure 4-31. This configuration resulted in over 8 inches of lead on all sides except the side towards the bioshield, which had 5 ½ inches and 1 to 2 inches of borated polyethylene on all sides, except the front which had 5 inches of borated polyethylene to account for the higher neutron flux coming from the beam line. The lead was also machined to closely fit around the detector to minimize streaming in from the detector side, as well as two lead collimators placed in the flight path from the sample to the detector. There was also a lithium fluoride disk placed in front of the detector to reduce the effect of thermal neutrons scattered by the sample. These lead collimators were situated with one at either end of the flight tube to the detector and are tapered such that they minimize the solid angle of the detector to about a 3 cm diameter at the sample location.

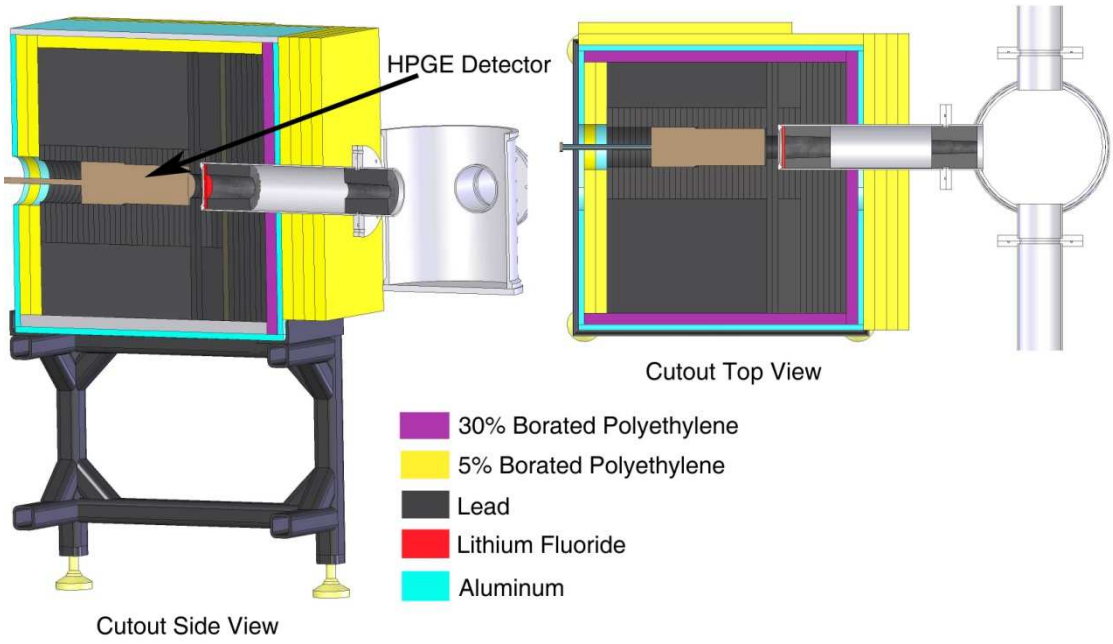


**Figure 4-31: Detector shielding (Each thickness of polyethylene in 1 inch and lead sheets are ½ inch thick)**

During the loading of these materials into the detector box, radiation measurements showed dose rates of 0.5 mR/hr gamma and 1.5 mrem/hr neutron after all the shielding was added, except for the lead past the end of the sample flight path, with the shutter open and the reactor at 1MW. The gamma dose would be expected to decrease further after the addition of the rest of the lead. However, the neutron dose would be expected to remain about the same, given that all of the polyethylene was added at this point.

According to the manufacture of the HPGe detector and Raaudorf, the threshold limit for minimal degradation of the resolution of the detector, resulting in less than 200 eV degradation from fast neutrons damage, should be approximately equal to $2 \times 10^8$ Neutrons$/cm^2$ (Advanced Measurement Technology, Inc., 2007); (Thomas W. Raaudorf, February 1984),. This value was determined from using 1.5 MeV neutrons (Thomas W. Raaudorf, February 1984). Assuming that the neutron dose rate

to the detector is not greater than 1.5 mrem/hr and using the ICRP-21 dose conversion factor for 2MeV neutrons, this would suggest that the detector has a minimum life of 5300 hours. This equates to be about 4 years of operation at the current operating tempo for the reactor.

The new detector configuration resulted in a much lower background signal with detector dead times of about 1%. There was also a considerably higher background count rate when the shutter was not evacuated. This effect was much less pronounced from first background spectrum with the temporary shielding, as shown in Figure 4-32, because of the higher count rate due to poor shielding configuration. Also, the hydrogen and aluminum peaks which were observed in the original background spectra were reduced considerably.

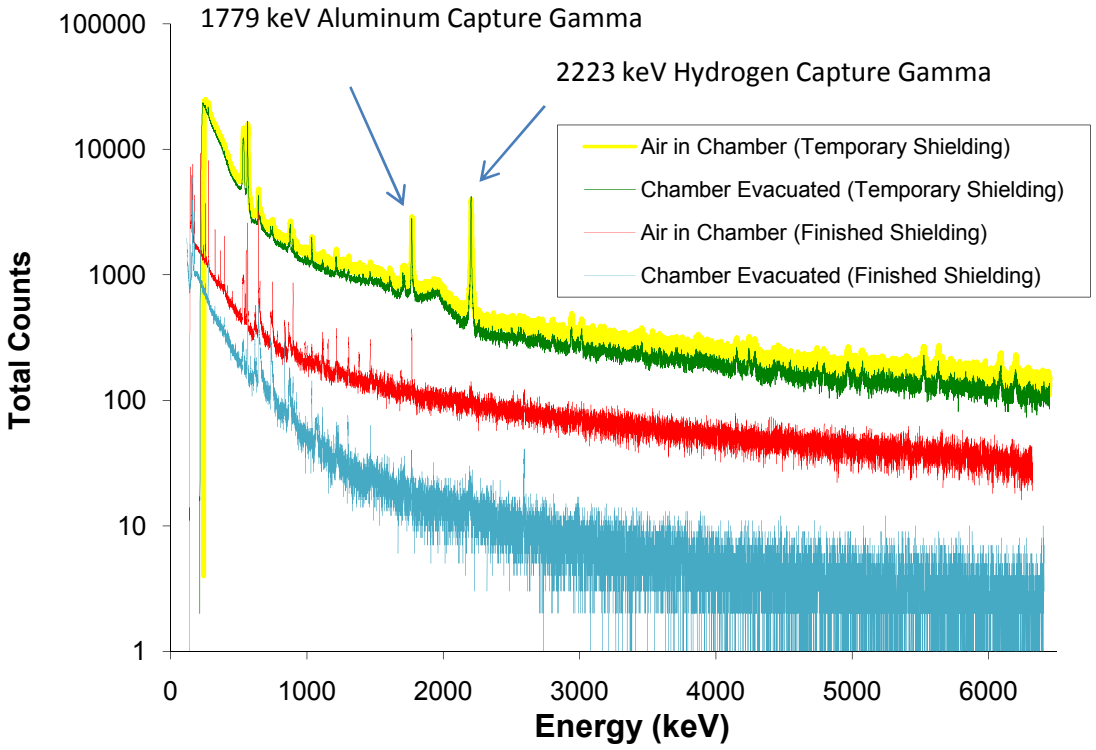


**Figure 4-32: 1 hour PGNAA background spectra with temporary shielding and final shielding configurations.**

**Table 4-7 High Purity Germanium Detector specifications**

**ORTEC PopTop**
Model No. GEM-25185-P
Serial No. 33-TP11005A
Data from ORTEC Manufacture 10-26-07

| **Dimensions** | | **Absorbing Layers** | |
|---|---|---|---|
| Detector Diameter | 62.0 mm | Aluminum | 1.0 mm |
| Detector Length | 54.6 mm | Inactive Ge | 700$\mu$m |
| End cap to detector | 4 mm | | |

| **Performance Specifications** | **Warranted** | **Measured** | **Amplifier Time Constant ($\mu$s)** |
|---|---|---|---|
| Resolution (FWHM) at 1.33 MeV, Co-60 | 2.03 keV | 1.73 keV | 6 |
| Peak-to-Compton Ratio, Co-60 | 49:1 | 68:1 | 6 |
| Relative Efficiency at 1.33 MeV, Co-60 | 22.50% | 36.50% | 6 |
| Peak shape (FWTM/FWHM), Co-60 | 1.9 | 1.86 | 6 |
| Peak shape (FWFM/FWHM), Co-60 | | 2.25 | 6 |
| Resolution (FWHM) at 122 keV, Co-57 | 935 eV | 668 | 6 |

# 5. Radiation measurements during installation and after completion of facility

Documented in this section are the radiation measurements which were used to demonstrate the adequacy of the shielding in the facility. Table 5-1 contains the radiation measurements taken at various points during the installation of the collimator. The last set of measurements showing the neutron and gamma doses exiting the collimator after installation with the reactor shutdown is perhaps the most valuable. These measurements demonstrates that the sapphire and bismuth in the collimator provide enough shielding when the reactor is shutdown to allow for the removal of the shutter during service of the facility or the beam port without dose concerns to the workers involved.

**Table 5-1 Radiation measurements during and after installation of collimator, March 17, 2008**

| Measurements taken in beam and at reactor Bioshield | Gamma (mR/hr) | Neutron (mrem/hr) |
|---|---|---|
| After removal of lead shield | 0.1 | 0 |
| After removal of wood plug | 0.1 | 0 |
| After removal of concrete plug | 40 R/hr | No measurement |
| After insertion of collimator | 2 | 0 |

The predicted gamma doses of 10-20 mrem/hr were fairly consistent with the measured value in Table 5-2. If geometric attenuation is considered between the collimator and the final beam stop this is reduced to 6-12 mrem/hr gamma dose rate. This is quite close to the measured dose rate in Table 5-3. However, in the case of the neutrons, the predicted dose rate exiting the final beam stop of 40 mrem/hr was significantly lower than the measured value during installation of 140 mrem/hr. After

these differences were corrected with additional shielding around the beam stop and the shutter, a new set of measurements was taken to show that radiation levels were reduced to an acceptable level. These measurements are tabulated in Table 5-4, Table 5-5 and Table 5-6.

**Table 5-2: Dose rates after installation of collimator with shutter and beam stop in position, March 19/2008**

| Reactor power and Shutter position | Shutter position | On Sides of Shutter next to Bioshield of reactor | | In Beam line | |
|---|---|---|---|---|---|
| | | Gamma mR/hr | Neutron: mrem/hr | Gamma mR/hr | Neutron: mrem/hr |
| | | 0.4 | 0.5 | 0 | 0 |
| 10 kW | Closed | 1.8 | 3 | 0.4 | 3.5 |
| 100 kW | Closed | 12 | 50 | 18 | 35 |
| 1 MW | Closed | | 150 | 30 | 200 |
| Doses exiting Beam stop with shutter open and reactor power 100 kW | | 0.5 mR/hr and 15 mrem/hr | | | |

**Table 5-3: Dose measurements at 1MW around beam stop with shutter open after initial installation of bioshield, May 13/2008**

| Measurement location | Gamma mR/hr | Neutron mrem/hr |
|---|---|---|
| **Left side:** Next to front* | 60 | 70 |
| **Left side:** All of side except front | 60 | 70 |
| **Right side:** Next to front | 12 | 90 |
| **Right side:** All of side except front | 6 | 80 |
| **Top:** Near front | 12 | 90 |
| **Top:** All of top except front | 6 | 70 |
| Back | 6 | 140 |
| *Front (side of beam entrance) | | |

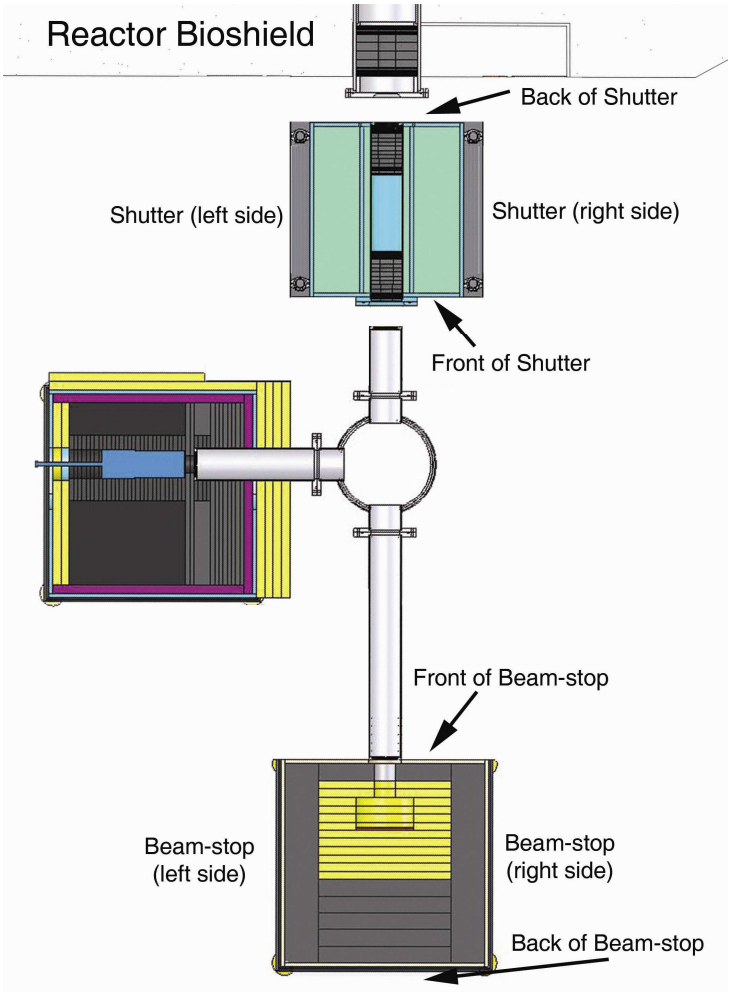


**Figure 5-1: PGNAA diagram for location of radiation measurements in tables 5.2-5.3**

**Table 5-4: Dose Measurements at 1MW around concrete block structure placed around beam stop June 10/2008**

| | **Left Side** | | **Right Side** | |
|---|---|---|---|---|
| | Gamma (mR/hr) | Neutron (mrem/hr) | Gamma (mR/hr) | Neutron (mrem/hr) |
| Front Beam Height | 4 | 20 | 5 | 20 |
| Middle Beam Height | 0.5 | 2 | 0.5 | 1 |
| Back Beam Height | 0.2 | 1 | 0.2 | 1 |
| | **Top ( Two courses of bricks)** | | **Top ( Four courses of bricks)** | |
| | Gamma (mR/hr) | Neutron (mrem/hr) | Gamma (mR/hr) | Neutron (mrem/hr) |
| Center Beam Line | 0.6 | 15 | BKG | 1.5 |
| Front Beam line | BKG | 28 | BKG | 18 |
| Back (Beam exiting side)= Non distinguishable from background levels (gamma and neutron) | | | | |

**Table 5-5: Bioshield neutron and gamma dose measurements after adding additional neutron shielding inside shutter bioshield, July 2/2008 (Shutter Closed Reactor Power 1MW)**

| **Right Side** | | | | | | |
|---|---|---|---|---|---|---|
| | **Top** | | **Middle** | | **Bottom** | |
| | Gamma (mR/hr) | Neutron (mrem/hr) | Gamma (mR/hr) | Neutron (mrem/hr) | Gamma (mR/hr) | Neutron (mrem/hr) |
| Front | 1 | 1 | 1 | 1 | 0.5 | 0.5 |
| Middle | 1.5 | 0.5 | 2.5 | 2 | 1.5 | 1 |
| Back* | 2 | 1 | 6 | 6 | 2.5 | 2.5 |
| **Left Side** | | | | | | |
| | **Top** | | **Middle** | | **Bottom** | |
| | Gamma (mR/hr) | Neutron (mrem/hr) | Gamma (mR/hr) | Neutron (mrem/hr) | Gamma (mR/hr) | Neutron (mrem/hr) |
| Front | 0.5 | 1 | 1 | 1.5 | 1 | 1 |
| Middle | 1 | 1.5 | 3 | 4.5 | 1.5 | 1.5 |
| Back* | 2 | 2 | 11 | 20 | 2 | 2.5 |
| **Front** | | | | | | |
| | **Top** | | **Middle** | | **Bottom** | |
| | Gamma (mR/hr) | Neutron (mrem/hr) | Gamma (mR/hr) | Neutron (mrem/hr) | Gamma (mR/hr) | Neutron (mrem/hr) |
| Left Side | 1 | 0.5 | 1 | 1 | 0.5 | 0.5 |
| Middle | 1 | 1 | 2** | 12** | 0.5 | 0.5 |
| Right Side | 1 | 1 | 1 | 1 | 0.5 | 0.5 |

* Next to Reactor Bioshield
** In Sample Chamber

**Table 5-6: Bioshield neutron and gamma dose measurements after adding additional neutron shielding inside shutter bioshield, July 2/2008 (Shutter Open Reactor Power 1MW)**

| **Right Side** | | | | | | |
|---|---|---|---|---|---|---|
| | **Top** | | **Middle** | | **Bottom** | |
| | Gamma (mR/hr) | Neutron (mrem/hr) | Gamma (mR/hr) | Neutron (mrem/hr) | Gamma (mR/hr) | Neutron (mrem/hr) |
| Front | 1.5 | 5 | 3.5 | 8 | 2.5 | 7.5 |
| Middle | 1.5 | 2.5 | 6 | 5 | 3.5 | 3 |
| Back* | 1.5 | 2.5 | 8 | 6 | 3.5 | 4 |
| **Left Side** | | | | | | |
| | **Top** | | **Middle** | | **Bottom** | |
| | Gamma (mR/hr) | Neutron (mrem/hr) | Gamma (mR/hr) | Neutron (mrem/hr) | Gamma (mR/hr) | Neutron (mrem/hr) |
| Front | 1.5 | 5 | 3.5 | 10 | 2.5 | 8 |
| Middle | 1.5 | 3 | 6 | 6 | 3 | 5 |
| Back* | 1.5 | 3 | 11 | 22 | 3 | 5 |
| **Front** | | | | | | |
| | **Top** | | **Middle** | | **Bottom** | |
| | Gamma (mR/hr) | Neutron (mrem/hr) | Gamma (mR/hr) | Neutron (mrem/hr) | Gamma (mR/hr) | Neutron (mrem/hr) |
| Left Side | 1.5 | 10 | 6 | 30 | 4 | 20 |
| Middle | 1.5 | 10 | 18 R/hr** | >10,000** | 6 | 25 |
| Right Side | 1.5 | 10 | 6 | 35 | 3 | 20 |

* Next to Reactor Bioshield

** In Sample Chamber

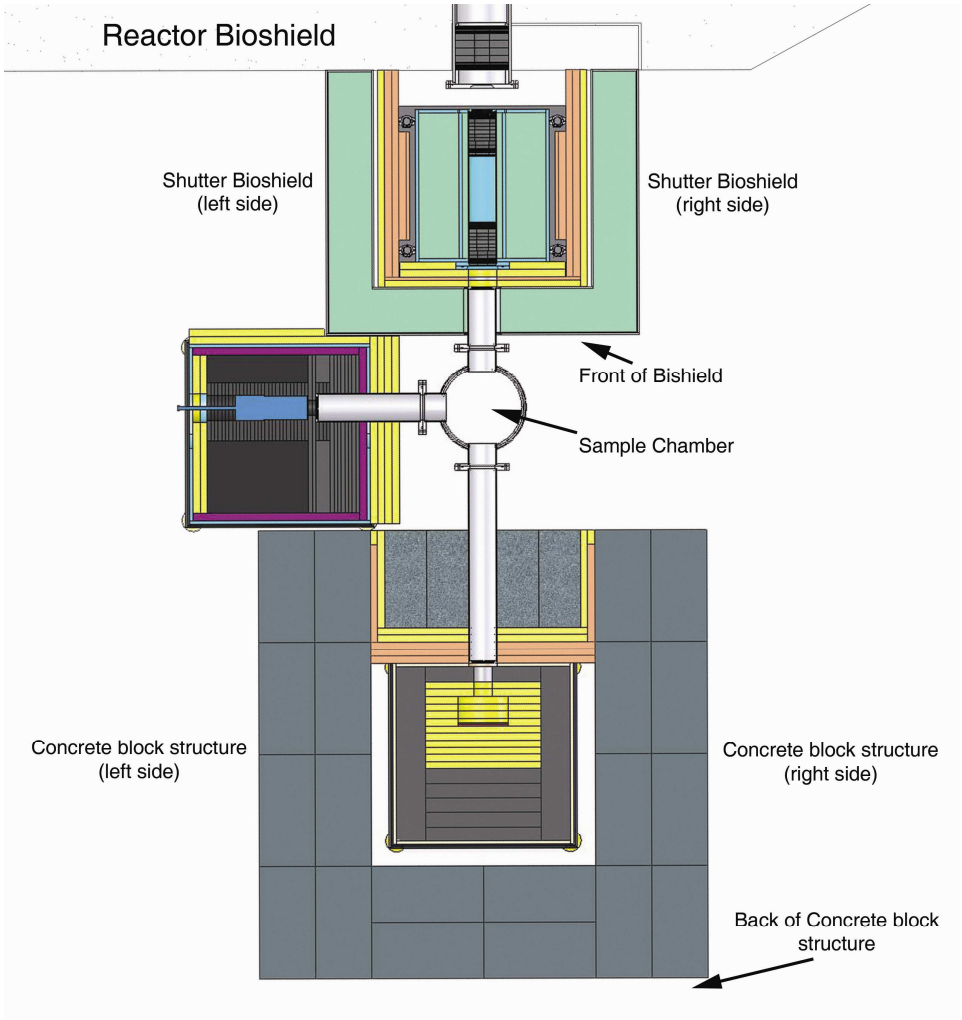


**Figure 5-2: PGNAA diagram for location of radiation measurements in tables 5.4-5.6**

# 6. Operation and controls of facility

## *6.1. Controls and Safety Interlocks*

Since there is a high-intensity neutron beam passing through the sample chamber when the shutter is open, it is important that there be engineered and administrative controls to prevent accidental exposures to the neutron beam as well as provide efficient and simple operation of the facility. Administrative safety controls, which are important, will not be discussed here because they were not directly considered in the design of this facility.

The controls for the facility consist of a shutter control box, and a gauge board with a series of three way valves to control the evacuation and back filling of the collimator, shutter, sample chamber, and beam tubes. The shutter control box, which is fastened to the reactor bioshield on the detector side of the facility is shown in Figure 6-1.


**Figure 6-1: Shutter Control Box**

When the shutter open button is pressed, power is applied to a 3-way solenoid valve, sending air to the cylinder which raises the shutter beam stop. When the close button is pressed, power is lost to the solenoid valve and the shutter pneumatic cylinder is vented, causing the shutter beam stop to lower to the closed position. To prevent the shutter from being opened when the sample chamber lid is removed, there is a limit switch installed on the sample chamber lid. To give the reactor operator full control of the facility, there is a permissive switch on the reactor console. If either the

sample chamber lid is removed or the reactor permissive switch is turned off, power is lost to the shutter control circuitry and the shutter defaults to the closed position. LED lights on the control box are used to provide the user notification of the status of the shutter permissive, shutter position (closed, intermediate, or open), and whether the sample chamber lid is installed or removed. A schematic diagram of the relays and wiring for the shutter control is provided bellow.

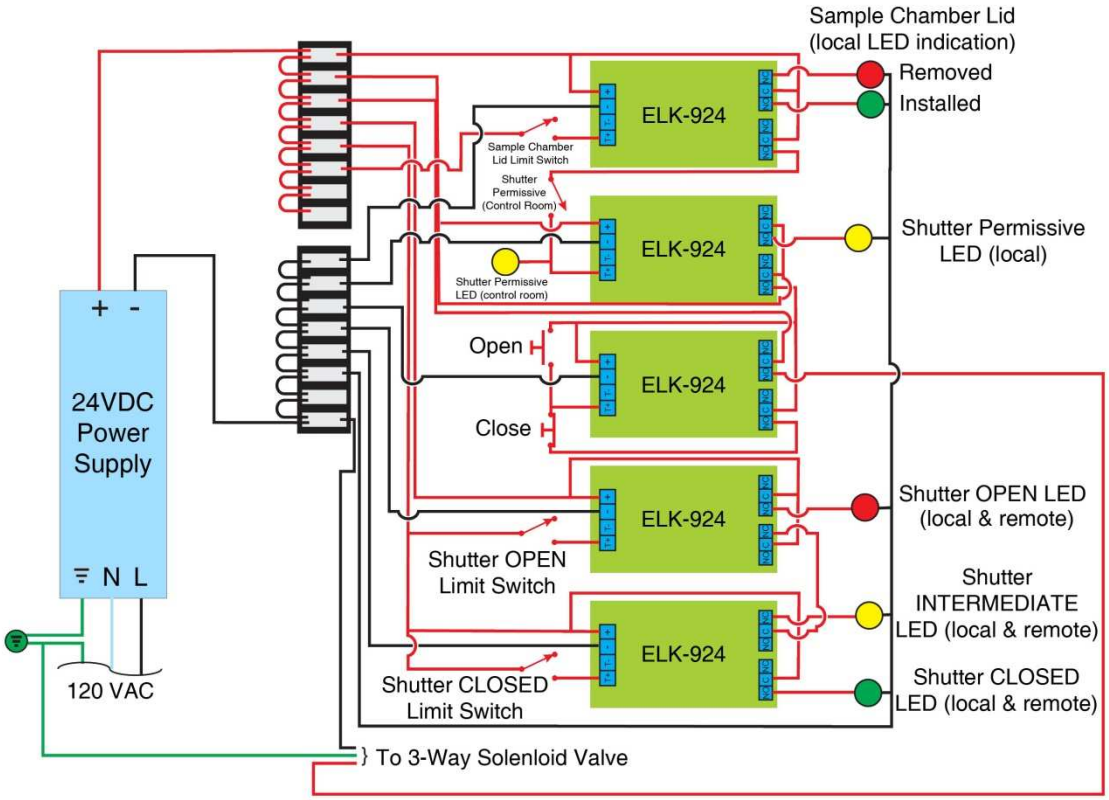


**Figure 6-2: Schematic diagram of shutter control circuitry (Note: ELK-924 is a 1.2 mA trigger sensitive relay module produced by (ELK Premium Products for Security & Automation))**

Aside from the shutter controls, there are also a set of controls for evacuating or back filling the collimator, shutter beam tubes, and sample chamber with helium. These controls are located on the shutter bioshield next to the sample chamber entrance and consist of a set of three way valves allowing each component to be isolated or switched to a vacuum pump or helium cylinder as shown in Figure 6-3.

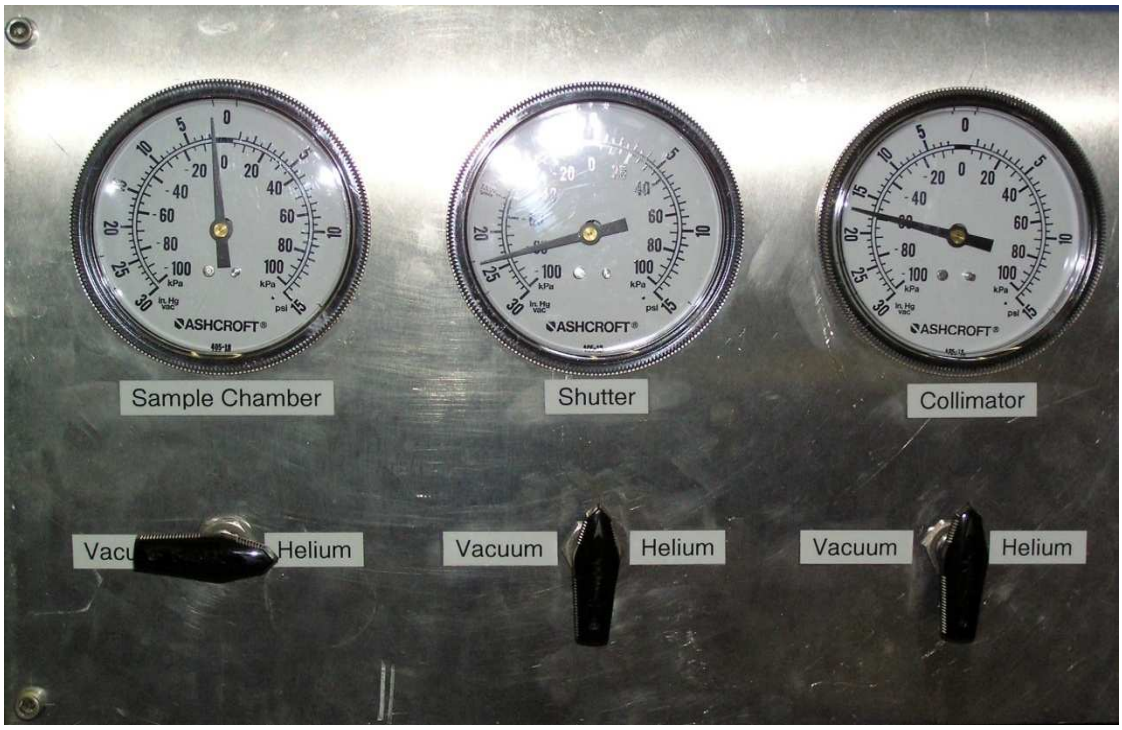


**Figure 6-3: shutter evacuation and fill controls**

Since the collimator and shutter beam tube are both air tight, it should not be necessary to evacuate and back fill them regularly. *(It is important to note that the collimator should only be evacuated after the reactor has been shutdown for an extended period of time. Otherwise a significant amount of* $^{41}Ar$ *can be introduced into the room which is produced from* $^{40}Ar$ *within the air which is in the collimator. The half life for this isotope is approximately 1.8 hours.)* The sample chamber needs to be evacuated each time a sample is loaded. Shown in Figure 6-4 is a schematic diagram of the evacuation and filling system. Each component is protected by a pressure relief valve preset to vent at 5psig. This prevents damage to the aluminum thin-windows in the event of a buildup of pressure.

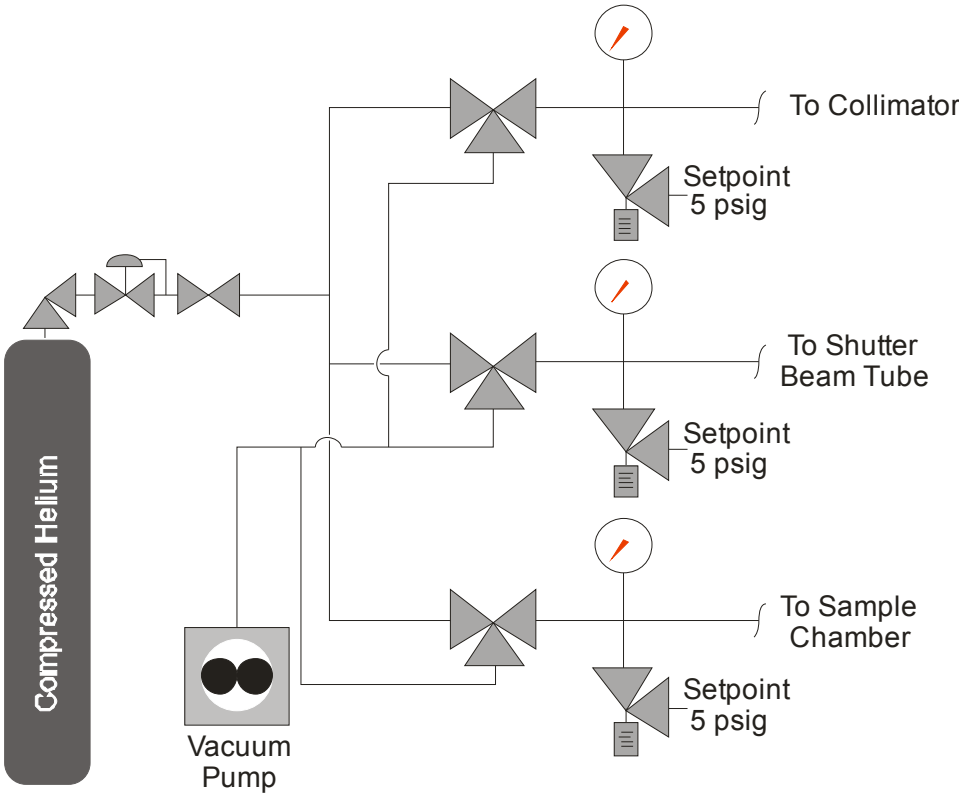


**Figure 6-4: Schematic diagram of shutter evacuation and fill system**

### *6.2. Sample Preparation and Irradiation*

When samples are irradiated, it is important that the geometry of the sample be such that there is a minimal amount of self shielding within the sample, otherwise quantitative analysis becomes more difficult. This is important when considering what standards are to be used when determining elemental quantities. For many samples, this is accomplished by pressing the sample material into a thin disk shaped pellet using a pellet die. The pellet needs to be small enough such that the entire pellet will be fully bathed by the uniform center portion of the neutron beam. The pellet is then held in the beam by the sample holder positioned at a $45^{o}$ angle to the neutron beam. This not only moves the sample holder post out of the flight path of the detector, it also minimizes self shielding of the gammas produced in the direction of the detector.

If pressing the material is not possible, another option is to heat seal them into a Teflon® pouch. If this method is used, as much air as possible should be pressed out of the pouch before it is sealed to prevent it from bursting when the sample chamber is evacuated.

Since the amount of the analyte in the sample is directly proportional to the measured capture gamma rate, it is important that a standard with a known amount of the analyte be run in a similar configuration to the sample. If the sample contains a large amount of hydrogen or some other substance which could influence the neutron exposure within the sample, it is important this be taken into consideration when preparing a standard.

# 7. Characterization of facility

## *7.1. Neutron Beam*

The neutron beam for the facility was characterized using radiograph imaging plates and gold and nickel foils. The radiograph imaging plates were used to determine the dimensions, shape, uniformity, and location of the neutron beam. The imaging plates used were a BAS-ND neutron imaging plate, which is manufactured by Fujifilm (FUJIFILM Global, 2008). These plates contain a photo-stimulable phosphor which produces "Photo-stimululated luminescence" (PSL). This means that the substance emits light after a second stimulation by light with a longer wavelength than the wavelength of the first stimulation. The BAS-ND neutron imaging plates contain BaFBr:$Eu^{+2}$, where $Eu^{+2}$ is used as the fluorescence center, which is used widely for x-ray imaging (Batentschuk, Winnacker, Schuwartz, & Trautmann, 2007) and $Gd_2O_3$, which is used as a neutron converter. When neutrons interact with the gadolinium in $Gd_2O_3$ internal conversation electrons are produced. The electrons cause photons of light to be emitted, which excite the BaFBr:$Eu^{+2}$ to a metastable state. The plates are then scanned with A BAS-500 scanner produced by FUJIFILM, which has a laser of wavelength such that the electrons trapped in the metastable state are further excited and immediately decay back to the ground state, emitting a luminance of blue light. The light is captured through a photomultiplier tube to produce a signal which is transferred into a two dimensional image of the intensity.

Using this system, radiograph images and plots of intensity as a function of position across the center of the beam were produced at 5 inch intervals between the shutter bioshield and the beam stop. Figure 7-2 indicates how the diameter was

determined for the radiograph taken at the sample position. Shown in Figure 7-3 and Figure 7-4 , the beam profile plots were used to produce a plot of the main beam diameter, as well as the maximum diameter of the umbra as a function of distance from the bioshield out to the beam stop. It was determined from these results that the umbra and penumbra had diameters of approximately 2.04 cm and 6 cm, respectively, at the sample location and the maximum diameter of the beam was 10 cm at the beam stop.

There also appeared to be a focal point for the penumbra approximately 25 cm from the beam stop. This is the point at which the beam would be focused to a point providing the collimators were continued with the same taper to this point. Since they are not and the last collimator has a diameter of approximately 3.7 cm, the penumbra can never have a diameter less than 3.7 cm. This is because at any point directly in front of the collimator there will always be a 3.7 cm diameter portion of the source visible. The reason this does not show up in the plot is because this 3.7 diameter portion of the source is relatively small in comparison to the whole source. The point which appears to be the focal point is the distance from the collimator for which the whole source can only be seen at a point.

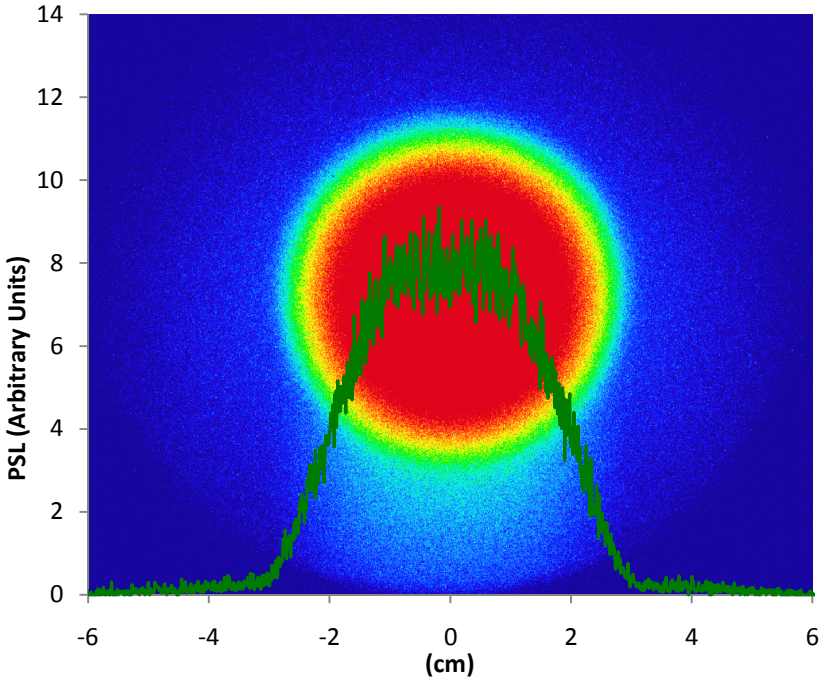


**Figure 7-1: Beam profile at sample location, reactor power 10 kW**

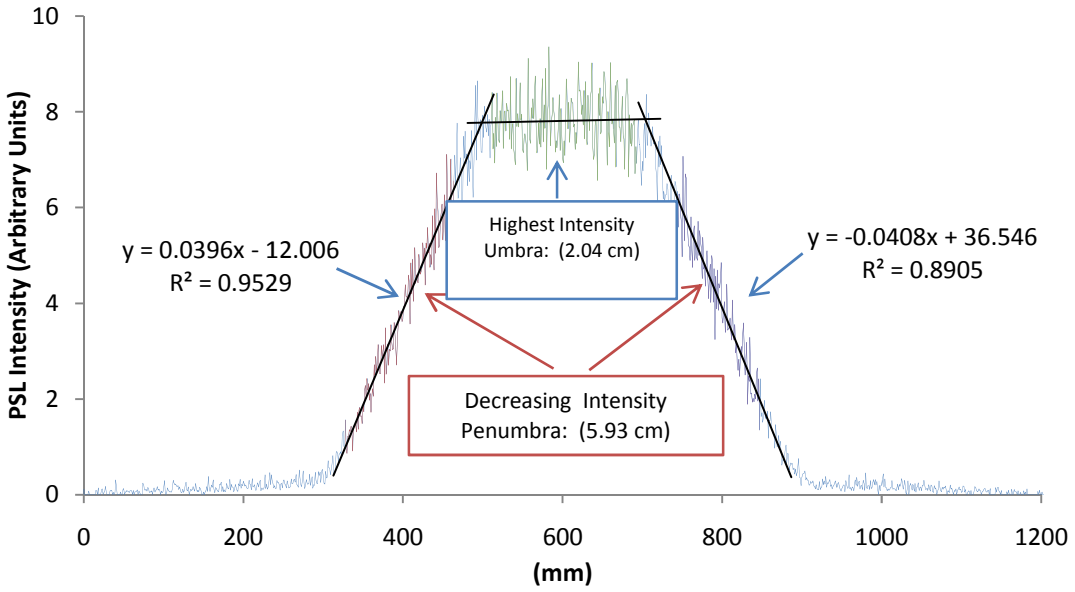


**Figure 7-2: Radiograph Beam Profile at Sample Location, Reactor power 10 kW and shutter opened approximately 25 seconds**

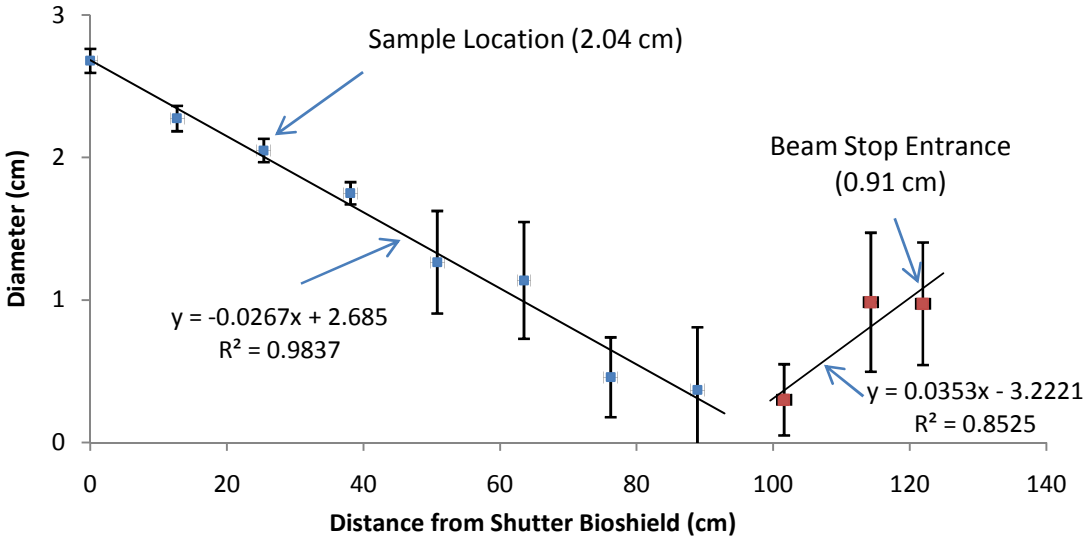


**Figure 7-3 Radiograph Measurements of Main Beam Diameter (Umbra)**

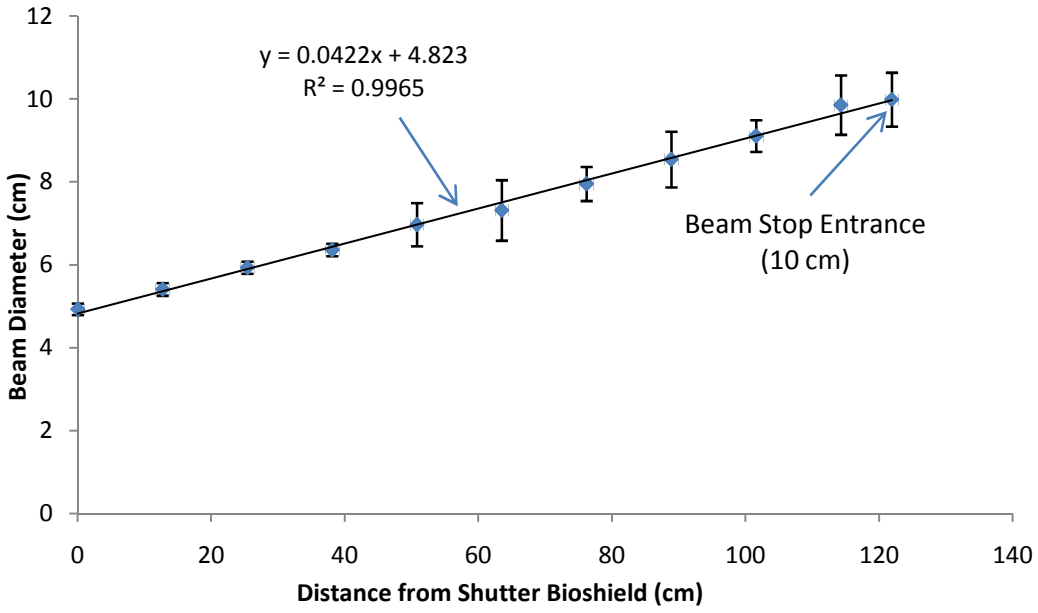


**Figure 7-4: Radiograph Measurements of total Beam Diameter (Penumbra)**

Gold and nickel foils were used to determine the fast and thermal flux of the beam. This was done by placing cadmium-covered and bare gold foils in the beam. The resulting activity of the cadmium covered and bare gold foils were measured and decay corrected to determine the epithermal and thermal flux of the beam. These flux measurements were made both before and after the fuel change in the reactor. The measurements taken after the core change did not show an appreciable change in the epithermal or thermal neutron flux of the beam. These results are all tabulated in Table 7-1. The flux measurements which were taken on 6/1/08 and 7/10/08, were both taken before the facility was completely constructed. This lead to possible errors associated with estimates of where the exact sample location would be. Also, the Ni measurement does not report an epithermal flux because the activity generated after 7 hours in the beam with a cadmium cover was not measurable. Additionally there is a much larger uncertainty associated with the Ni thermal flux measurement because the efficiency calibration had a greater degree of uncertainty then that which was used for Au measurements. Therefore, the best estimate of the actual flux for the beam would be the Au foil measurement taken after the core change. The thermal flux for the facility was measured to be $2.8\times10^{7} \pm 5.13\times10^{5}$ neutrons/cm$^2$/s with a cadmium ratio of approximately 106±3. This flux measurement is approximately three times the magnitude of the flux measured at the University of Texas and 60% of the magnitude of the thermal flux at the Budapest facility (Revey, Harrison, Alvarez, Biegalski, & Landsberger, 2007) (Belgya, Revay, & Molnar, 2004). It is also a factor of ten less than the measured flux for the thermal PGNAA facility at NIST, which has a cadmium ratio of 175 calculated from their measured thermal and epithermal neutron flux and

the neutron cross sections use for the measurements made for this facility (Mackey, Anderson, Liposky, Lindstrom, Chen-Mayer, & Lamaze, 2004).

**Table 7-1: PGNAA Flux measurements**

| PGNAA Facility Beam flux Measurements (In Sample Position) | | | | |
|---|---|---|---|---|
| | | Thermal (Bare Au) | Epithermal (Cd covered Au) | |
| Foil | Date | Neutrons/cm$^2$/s | Neutrons/cm$^2$/s | Cadmium Ratio |
| | | Before Core Change HEU Fuel | | |
| Au | 6/1/2008 | 3.85E+07 ± 4.24E+05 | 1.49E+04 ± 1.64E+02 | 166 ± 3 |
| Au | 7/10/2008 | 3.03E+07 ± 2.84E+05 | 1.97E+04 ± 1.85E+02 | 99.0 ± 1 |
| Au | 8/1/2008 | 2.98E+07 ± 5.28E+05 | 1.48E+04 ± 2.62E+02 | 129 ± 3 |
| | | After Core Change LEU Fuel | | |
| Au | 11/12/2008 | 2.81E+07 ± 5.13E+05 | 1.70E+04 ± 3.11E+02 | 106 ± 3 |
| Ni | 11/6/2008 | 4.42E+07 ± 1.55E+07 | NA | |
| Note: Uncertainties include uncertainties for both the detector efficiency of the measurement as well as the counting statistics | | | | |

## *7.2. Characterization of Detection Capabilities*

In order to characterize the detector and to determine the detection capabilities for the facility, an absolute efficiency curve for the detector was produced with a combination of check sources and prompt gamma spectra for various targets. Background spectra were used to determine measured elements within the background, and spectra for three NIST standards as well as polyethylene were produced using the facility to obtain sensitivities and minimal detection capabilities for the facility. The NIST standards were 1633a (Coal Fly Ash) and, 1571 (Orchard Leaves) with approximate sample sizes of 1 gram.

Sensitivity (S) is defined as the counts per second per milligram in a specific sample of a specific mass (Currie, 1968) and (Dzubay, 1977).

$$\boldsymbol{S = (counts/s)/mg} \qquad 7\text{-}1$$

The detection limit ($L_d$) for an analyte is defined as the smallest concentration of that analyte present for which it can be reliably detected and distinguished from background (Currie, 1968) and (Dzubay, 1977). In other words, the concentration must be great enough to minimize the chance of a false positive (decision that the analyte is present when it is not) and a false negative (decision that that the analyte is not present when it is). Thus a critical level ($L_c$) is determined such that if the measured value is greater than this value, the probability ($\beta$) that the measured value is due to background and the probability ($\alpha$) that the measured value is not due to the sample are both sufficiently small to prevent a false positive outcome. An illustration of this is presented in Figure 7-5. This leads to the following equations for the critical

level which is based on the standard deviation ($\sigma_0$) when a sample is not present for which the net measurement is 0 and the detection limit ($L_d$), which is based on $\sigma_D$, for which the net signal from the sample is equal to $L_c$.

$$L_c = k_\alpha \sigma_0 \qquad 7\text{-}2$$

$$L_d = L_c + k_\beta \sigma_D \qquad 7\text{-}3$$

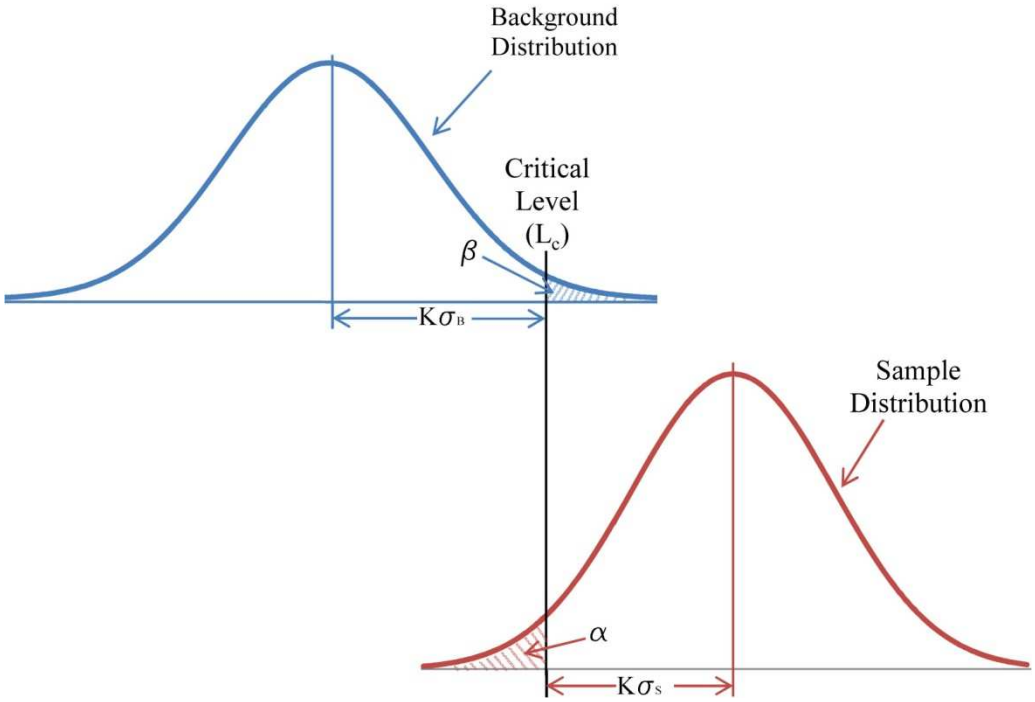


**Figure 7-5: Illustration of Background and sample distribution representing the critical level. $\beta$ is the probability that the measured values is due to the background and $\alpha$ is the probability that the measured value is not due to the sample.**

Typically, these values of $\alpha$ and $\beta$ are both chosen to equal to 0.05, leading to a 95% probability that a false positive will not be detected. It is assumed that the data is Gaussian distributed. Thus $\alpha=\beta$ and therefore $k_\alpha=k_\beta=k$, which leads to the following simplification of Equation 7-3,

$$\boldsymbol{L_d = k(\sigma_o + \sigma_D)} \quad \text{7-4}$$

Also, if $\sigma$ is assumed to be approximately constant then,

$$\boldsymbol{L_c = k_\alpha \sigma_0 = 1.64\sigma_0} \quad \text{7-5}$$

$$\boldsymbol{L_d = 2L_c = 3.29\sigma_0} \quad \text{7-6}$$

Finally, this leads to the determination of $\sigma_o$, which is the standard deviation when the concentration is equal to 0. For the case of prompt gamma activation analysis, the concentration can be estimated as, $(N_G\text{-}N_B)/(S*t)$, where $N_G$ is the gross number of count, $N_b$ is the number of background counts, $S$ is the sensitivity defined above, and $t$ is the count time. Also, if the probability distribution is assumed to be Poisson, given that the probability of interaction with a particular atom is extremely improbable, then $\sigma$ is equal to the square root of the number of counts. Thus, taking into account the sensitivity and the irradiation time $\sigma_o$ becomes,

$$\boldsymbol{\sigma_o = \frac{\sqrt{N_B}}{S*t} = \frac{\sqrt{R_b/t}}{S}} \quad \textbf{7-7}$$

where $R_b$ is the background count rate.

Therefore, the detection limit for PGNAA can be determined by,

$$\boldsymbol{L_d = 3.29\frac{\sqrt{R_b/t}}{S}} \quad \text{7-8}$$

One significant improvement was achieved in an effort to reduce the 477keV gamma in the background associated with the boron within the shielding materials. This was addressed by the addition of machined lead collimators between the detector and the sample to fill the space between the existing lead collimators in the original design as shown in Figure 7-6.

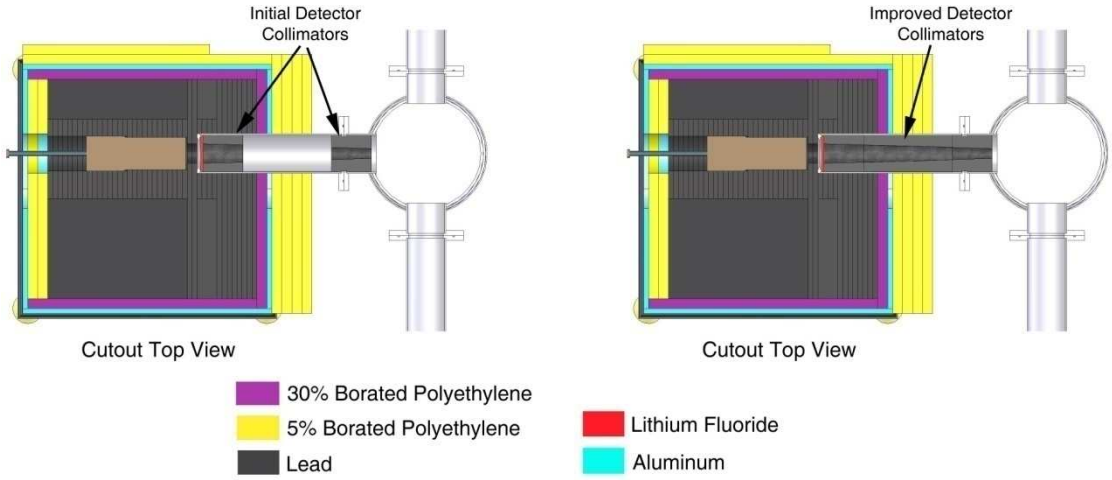


**Figure 7-6: Illustration of improved detector collimators**

As a result, some of the data in the following sections was taken before this change was made. In order to avoid confusion the data will be distinguished as before or after improved detector shielding, whichever is the case.

**Efficiency Curve**

An absolute efficiency curve was obtained for the detector at the sample location, using a combination of check sources placed in the sample location, and PGNAA spectra. The check sources were used to determine efficiencies below 2 MeV, and the PGNAA spectra determine efficiencies for energies greater than 2 MeV. The check sources used were $^{60}$Co, $^{133}$Ba, and $^{137}$Cs. Absolute efficiencies were based on the yields for the emitted gamma energies, and the disintegrations per second which were calculated from the decay corrected activities. The efficiency curve was produce by a five degree polynomial relating the logarithm of the efficiency to the logarithm of the energy as described by Knoll (Knoll, 2000)

$$\ln(\epsilon) = \sum_{i=1}^{5} a_i \left( ln \frac{E}{E_o} \right)^{i-1} \qquad \textbf{7-9}$$

where $\in$ is the efficiency, E is the energy, and $E_0$ is a reference energy.

The isotopes used for the efficiency curve using PGNAA spectra were Ni, Cl, and Na. Since the energy distribution for the neutron beam was not well known it was not possible to determine efficiencies based on the reaction rates. Instead the measured yields for the specific isotopes were used to extrapolate beyond the efficiency curve determined from the check source measurements to obtain efficiencies beyond 2MeV. This was done by using the count rates for gammas emitted for each isotope within the measured check source efficiency curve to determine the production rate for these gammas. Then, based on these production rates and relative yields, approximate production rates for the higher energy gamma-rays were obtained. These production

rates were then used to determine efficiencies beyond the check source energies. The relative yields used were those published by (Brookhaven National Laboratory, 2008).

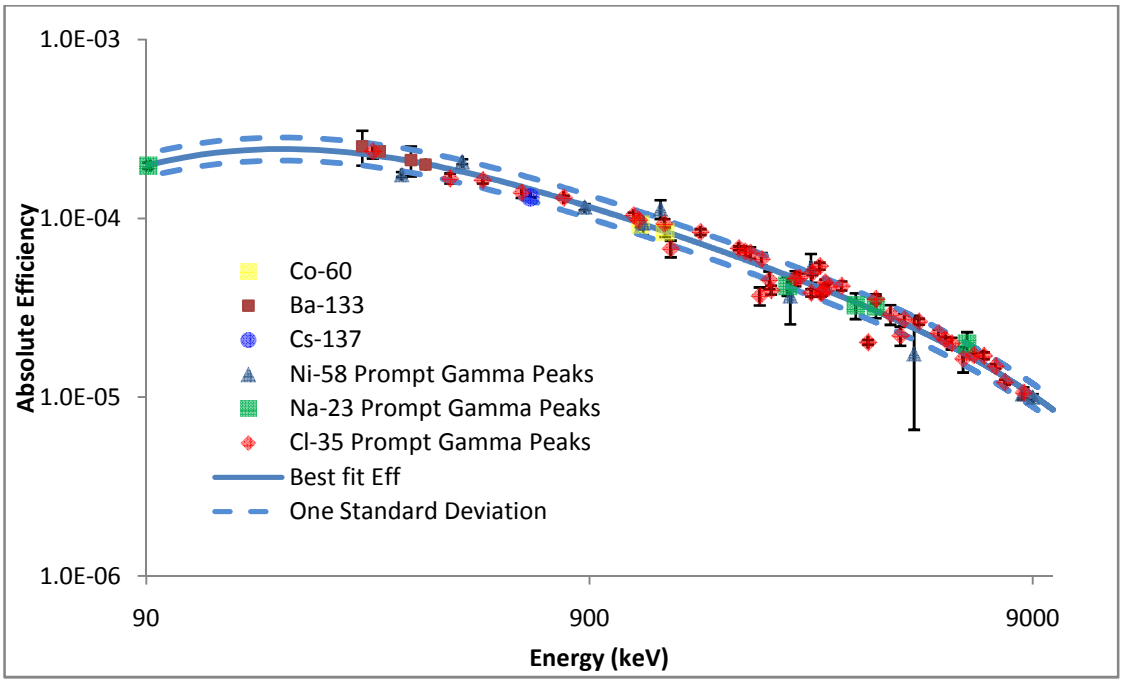


**Figure 7-7: PGNAA Absolute detector efficiency with source at sample location**

**Background Spectra**

A detailed analysis of two background spectra taken before the improved detector collimator, both with and without the sample chamber evacuated, are presented in Figures 7-8 to 7-18. The hydrogen, boron, and lead peaks are mostly from the polyethylene, paraffin, borated polyethylene, boral, and lead shielding in the detector shielding, beam stop, shutter, and biological shield. Aluminum peaks are from the aluminum sample chamber, aluminum beam tubes, aluminum support structure, and the aluminum surrounding the germanium crystal in the detector. Iron peaks are from the steel supporting structure within the facility. Nitrogen, which is only seen in the spectrum without the sample chamber evacuated, is from the air in the sample chamber which is approximately 78% nitrogen.

Besides the prominent peaks listed above, there are a large number of prompt and decay germanium peaks. Most of the germanium peaks are similar to that of typical decay and prompt gamma peaks. These are due to activation of the germanium in the detector as well as exited compound nuclei decay from thermal neutron interactions. Some of these peaks however are broadened on the high energy side creating triangular shaped peaks, for example the peaks at 595.9 keV and 691.3 keV, which are primarily a result of the decay of exited nuclei from $^{74}$Ge and $^{72}$Ge. These peaks are what are known as “germanium triangles”, and are a result of inelastic scattering of fast neutrons within the detector. The broadening of these peaks is caused by electron-hole pairs created from the recoiling germanium atom, which is dependent on the scattering angle of the recoil nucleus. A further and more detailed analysis of the effects of neutron interactions within germanium detectors was conducted by Chasman, Jones, & Ristinen (Chasman, Jones, & Ristinen, 1965). Also, a possible

technique for determining the spectral distribution and flux of the fast and thermal neutrons was developed by Skoro (Skoro, et al., 1992).

Presented in Figure 7-19 and Figure 7-20 is a comparison of the background measurements both before and after improving the detector collimator. Over all the total background was reduced by about a factor of two over the entire energy range and as much as a factor of 4 to 8 from 70-300 keV. The most significant change, however, was the reduction in the count rate for the boron peak from 1.77 cps to 0.05 cps, as shown in Figure 7-20 and Table 7-2. This is especially important since PGNAA is commonly use for quality control of boron concentrations in many manufacturing processes for which boron levels need to be measured in very low concentrations.

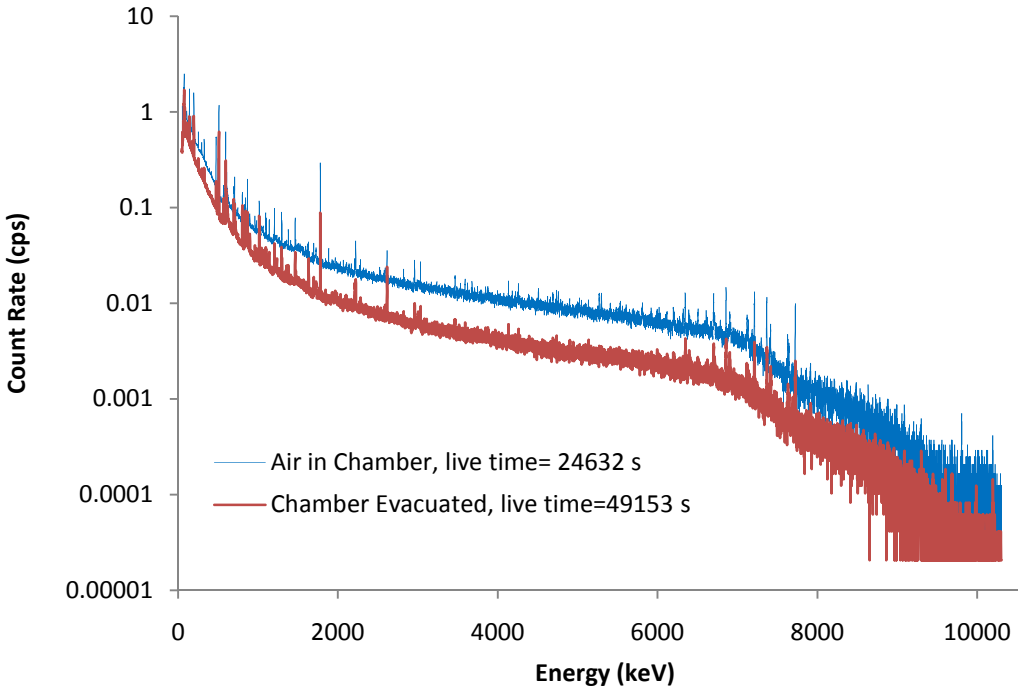


**Figure 7-8: PGNAA Background Spectra before improved detector collimator, (Reactor power 1MW, and Teflon sample pouch in beam)**

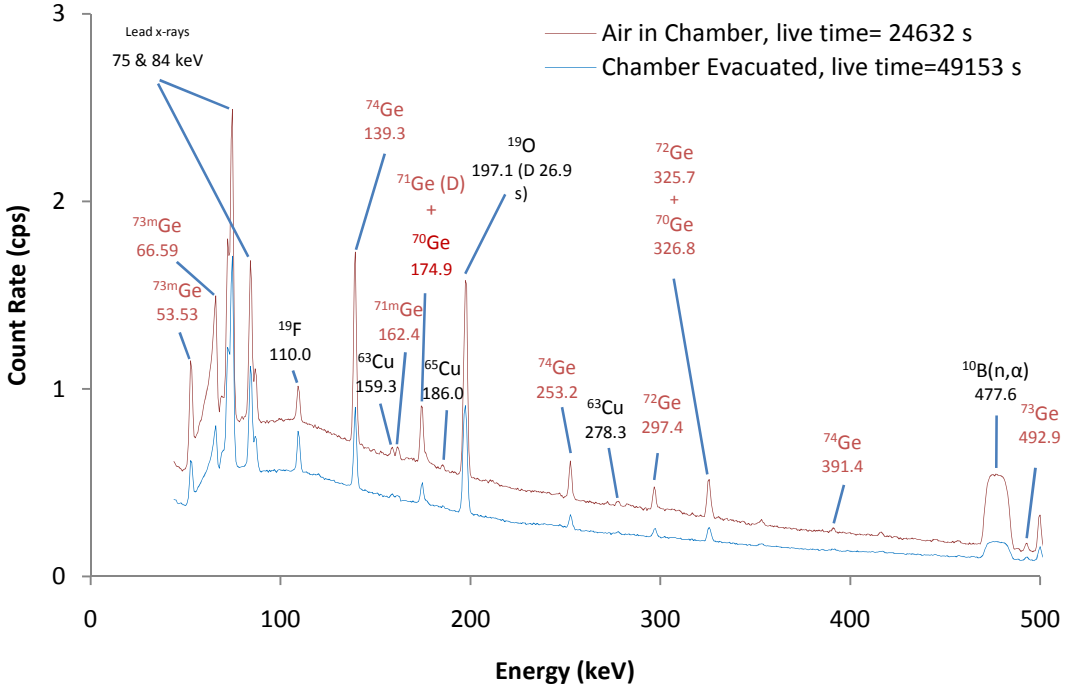


**Figure 7-9: PGNAA Background Spectra before improved detector collimator 0-500 keV, (Reactor power 1MW, and Teflon sample pouch in beam)**

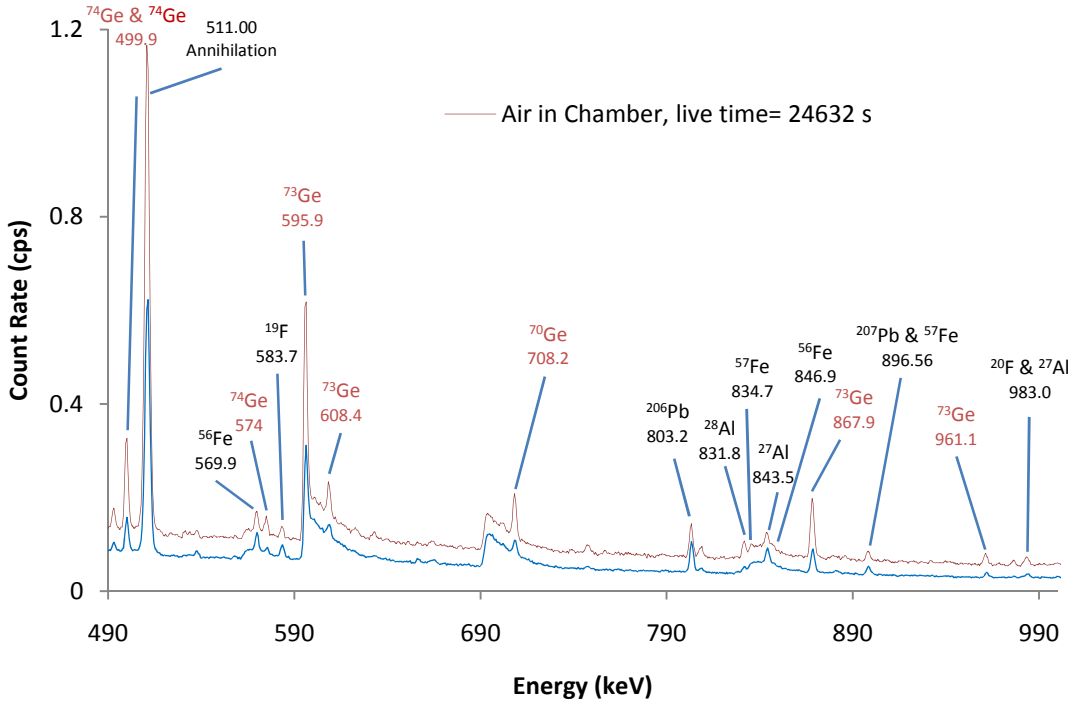


**Figure 7-10: PGNAA Background Spectra before improved detector collimator 500-1000 keV, (Reactor power 1MW, and Teflon sample pouch in beam)**

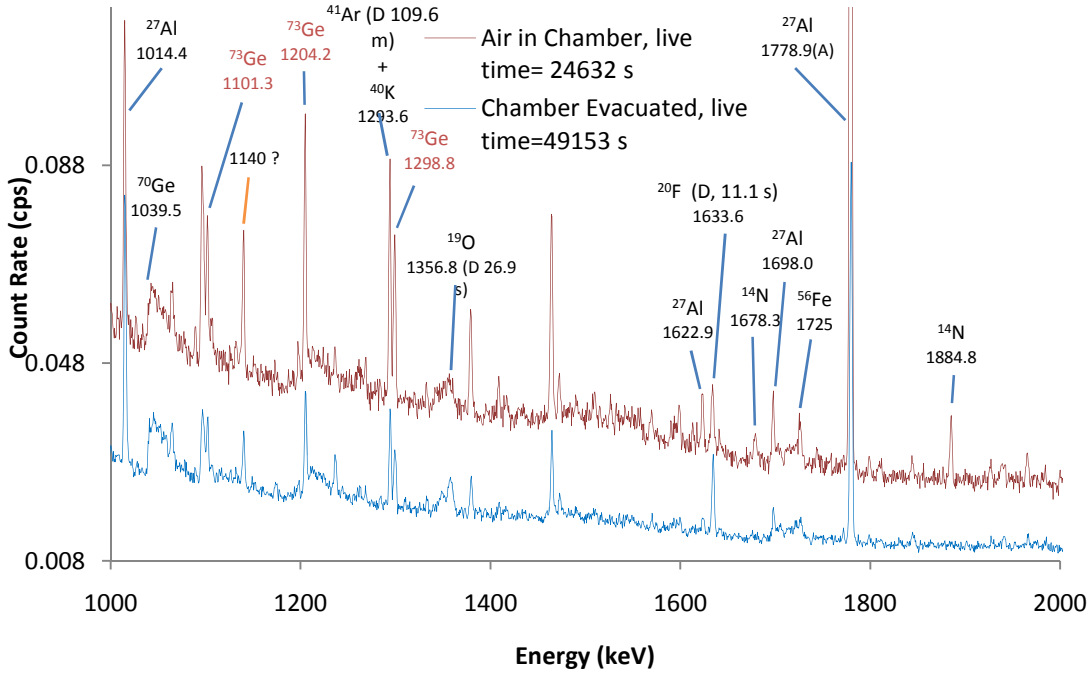


**Figure 7-11: PGNAA Background Spectra before improved detector collimator 1000-2000 keV, (Reactor power 1MW, and Teflon sample pouch in beam)**

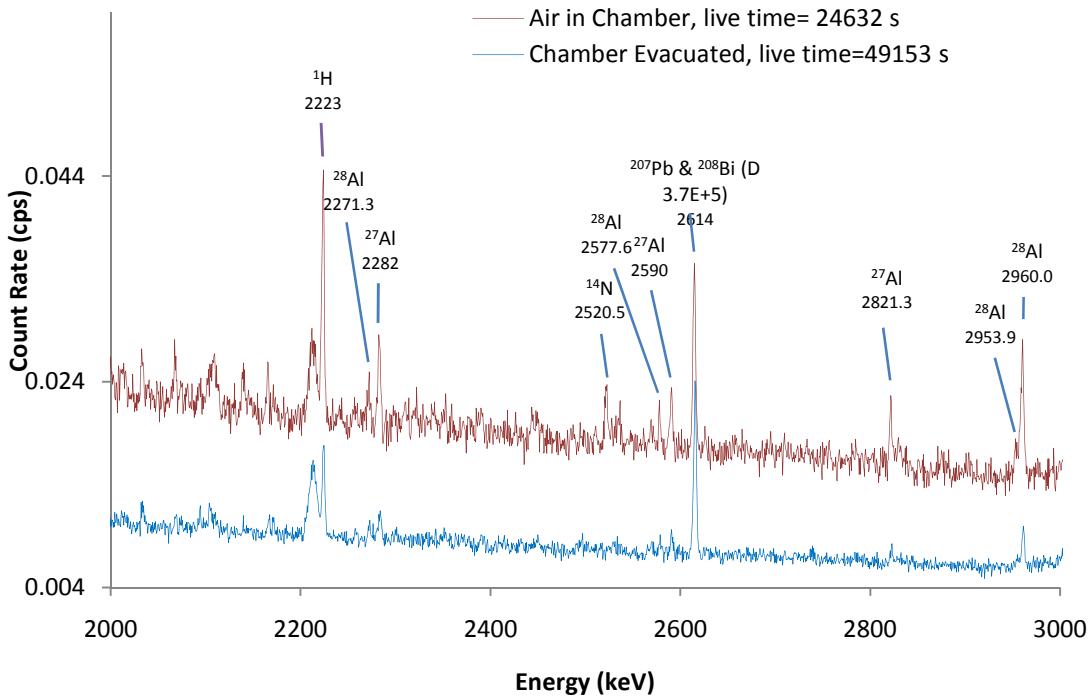


**Figure 7-12: PGNAA Background Spectra before improved detector collimator 2000-3000 keV, (Reactor power 1MW, and Teflon sample pouch in beam)**

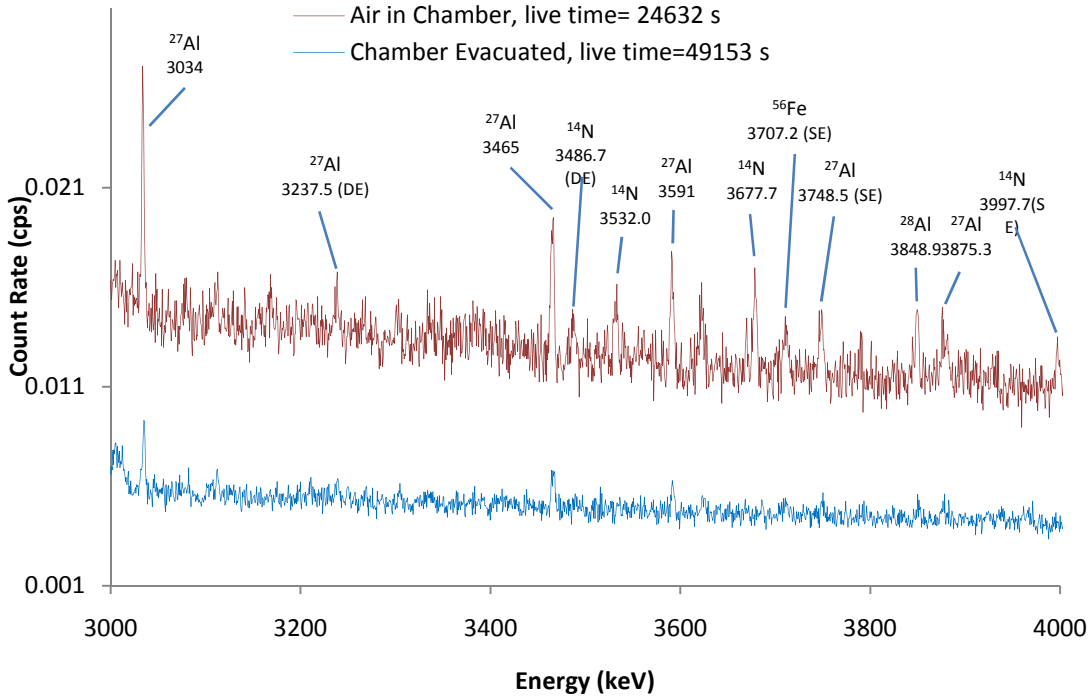


**Figure 7-13: PGNAA Background Spectra before improved detector collimator 3000-4000 keV, (Reactor power 1MW, and Teflon sample pouch in beam)**

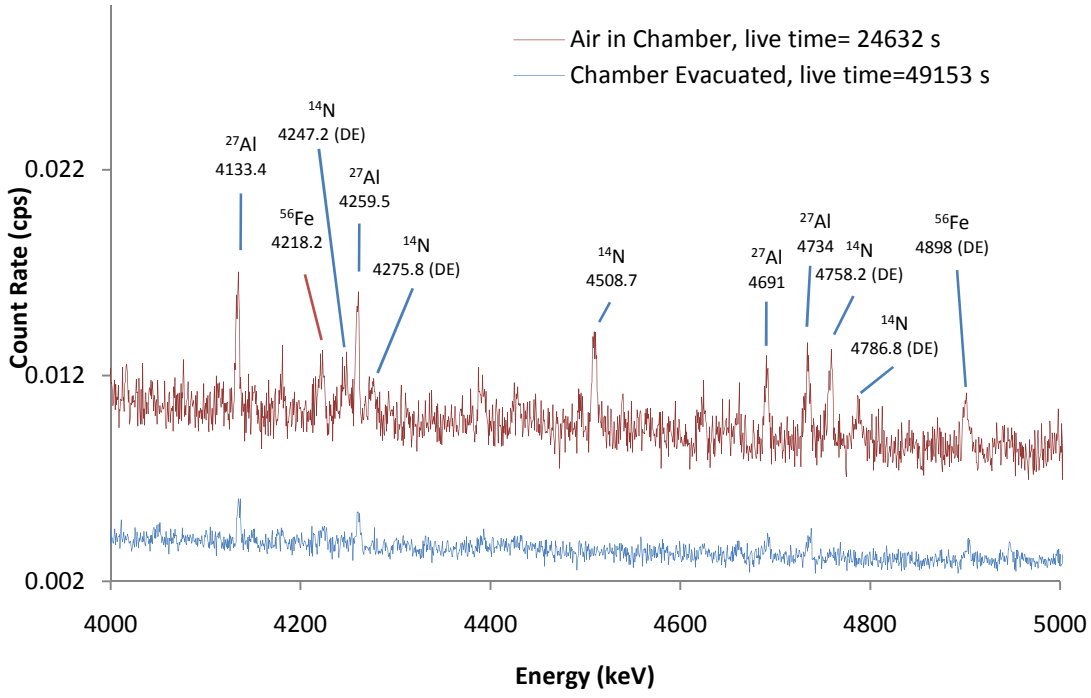


**Figure 7-14: PGNAA Background Spectra before improved detector collimator 4000-5000 keV, (Reactor power 1MW, and Teflon sample pouch in beam)**

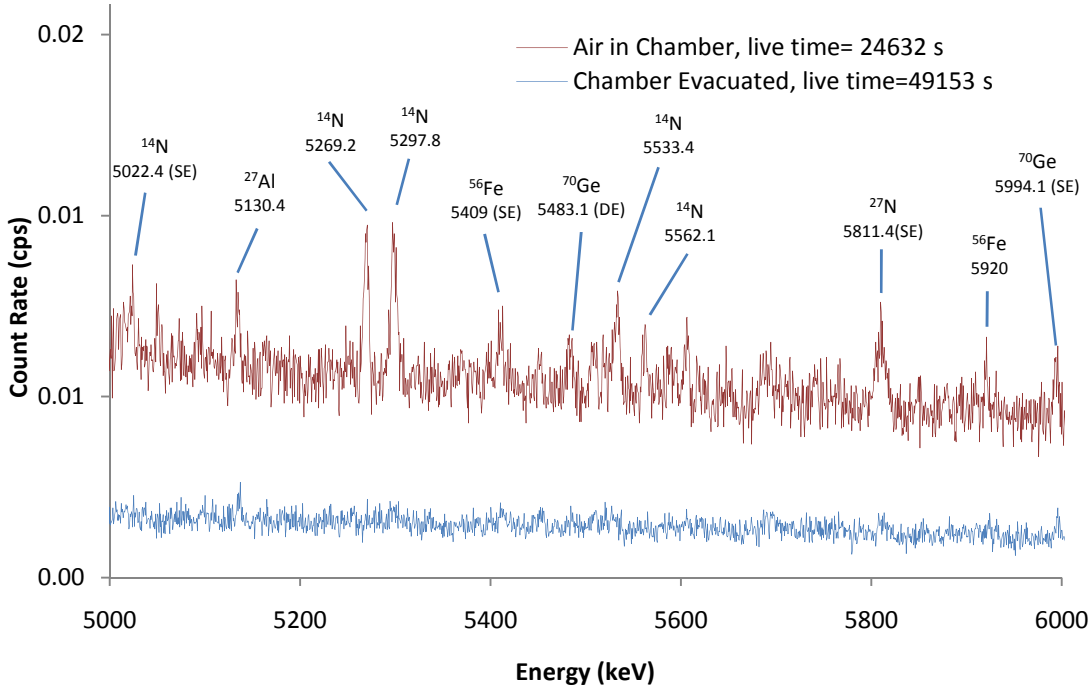


**Figure 7-15: PGNAA Background Spectra before improved detector collimator 5000-6000 keV, (Reactor power 1MW, and Teflon sample pouch in beam)**

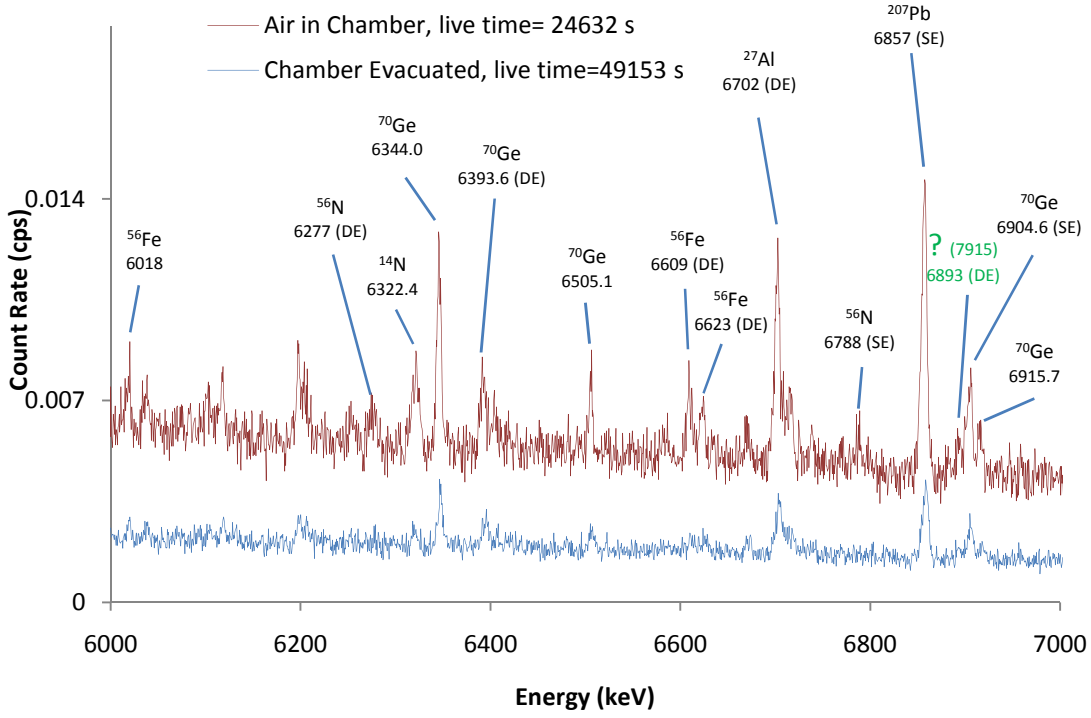


**Figure 7-16: PGNAA Background Spectra before improved detector collimator 6000-7000 keV, (Reactor power 1MW, and Teflon sample pouch in beam)**

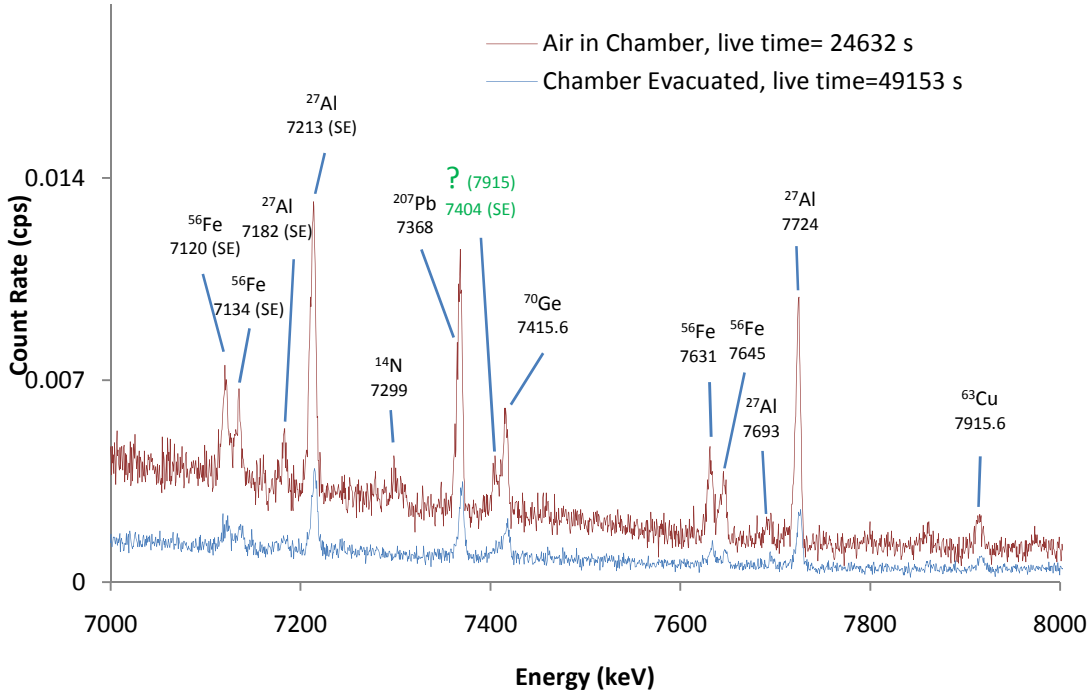


**Figure 7-17: PGNAA Background Spectra before improved detector collimator 7000-8000 keV, (Reactor power 1MW, and Teflon sample pouch in beam)**

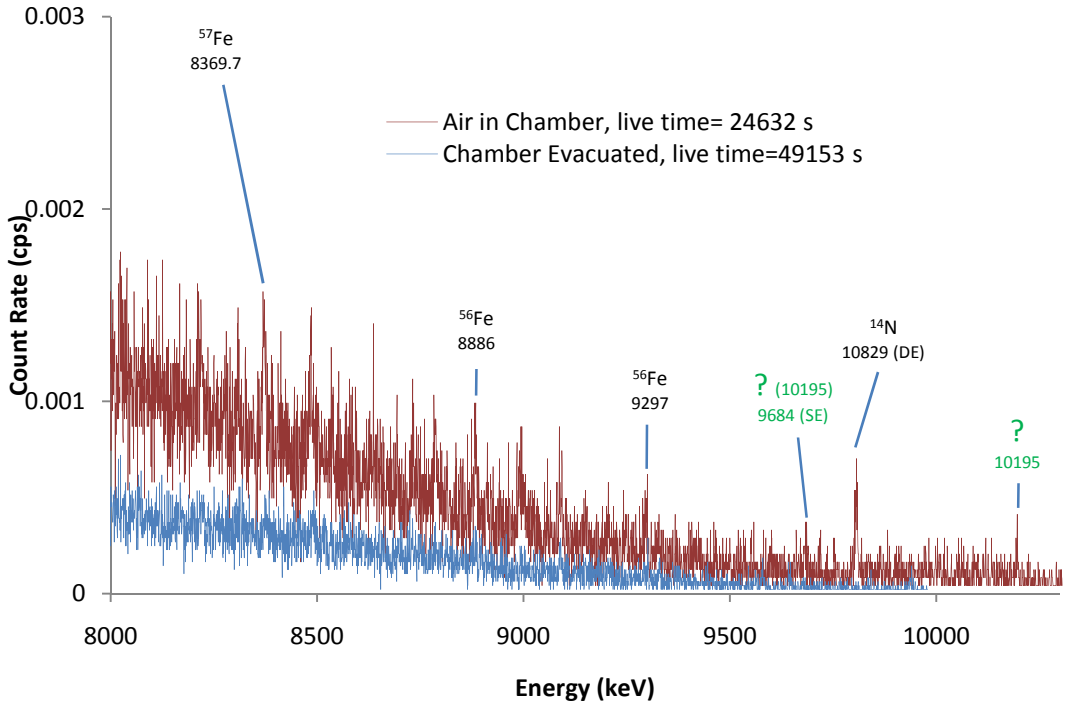


**Figure 7-18: PGNAA Background Spectra before improved detector collimator 8000-10300 keV, (Reactor Power 1MW, and Teflon sample pouch in beam)**

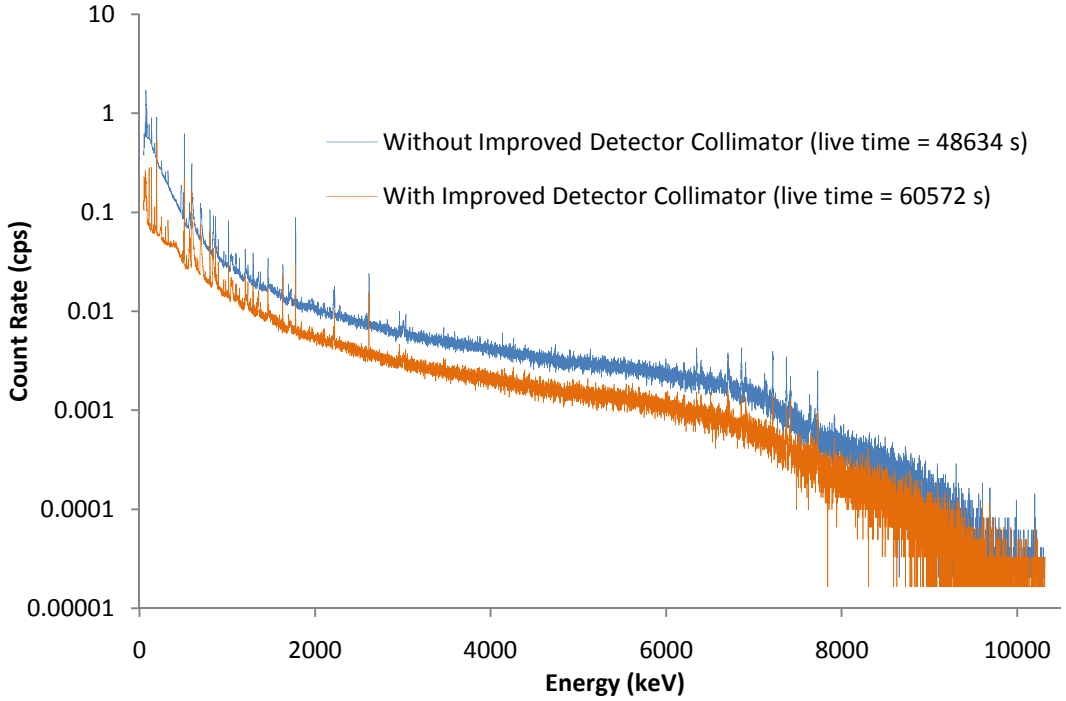


**Figure 7-19: PGNAA Background Spectra after improved detector collimator (Reactor Power 1MW, and Teflon sample pouch in beam)**

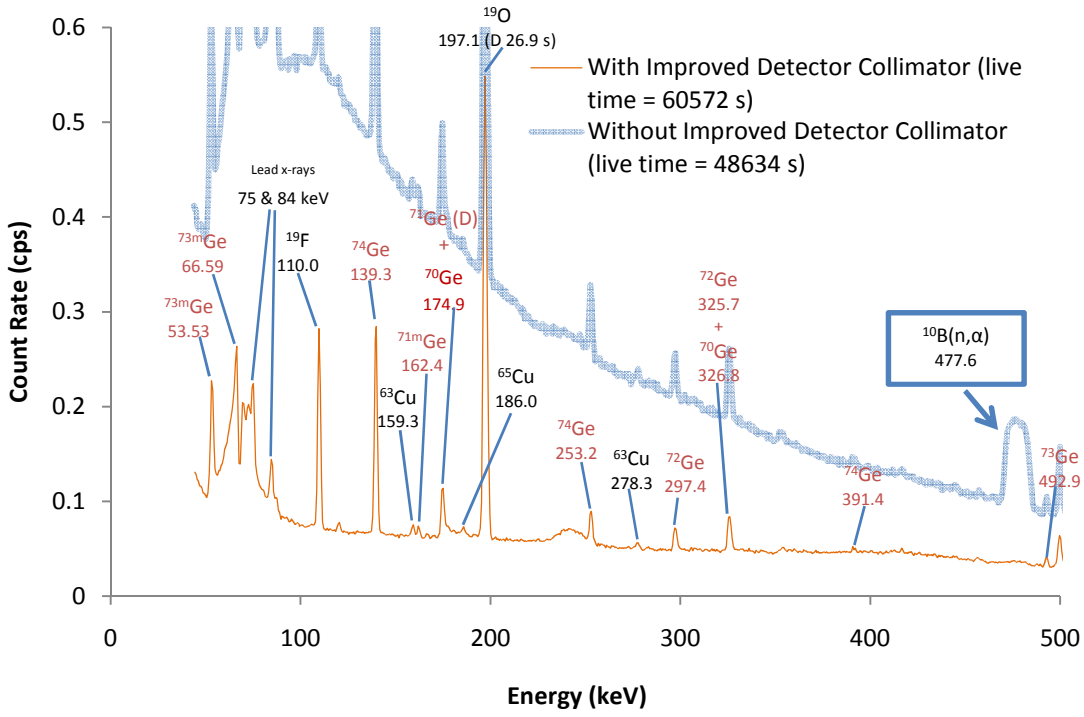


**Figure 7-20: PGNAA Background Spectra after improved detector collimator 0-500 KeV, illustrating the reduction in the Boron 477.6 KeV gamma line. (Reactor Power 1MW, and Teflon sample pouch in beam)**

**Table 7-2: Count Rates for some of the most prominent gamma energies in back ground PGNAA spectra both with and without the sample chamber evacuated**

| | Energy (keV) | Air in Sample Chamber Count Rate(cps) | Sample Chamber Evacuated Count Rate(cps) | Sample Chamber Evacuated, after enhanced Detector collimator Count Rate(cps) |
|---|---|---|---|---|
| O-19 (D 26.9s) | 197.1 | 4.018 ± 0.029 | 2.431 ± 0.016 | 1.839 ± 0.008 |
| Annihilation | 511 | 5.083 ± 0.020 | 2.568 ± 0.011 | 0.936 ± 0.006 |
| F-19 | 110 | 0.264 ± 0.010 | 0.315 ± 0.006 | 0.597 ± 0.007 |
| F | 1633.6 | 0.053 ± 0.006 | 0.066 ± 0.003 | 0.075 ± 0.002 |
| Ge-74 | 139.3 | 2.258 ±0.016 | 0.898 ± 0.008 | 0.670 ± 0.007 |
| Ge | 1204.2 | 0.162 ± 0.006 | 0.069 ± 0.003 | 0.037 ± 0.003 |
| Ge Triangle | 595.9 | 4.512 ± 0.064 | 3.038 ± 0.036 | 1.383 ± 0.025 |
| Ge Triangle | 693 | 2.187 ± 0.060 | 1.87 ± 0.032 | 0.935 ± 0.018 |
| Ge Triangle | 1039.5 | 0.380 ± 0.044 | 0.389 ± 0.022 | 0.103 ± 0.011 |
| B-10 | 477.6 | 7.748 ± 0.039 | 1.775 ± 0.020 | 0.047 ± 0.008 |
| Al-27 | 1014.4 | 0.255 ± 0.009 | 0.233 ± 0.005 | 0.065 ± 0.003 |
| Al-27 D | 1778.9 | 1.243 ± 0.010 | 0.366 ± 0.004 | 0.111 ± 0.002 |
| Al-27 | 3034 | 0.061 ± 0.007 | 0.024 ± 0.003 | 0.007 ± 0.002 |
| Al-27 | 7213 | 0.112 ± 0.005 | 0.033 ± 0.003 | 0.007 ± 0.001 |
| H | 2223 | 0.053 ± 0.006 | 0.031 ± 0.003 | 0.022 ± 0.002 |
| 207-Pb | 803.2 | 0.183 ± 0.005 | 0.222 ± 0.006 | 0.155 ± 0.004 |
| 207-Pb | 7368 | 0.090 ± 0.005 | 0.025 ± 0.002 | 0.008 ± 0.001 |
| Pb &Bi | 2614 | 0.105 ± 0.009 | 0.102 ± 0.004 | 0.065 ± 0.002 |
| Fe | 7631 & 7645 | 0.042 ± 0.006 | 0.010 ± 0.002 | Nd* |
| Fe (SE) | 7120 &7134 | 0.052 ± 0.008 | 0.012 ± 0.004 | Nd* |
| N-14 | 1678.3 | 0.007 ± 0.003 | Nd* | Nd* |
| N-14 | 1884.8 | 0.048 ± 0.005 | Nd* | Nd* |
| N-14 | 2520.5 | 0.023 ± 0.004 | Nd* | Nd* |
| N-14 | 3677.7 | 0.023 ± 0.004 | Nd* | Nd* |
| N-14 | 4508.7 | 0.035 ± 0.005 | Nd* | Nd* |
| N (DE) | 9807 | 0.005 ± 0.001 | Nd* | Nd* |

* Unable to distinguish from background

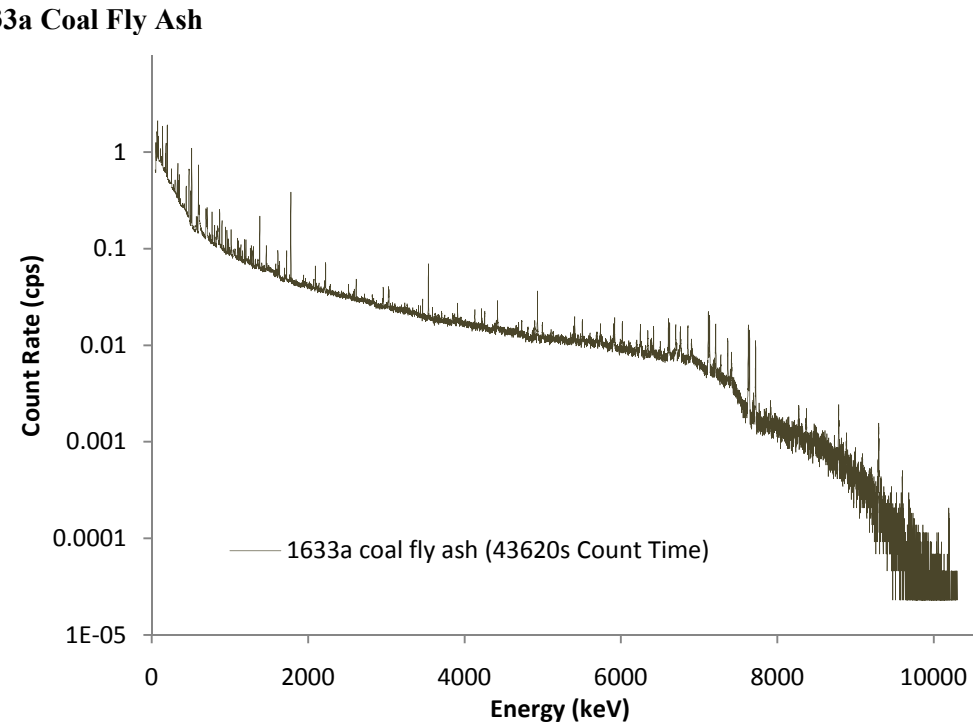


**Figure 7-21: PGNAA 1633a Coal Fly Ash Spectrum before improved detector collimator, (Reactor Power 1MW, and sample contained in Teflon sample pouch)**

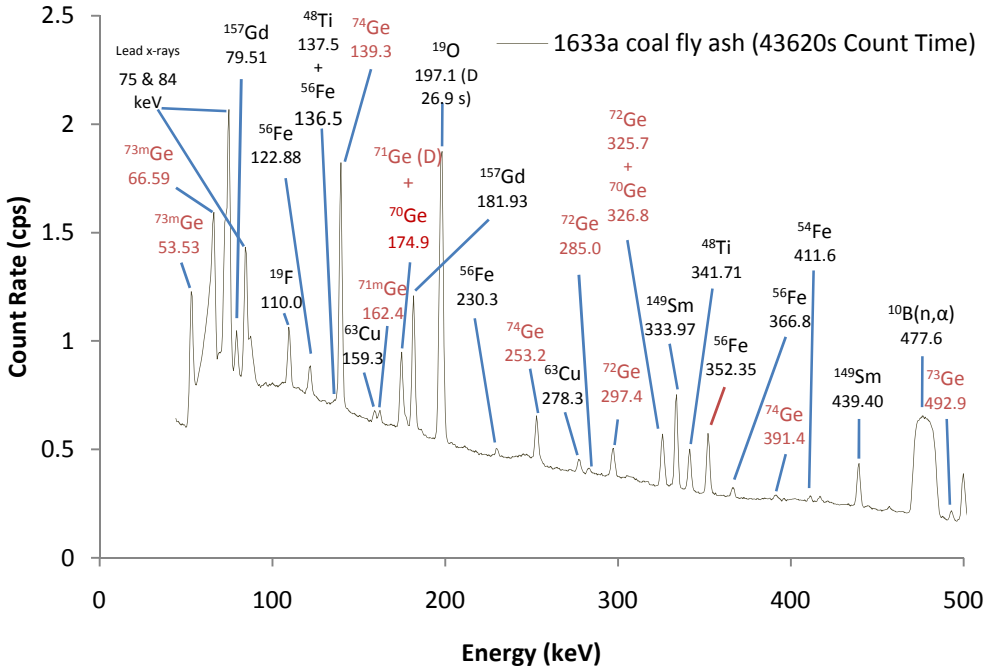


**Figure 7-22: PGNAA 1633a Coal Fly Ash Spectrum before improved detector collimator 0-500 keV, (Reactor Power 1MW, and sample contained in Teflon sample pouch)**

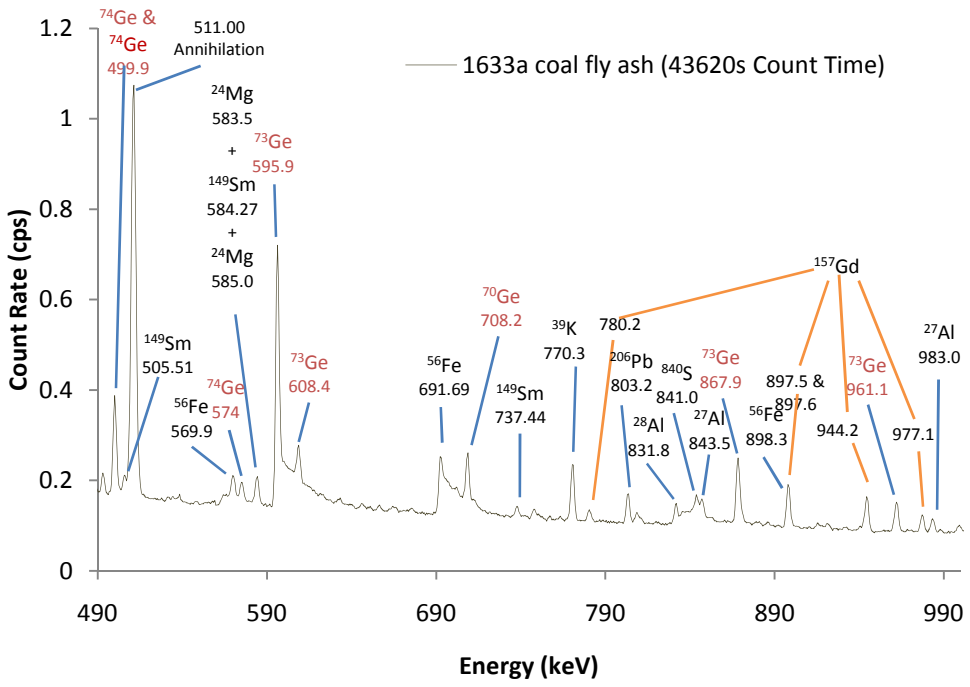


**Figure 7-23: PGNAA 1633a Coal Fly Ash Spectrum before improved detector collimator500-1000 keV, (Reactor Power 1MW, and sample contained in Teflon sample pouch)**

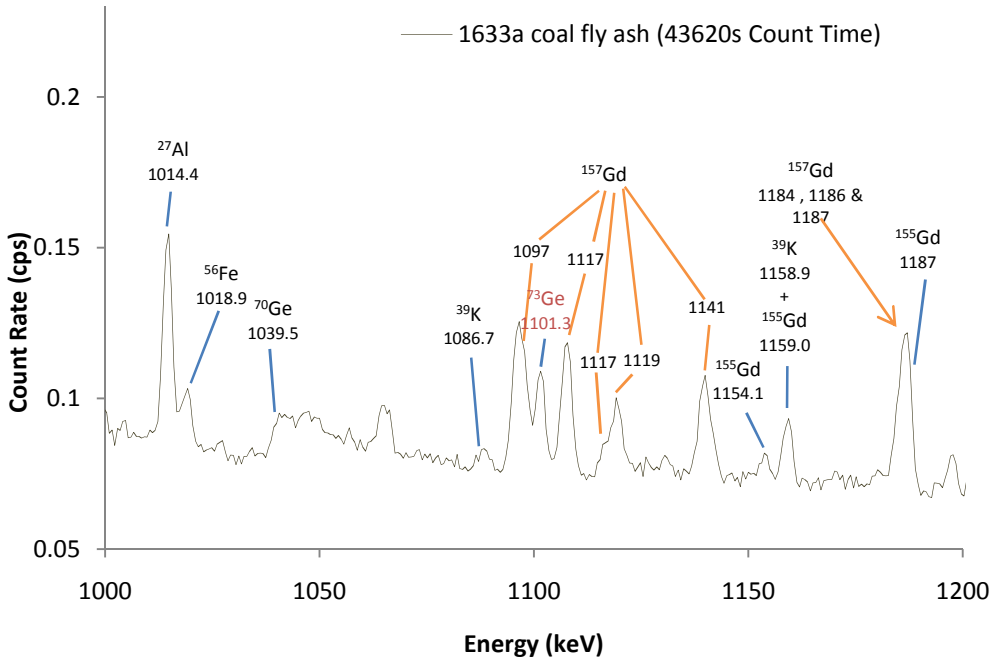


**Figure 7-24: PGNAA 1633a Coal Fly Ash Spectrum before improved detector collimator 1000-1200 keV, (Reactor Power 1MW, and sample contained in Teflon sample pouch)**

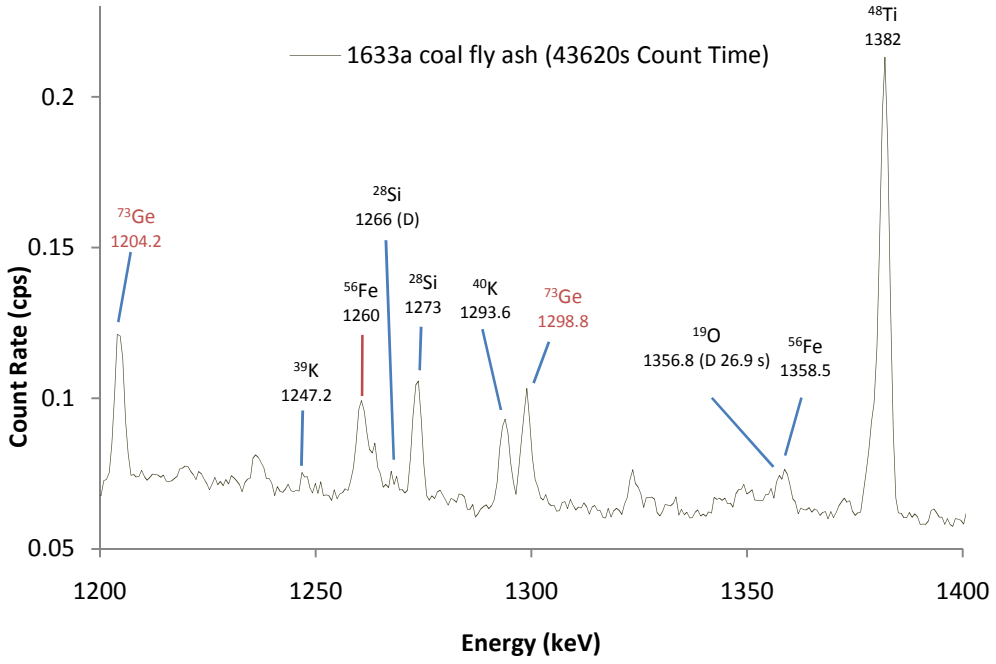


**Figure 7-25: PGNAA 1633a Coal Fly Ash Spectrum before improved detector collimator 1200-1400 keV, (Reactor Power 1MW, and sample contained in Teflon sample pouch)**

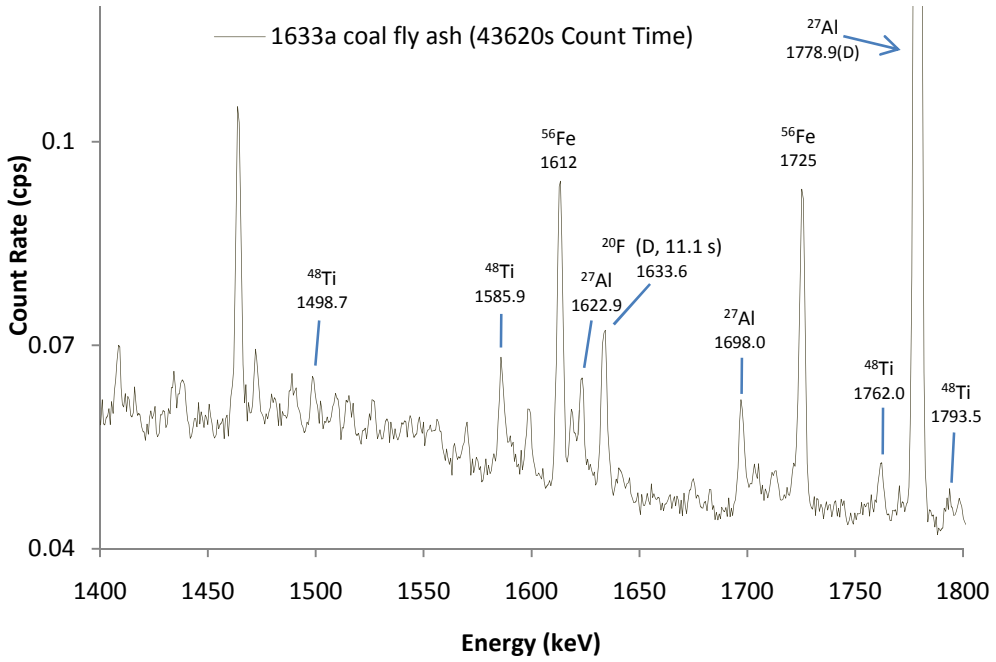


**Figure 7-26: PGNAA 1633a Coal Fly Ash Spectrum before improved detector collimator 1400-1800 keV, (Reactor Power 1MW, and sample contained in Teflon sample pouch)**

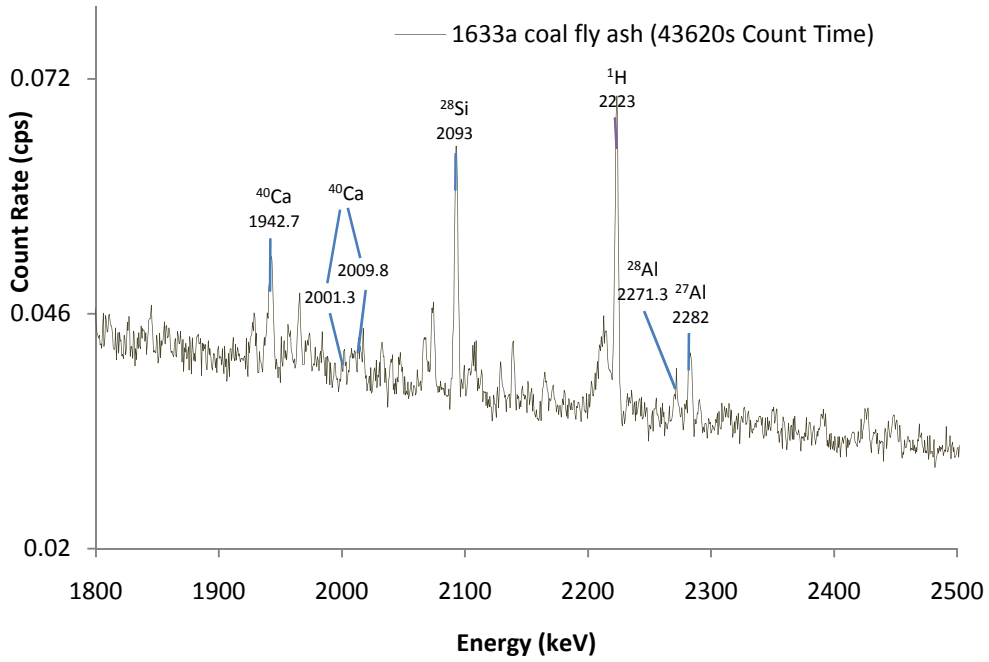


**Figure 7-27: PGNAA 1633a Coal Fly Ash Spectrum before improved detector collimator 1800-2500 keV, (Reactor Power 1MW, and sample contained in Teflon sample pouch)**

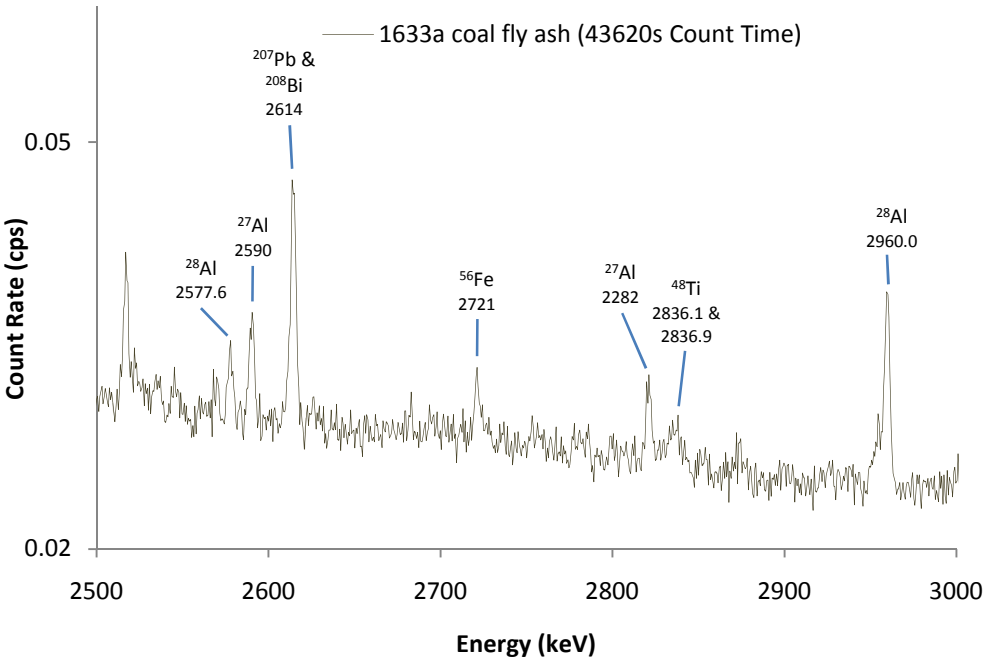


**Figure 7-28: PGNAA 1633a Coal Fly Ash Spectrum before improved detector collimator 2500-3000 keV, (Reactor Power 1MW, and sample contained in Teflon sample pouch)**

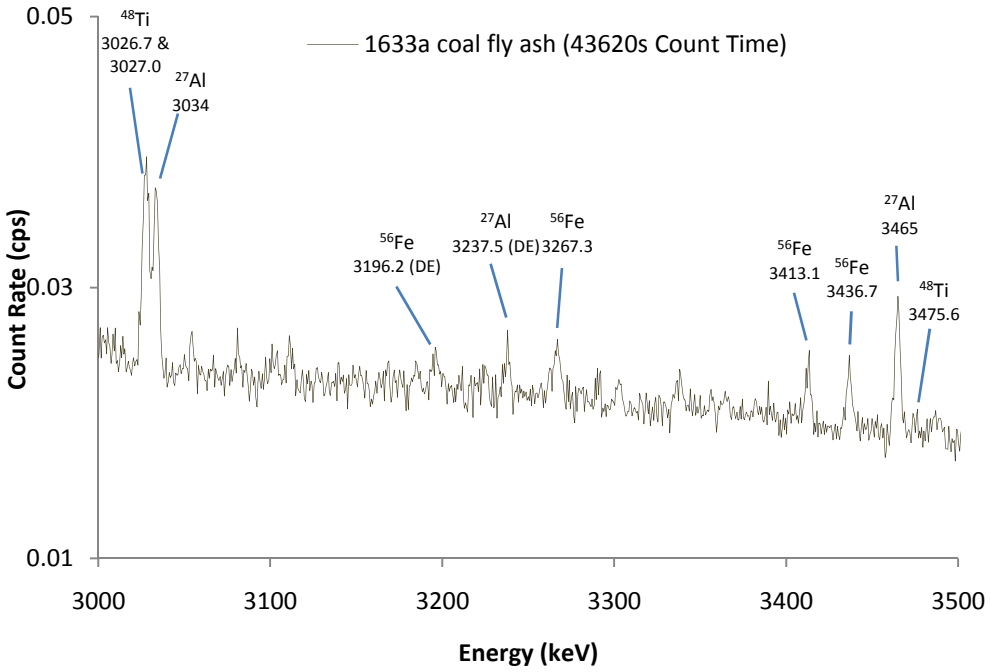


**Figure 7-29: PGNAA 1633a Coal Fly Ash Spectrum before improved detector collimator 3000-3500 keV, (Reactor Power 1MW, and sample contained in Teflon sample pouch)**

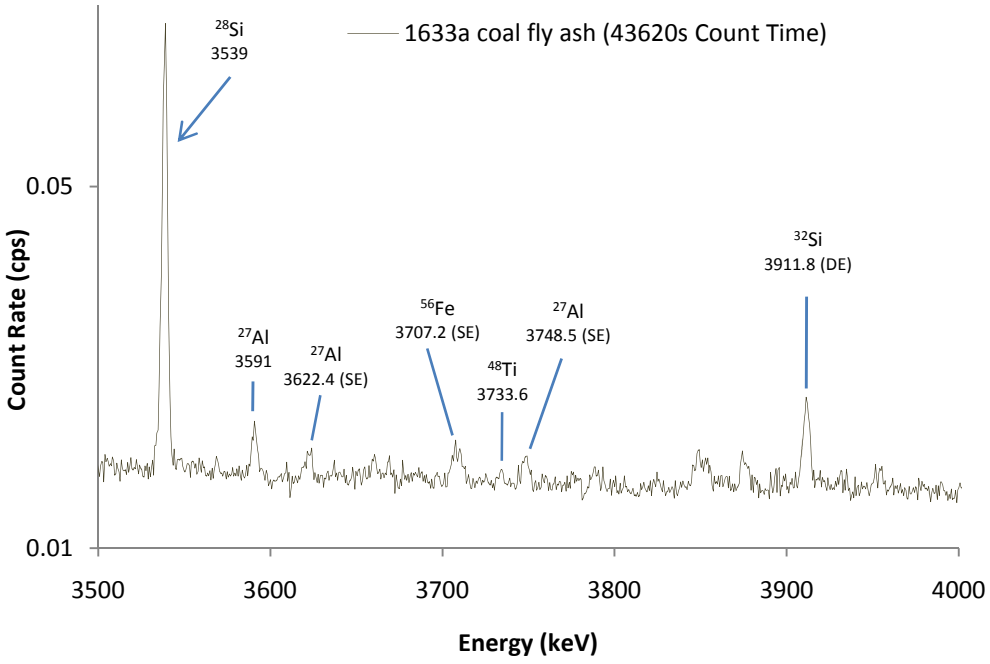


**Figure 7-30: PGNAA 1633a Coal Fly Ash Spectrum before improved detector collimator 3500-4000 keV, (Reactor Power 1MW, and sample contained in Teflon sample pouch)**

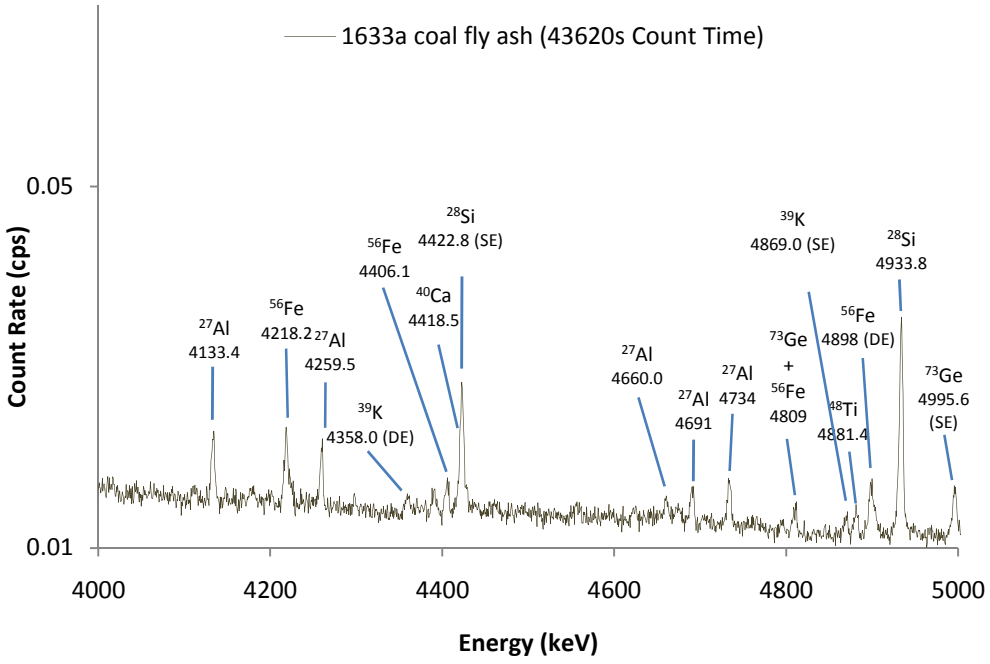


**Figure 7-31: PGNAA 1633a Coal Fly Ash Spectrum before improved detector collimator 4000-5000 keV, (Reactor Power 1MW, and sample contained Teflon in sample pouch)**

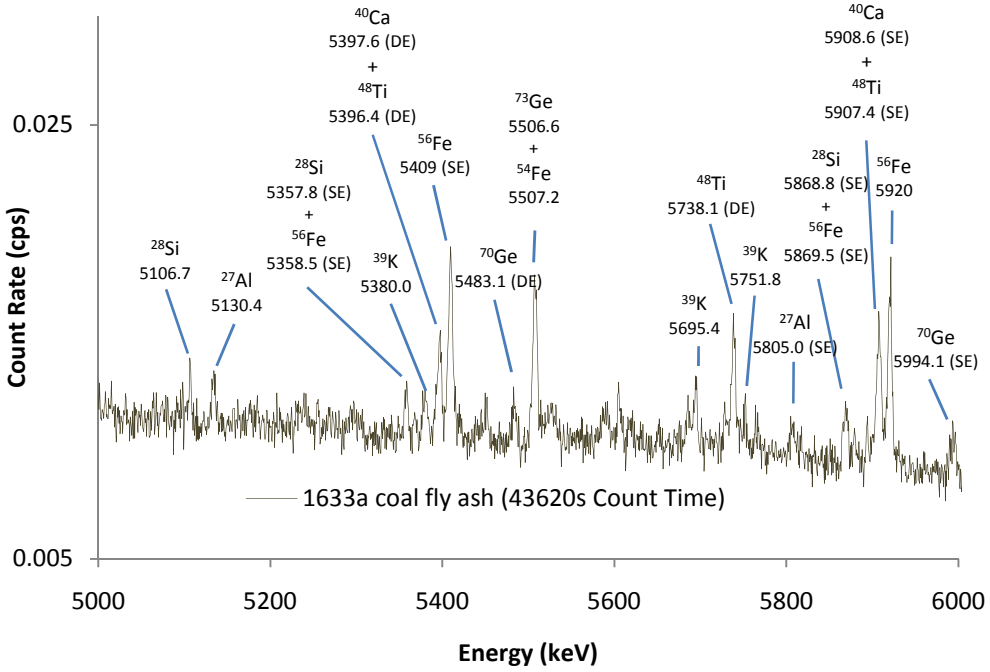


**Figure 7-32: PGNAA 1633a Coal Fly Ash Spectrum before improved detector collimator 5000-6000 keV, (Reactor Power 1MW, and sample contained in Teflon sample pouch)**

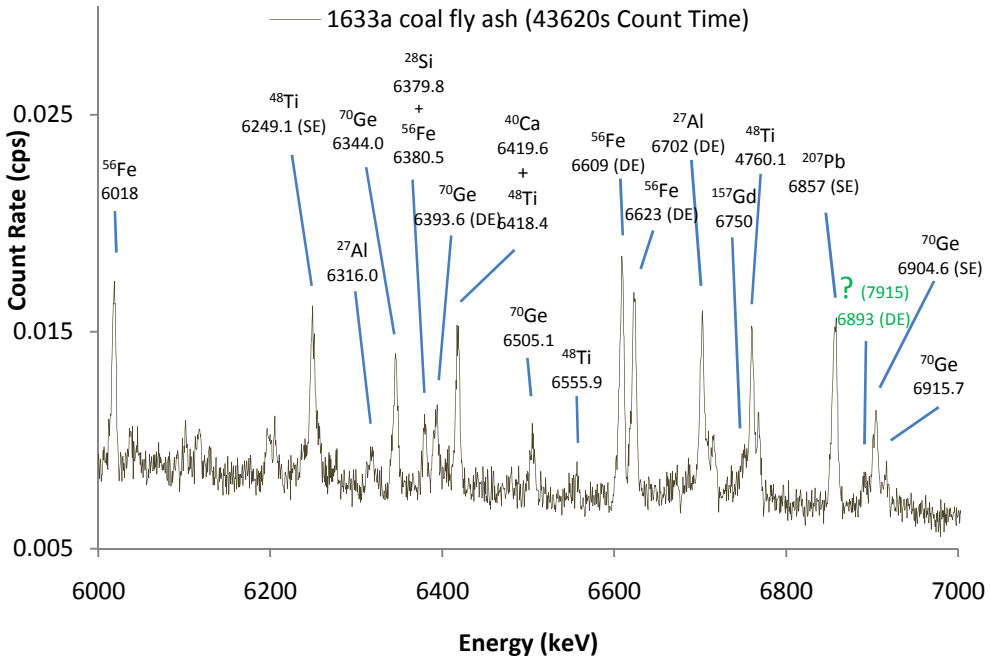


**Figure 7-33: PGNAA 1633a Coal Fly Ash Spectrum before improved detector collimator 6000-7000 keV, (Reactor Power 1MW, and sample contained in Teflon sample pouch)**

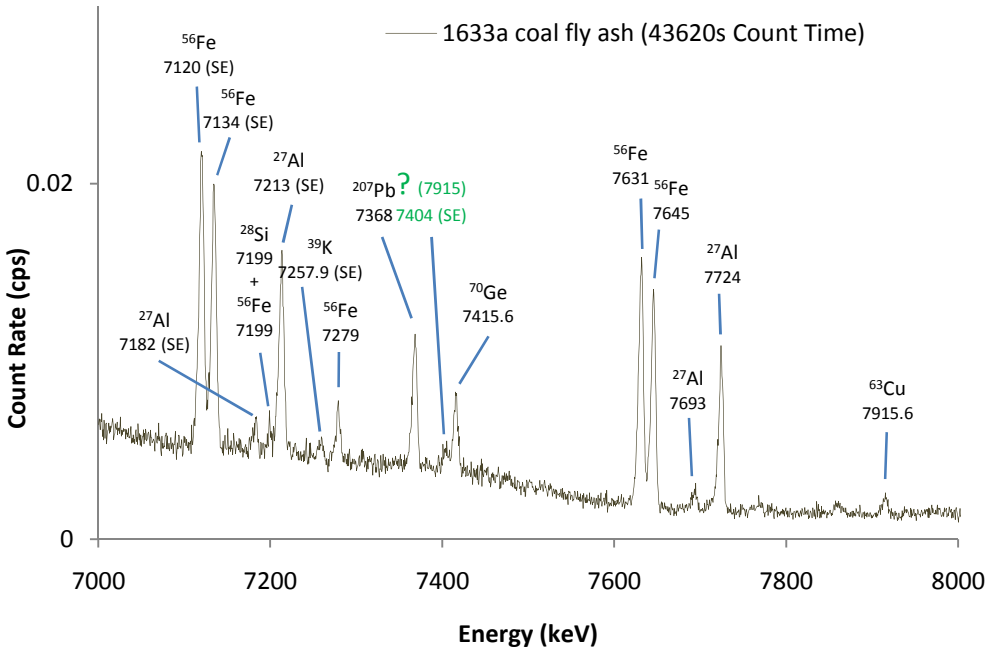


**Figure 7-34: PGNAA 1633a Coal Fly Ash Spectrum before improved detector collimator 7000-8000 keV, (Reactor Power 1MW, and sample contained in Teflon sample pouch)**

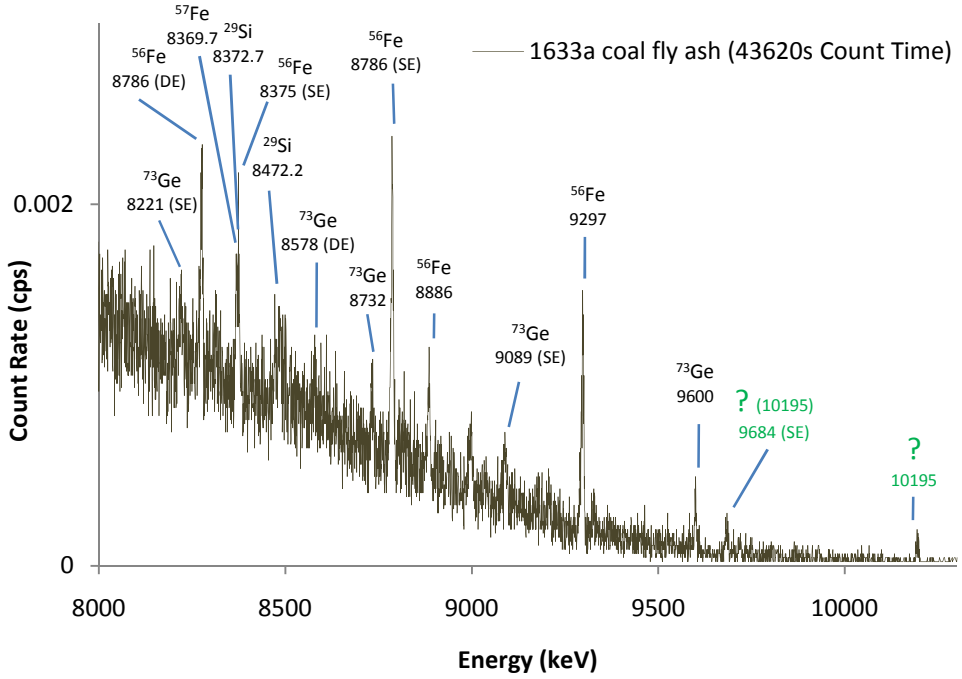


**Figure 7-35: PGNAA 1633a Coal Fly Ash Spectrum before improved detector collimator 8000-10500 keV, (Reactor Power 1MW, and sample contained in Teflon sample pouch)**

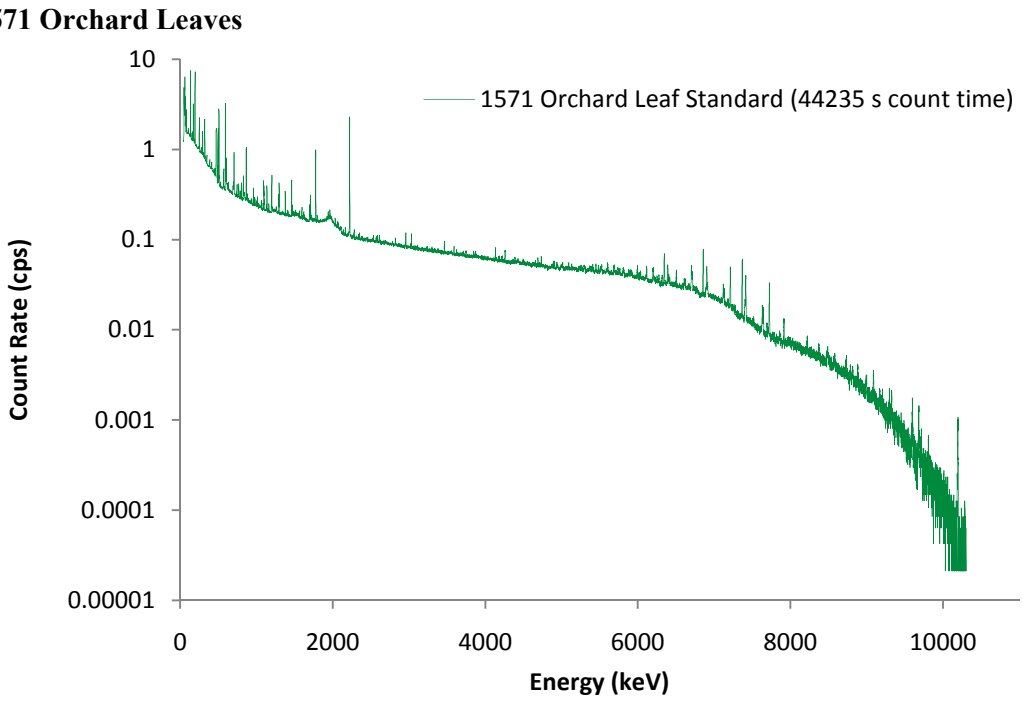


**Figure 7-36: PGNAA 1571 Orchard Leaf Spectrum before improved detector collimator, (Reactor Power 1MW, and sample contained in Teflon sample pouch)**

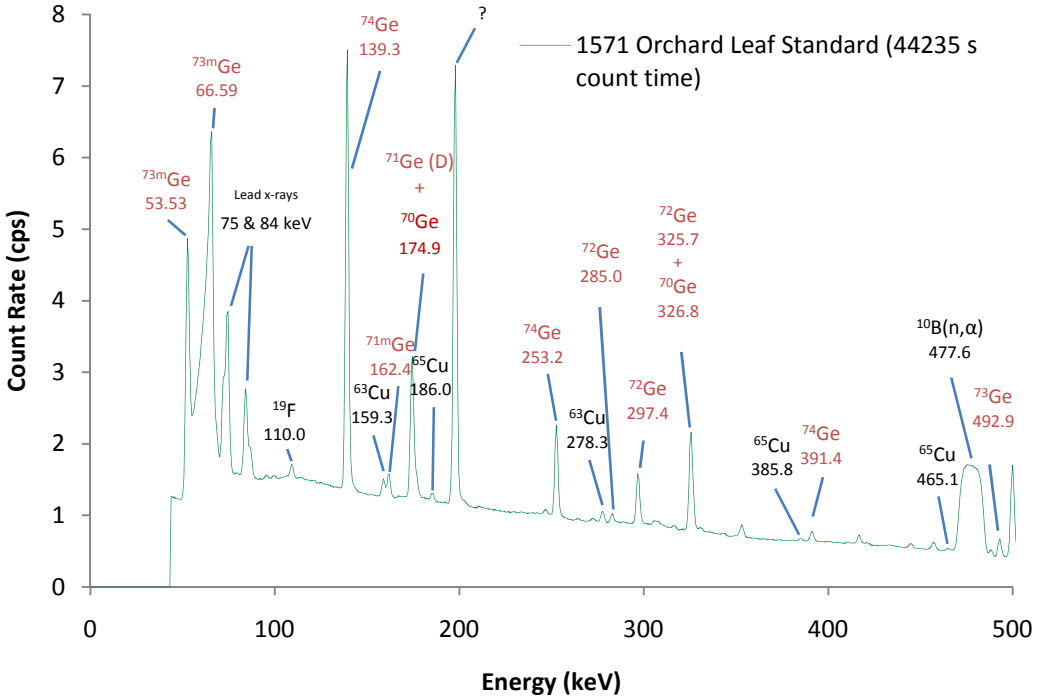


**Figure 7-37: PGNAA 1571 Orchard Leaf Spectrum before improved detector collimator 0-500 keV, (Reactor Power 1MW, and sample contained in Teflon sample pouch)**

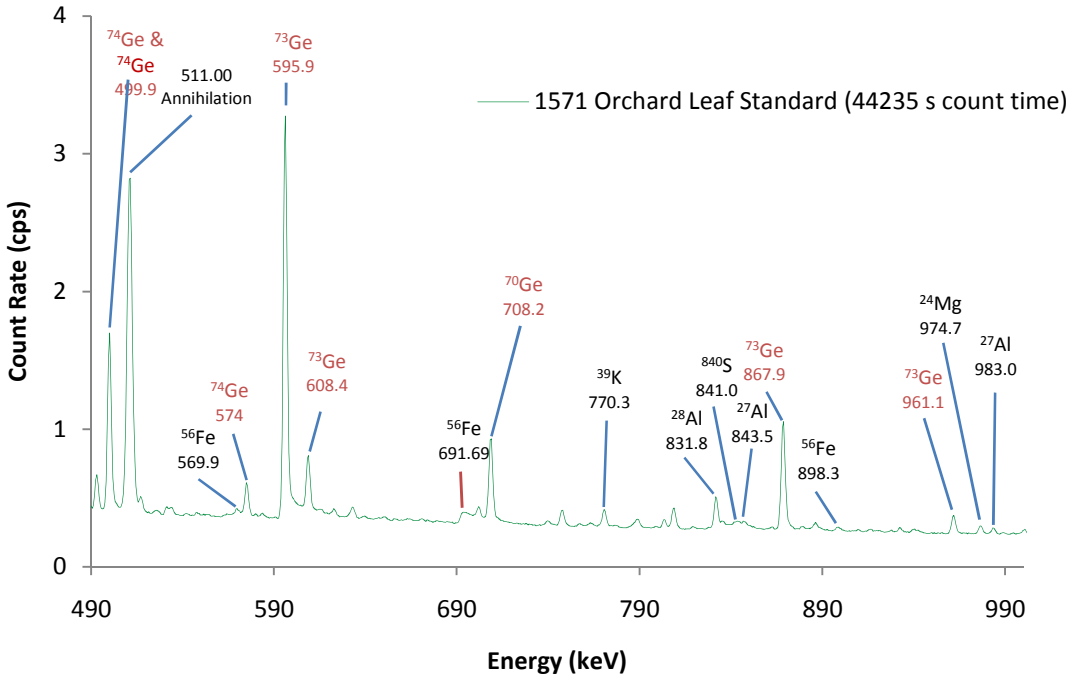


**Figure 7-38: PGNAA 1571 Orchard Leaf Spectrum before improved detector collimator 490-990 keV, (Reactor Power 1MW, and sample contained in Teflon sample pouch)**

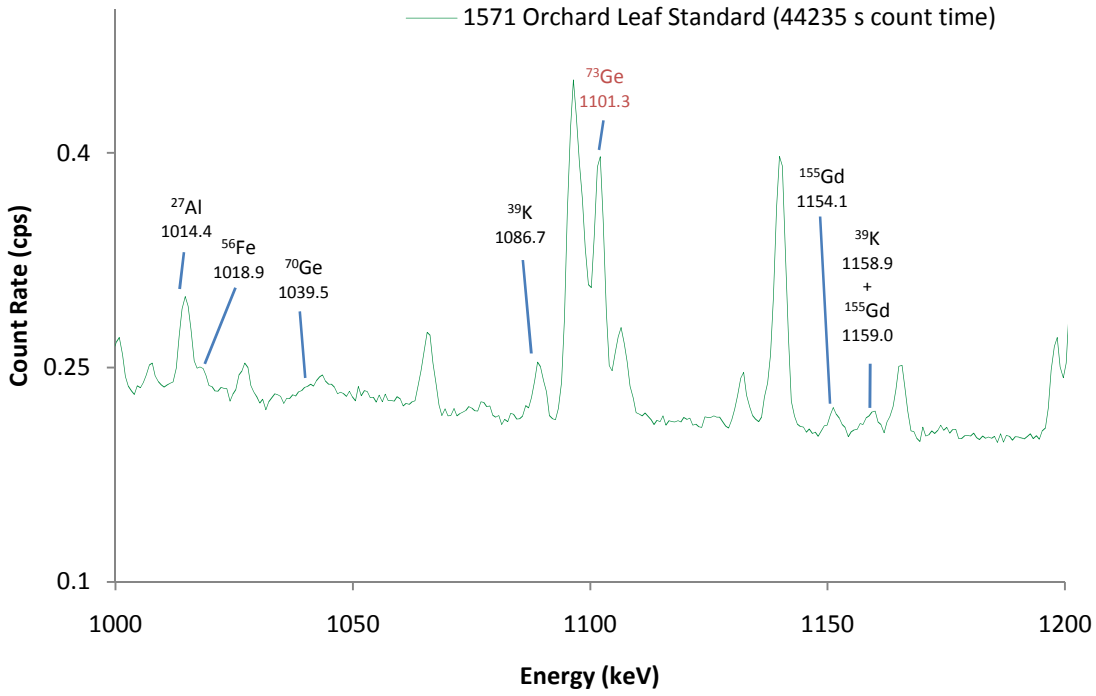


**Figure 7-39: PGNAA 1571 Orchard Leaf Spectrum before improved detector collimator 1000-1200 keV, (Reactor Power 1MW, and sample contained in Teflon sample pouch)**

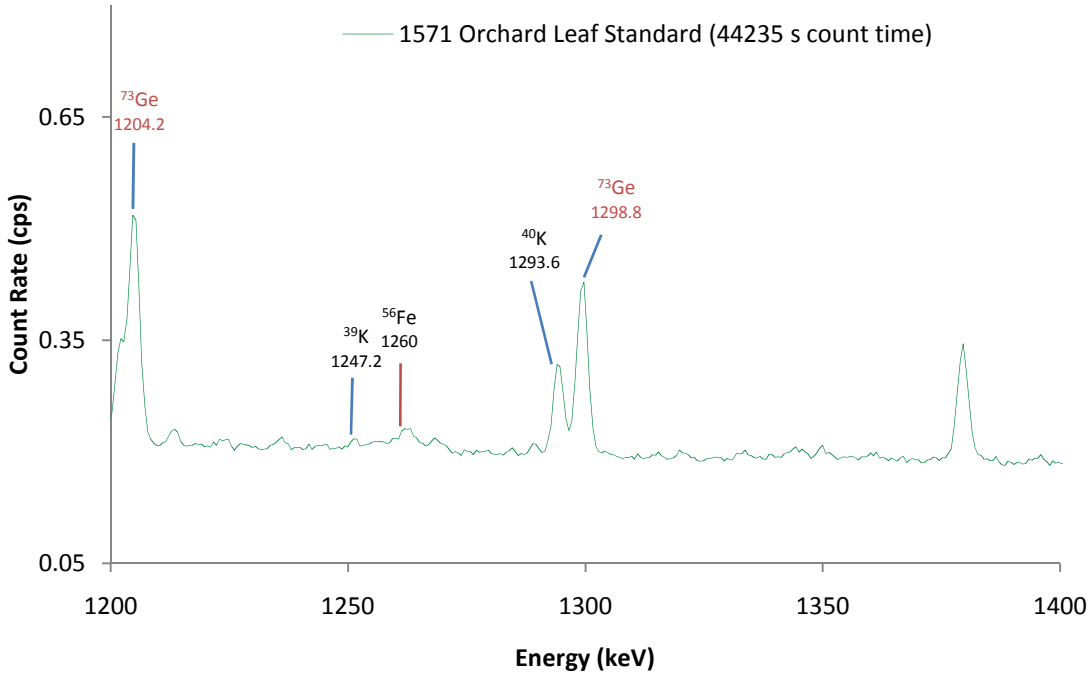


**Figure 7-40: PGNAA 1571 Orchard Leaf Spectrum before improved detector collimator 1200-1400 keV, (Reactor Power 1MW, and sample contained in Teflon sample pouch)**

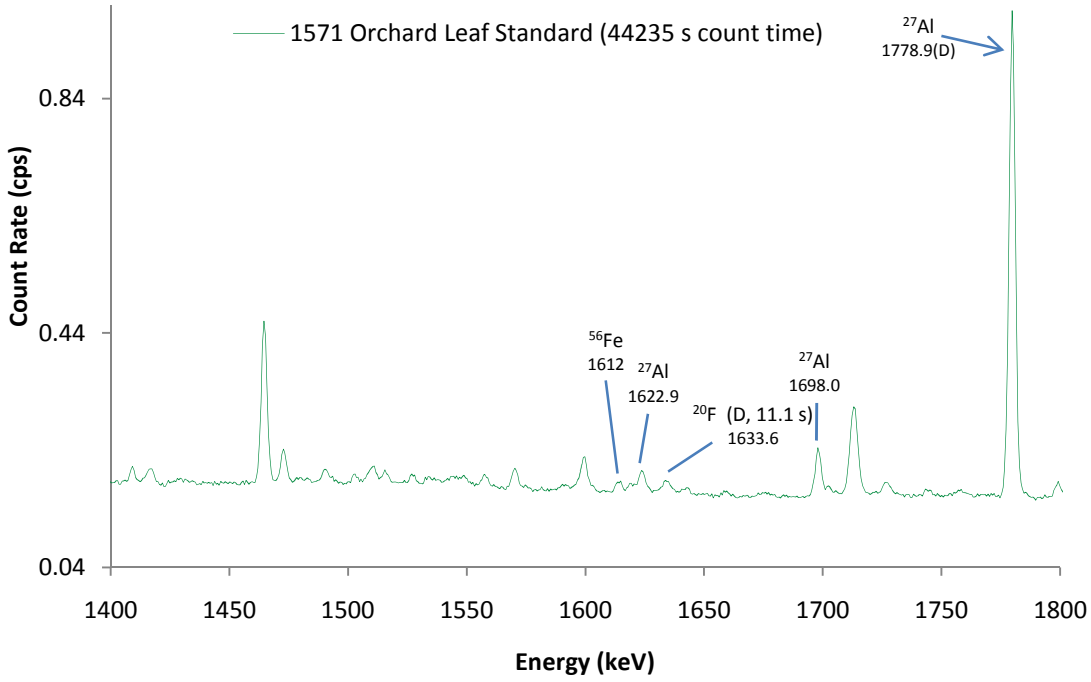


**Figure 7-41: PGNAA 1571 Orchard Leaf Spectrum before improved detector collimator 1400-1800 keV, (Reactor Power 1MW, and sample contained in Teflon sample pouch)**

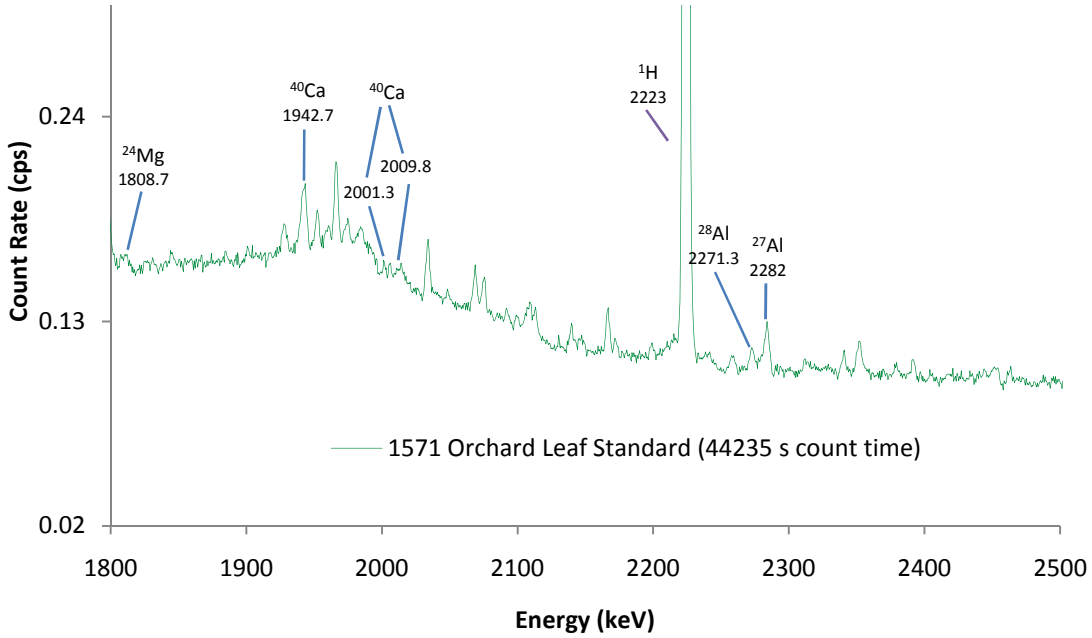


**Figure 7-42: PGNAA 1571 Orchard Leaf Spectrum before improved detector collimator 1800-2500 keV, (Reactor Power 1MW, and sample contained in Teflon sample pouch)**

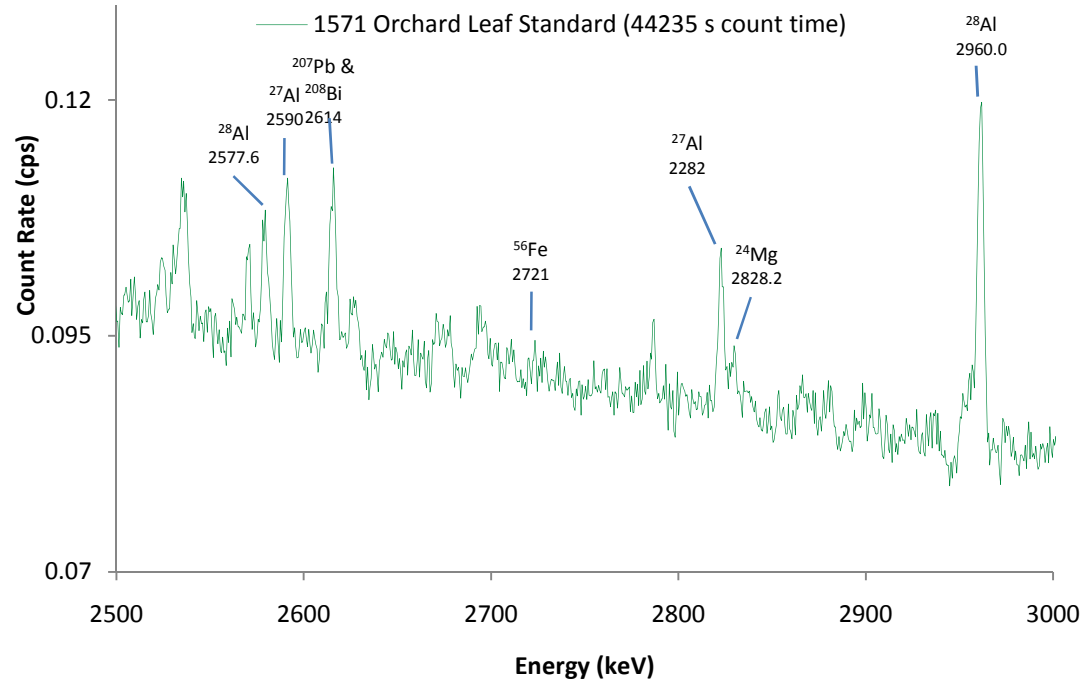


**Figure 7-43: PGNAA 1571 Orchard Leaf Spectrum before improved detector collimator 2500-3000 keV, (Reactor Power 1MW, and sample contained in Teflon sample pouch)**

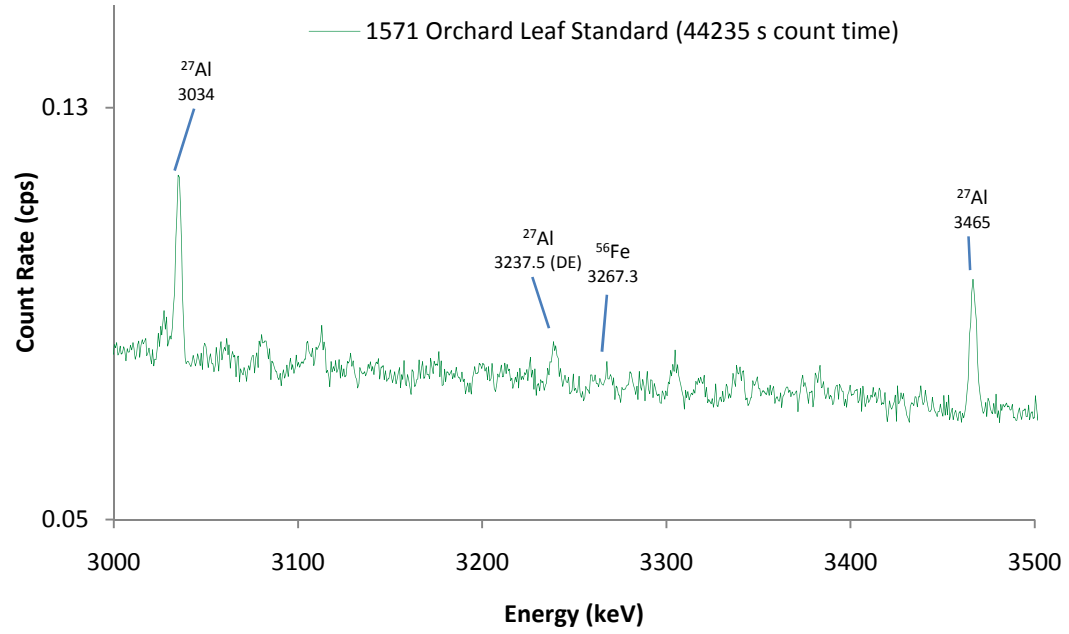


**Figure 7-44: PGNAA 1571 Orchard Leaf Spectrum before improved detector collimator 3000-3500 keV, (Reactor Power 1MW, and sample contained in Teflon sample pouch)**

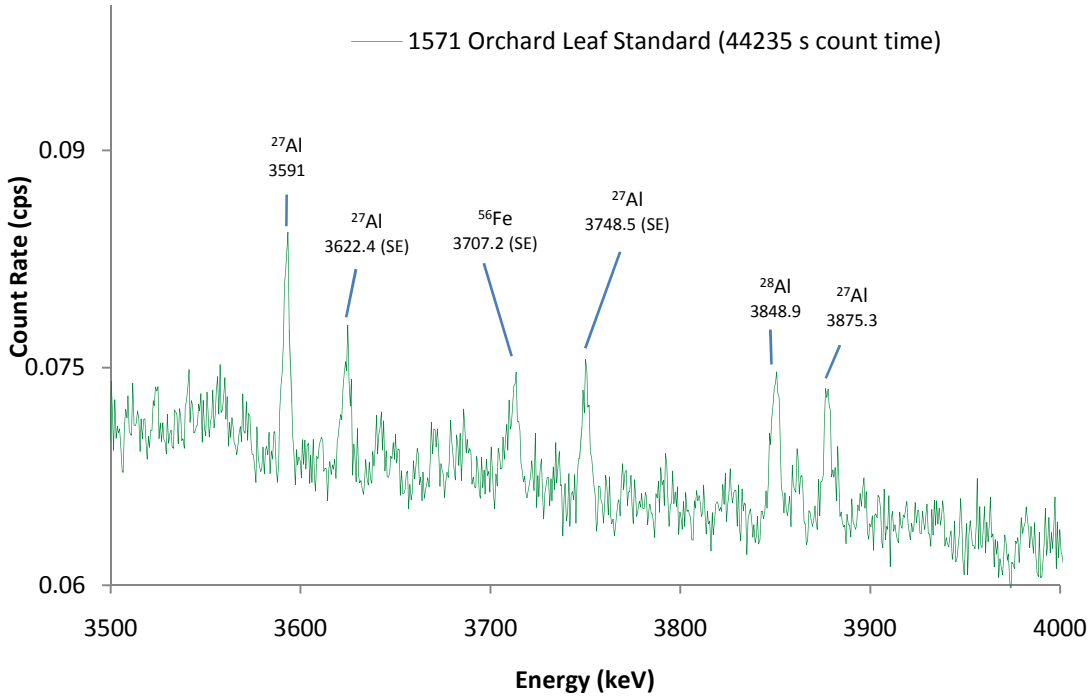


**Figure 7-45: PGNAA 1571 Orchard Leaf Spectrum before improved detector collimator 3500-4000 keV, (Reactor Power 1MW, and sample contained in Teflon sample pouch)**

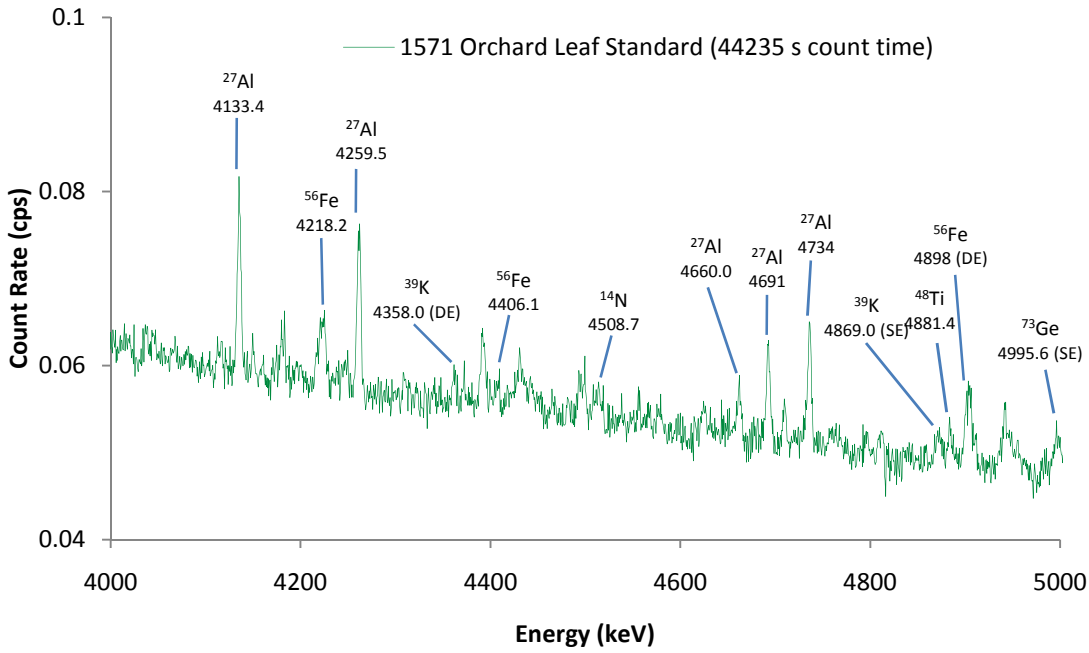


**Figure 7-46: PGNAA 1571 Orchard Leaf Spectrum before improved detector collimator 8000-5000 keV, (Reactor Power 1MW, and sample contained in Teflon sample pouch)**

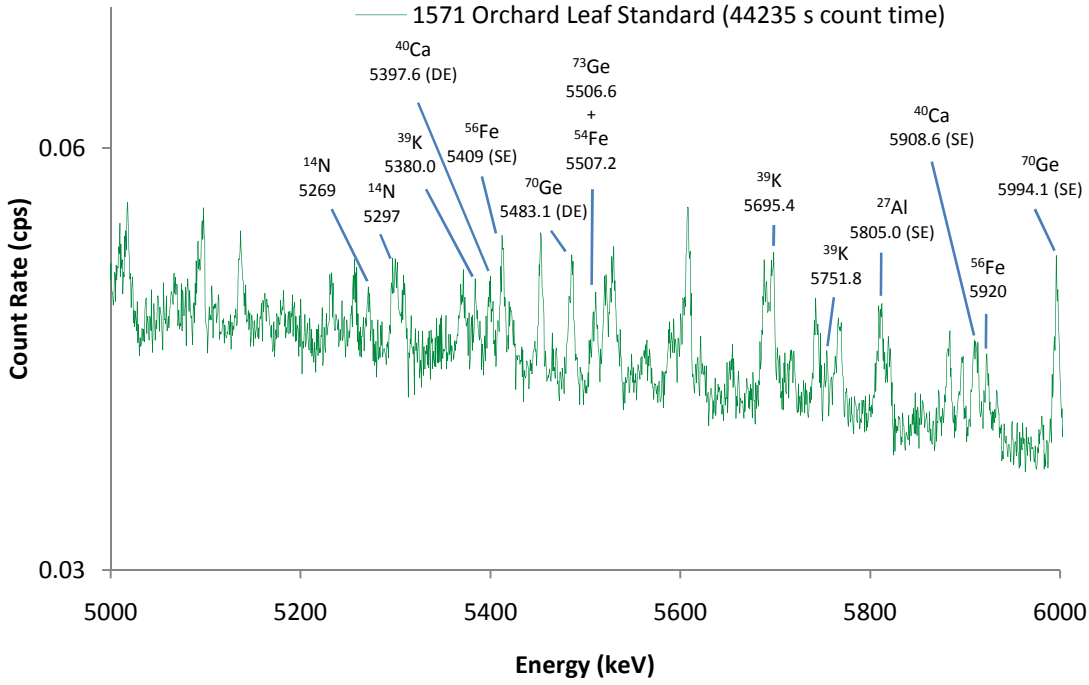


**Figure 7-47: PGNAA 1571 Orchard Leaf Spectrum before improved detector collimator 5000-6000 keV, (Reactor Power 1MW, and sample contained in Teflon sample pouch)**

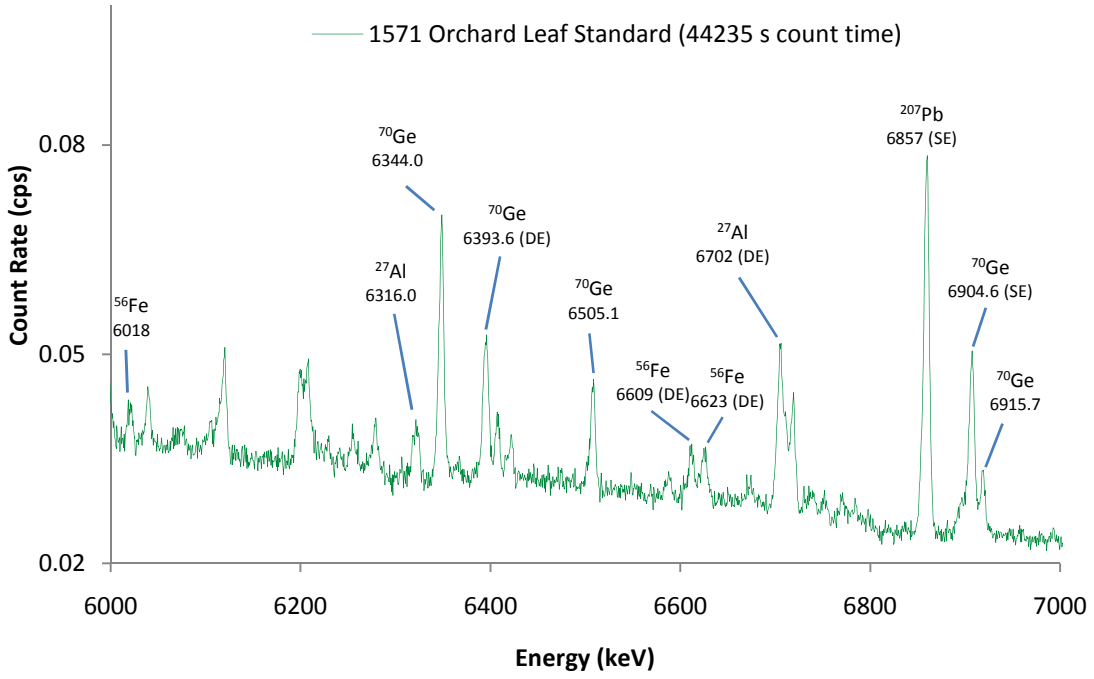


**Figure 7-48: PGNAA 1571 Orchard Leaf Spectrum before improved detector collimator 6000-7000 keV, (Reactor Power 1MW, and sample contained in Teflon sample pouch)**

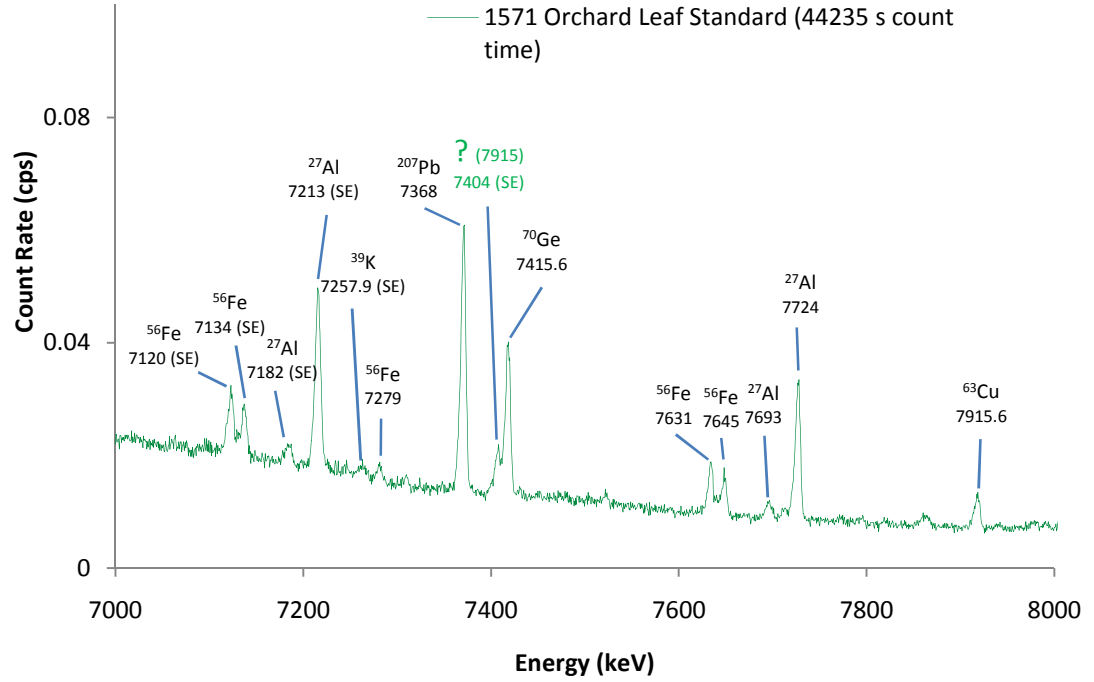


**Figure 7-49: PGNAA 1571 Orchard Leaf Spectrum before improved detector collimator 7000-8000 keV, (Reactor Power 1MW, and sample contained in Teflon sample pouch)**

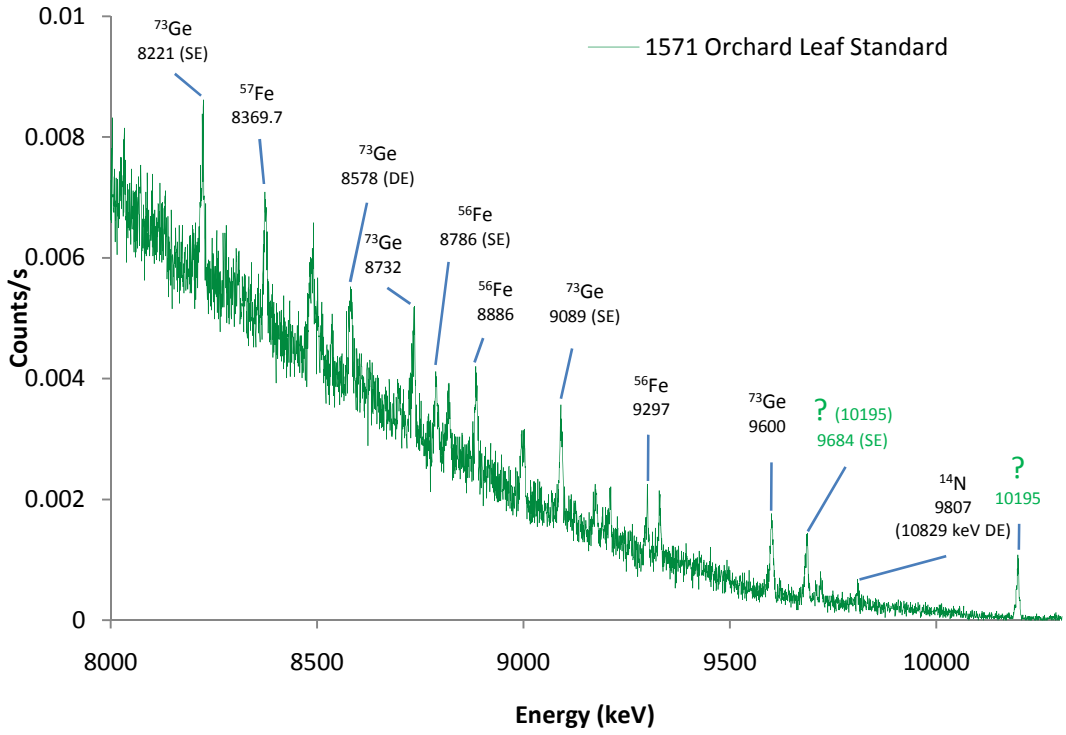


**Figure 7-50: PGNAA 1571 Orchard Leaf Spectrum before improved detector collimator 8000-10500 keV, (Reactor Power 1MW, and sample contained in Teflon sample pouch)**

## Polyethylene Pellet

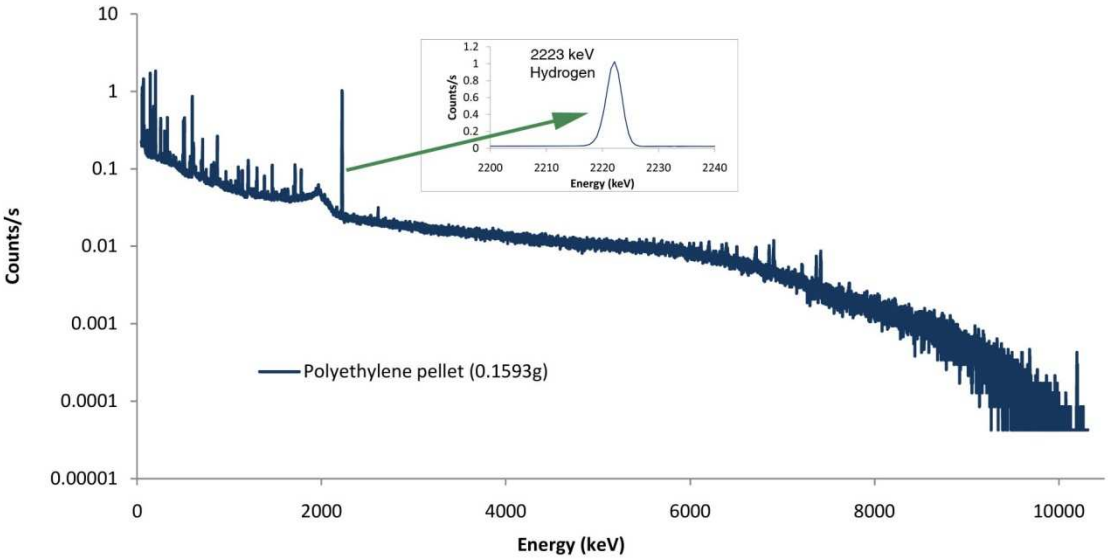


**Figure 7-51: PGNAA polyethylene Spectrum after improved detector collimator, (Reactor Power 1MW, and sample contained in Teflon sample pouch)**

**Sensitivities and Detection limits for 1633a Coal Fly Ash, and 1571 Orchard leaf Standards**

The measured sensitivities and detection limits for 1633a coal fly ash and 1571 orchard leaf standards were determined both before and after the improved detector collimator (Table 7-3 and Table 7-4). It is important to note that the count times for the data in Table 7-4 are approximately half the count times for the data in Table 7-3. Also, since the Detection limit was assumed to be $L_d = 3.29\frac{\sqrt{R_b/t}}{S}$ , the detection limit will change by a factor of $\sqrt{1/t}$ and therefore the detection limits should reduced by a factor of $\sqrt{1/2} \approx 0.71$ for a factor of 2 increase in count time. Since sensitivity is defined as $S = (counts/s)/mg$ the only change seen from a different count time would be a change in the relative error based on the total number of counts recorded, which is also what would be expected from a change in the background spectrum. A comparison of the ratio of the detection limits in Table 7-4 and Table 7-3 does not show a significant change in the detection level as illustrated in Figure 7-52. It appears that the detection was improved by the enhanced detector collimator such that the detection limits are equivalent to the old configuration with half the count time. However, the error in the measurements is large enough that longer count times should be performed to verify this.

These detection limits and sensitivities are approximately a factor 10 less sensitive than the results obtained at NIST for the same standards before their reactor was upgraded from 10MW to 20MW and their facility was reconstructed (Failey, Anderson, Zoller, & Gordon, 1979). The factor of ten better detection limits and sensitivities at NIST is a result of the factor of ten higher flux which increases gamma-ray production within the sample also by a factor of 10.

**Table 7-3: Orchard leaf, coal fly ash and polyethylene sensitivities, these values are based on measurements taken with reactor power at 1MW, and the live times associated with each measurement**

| (1.0213g sample with 44235 s count time) SRM 1571 Orchard Leaf | | | | |
|---|---|---|---|---|
| | Mass mg | Energy (KeV) | Sensitivity (counts/mg/s) | Detection limit (mg/g) |
| Cl | 0.75±0.03 | 517.07 | 0.076±0.003 | 0.37±0.05 |
| Cl | 0.75±0.03 | 785 & 788 | 0.457±0.019 | 0.065±0.008 |
| Cl | 0.75±0.03 | 1164 | 0.160±0.007 | 0.14±0.03 |
| K | 15.0±0.03 | 770 | 0.0275±0.0006 | 1.1±0.1 |
| Ca | 21.3±0.03 | 1942 | 0.0122±0.0002 | 2.3±0.3 |
| (1.015g sample with 43620s count time) SRM 1633a Coal Fly Ash | | | | |
| | Mass mg | Energy (KeV) | Sensitivity (counts/mg/s) | Detection limit (mg/g) |
| Mg | 4.6±0.1 | 585 | 0.054±0.001 | 0.44±0.09 |
| Si | 231±8 | 1273 | (5.6±0.2)E-04 | 25±14 |
| Si | 231±8 | 3539 | (1.40±0.05)E-03 | 8.5±4.7 |
| Si | 231±8 | 4934 | (8.90±0.03)E-04 | 12±9 |
| K | 19.1±0.6 | 77 | 0.027±0.001 | 0.75±0.17 |
| Ca | 11.3±0.1 | 1942 | 0.0075±0.0001 | 1.9±1.0 |
| Ti | 8.5±0.1 | 341.7 | 0.0717±0.0009 | 0.43±0.05 |
| Ti | 8.5±0.1 | 1382 | 0.0847±0.001 | 0.19±0.05 |
| Fe | 95±1 | 352 | 0.0075±0.0001 | 3.8±0.5 |
| Fe | 95±1 | 7120 & 7135 | 0.00395±0.00004 | 2.4±1.6 |
| Fe | 95±1 | 7631 & 7645 | 0.00299±0.00003 | 1.9±2.3 |
| Sm | 0.016±0.002 | 334 | 86.1±10.8 | (3.6±0.7)E-04 |
| Gd | 0.016±0.002 | 182 | 92±12 | (4.7±0.9)E-04 |
| Gd | 0.016±0.002 | 1185 | 18.0±2 | (9.4±3.7)E-04 |

**Table 7-4: Orchard leaf and coal fly ash sensitivities for improved detector collimator, these values are based on measurements taken with reactor power at 1MW, and the live times associated with each measurement**

| (1.0213g sample with 22363 s count time) SRM 1571 Orchard Leaf | | | | |
|---|---|---|---|---|
| | Mass mg | Energy (KeV) | Sensitivity (counts/mg/s) | Detection limit (mg/g) |
| B | 0.0400±0.007 | 477 | 97.1±0.2 | (5.6±0.4)E-04 |
| Cl | 0.75±0.03 | 517.07 | 0.107±0.004 | 0.27±0.10 |
| Cl | 0.75±0.03 | 785 & 788 | 0.369±0.015 | 0.082±0.027 |
| Cl | 0.75±0.03 | 1164 | 0.228±0.009 | 0.11±0.05 |
| K | 15.0±0.03 | 770 | 0.0266±0.005 | 1.0±0.4 |
| Ca | 21.3±0.03 | 1942 | 0.0069±0.001 | 4.6±1.5 |
| (1.015g sample with 21122 s count time) SRM 1633a Coal Fly Ash | | | | |
| | Mass mg | Energy (KeV) | Sensitivity (counts/mg/s) | Detection limit (mg/g) |
| B | 0.0400±0.0001 | 477 | 140±25 | (3.1±0.9)E-04 |
| Mg | 4.6±0.1 | 585 | 0.0408±0.0009 | 0.56±0.23 |
| Si | 231±8 | 1273 | (2.29±0.08)E-04 | 68±64 |
| Si | 231±8 | 3539 | (1.36±0.048) E-03 | 8.8±7.5 |
| Si | 231±8 | 4934 | (8.25±0.029)E-04 | 12±16 |
| K | 19.1±0.6 | 77 | 0.028±0.001 | 0.78±0.27 |
| Ca | 11.3±0.1 | 1942 | 0.0064±0.0001 | 2.39±2.24 |
| Ti | 8.5±0.1 | 341.7 | 0.0685±0.0008 | 0.40±0.10 |
| Ti | 8.5±0.1 | 1382 | 0.0703±0.0008 | 0.28±0.10 |
| Fe | 95±1 | 352 | 0.0101±0.0001 | 2.9±0.6 |
| Fe | 95±1 | 7120 & 7135 | 0.00356±0.00004 | 2.9±2.7 |
| Fe | 95±1 | 7631 & 7645 | 0.00269±0.0003 | 2.2±3.4 |
| Sm | 0.016±0.002 | 334 | 67.8±8.5 | (4.4±1.1)E-04 |
| Gd | 0.016±0.002 | 182 | 143±19 | (2.5±0.5)E-04 |
| Gr | 0.016±0.002 | 1185 | 13.8±1.8 | (1.4±0.7)E-03 |
| (0.1593g sample with 23446 s count time) Polyethylene | | | | |
| H | 22.753 | 2223 | 0.26595±0.00002 | 0.068±0.011 |

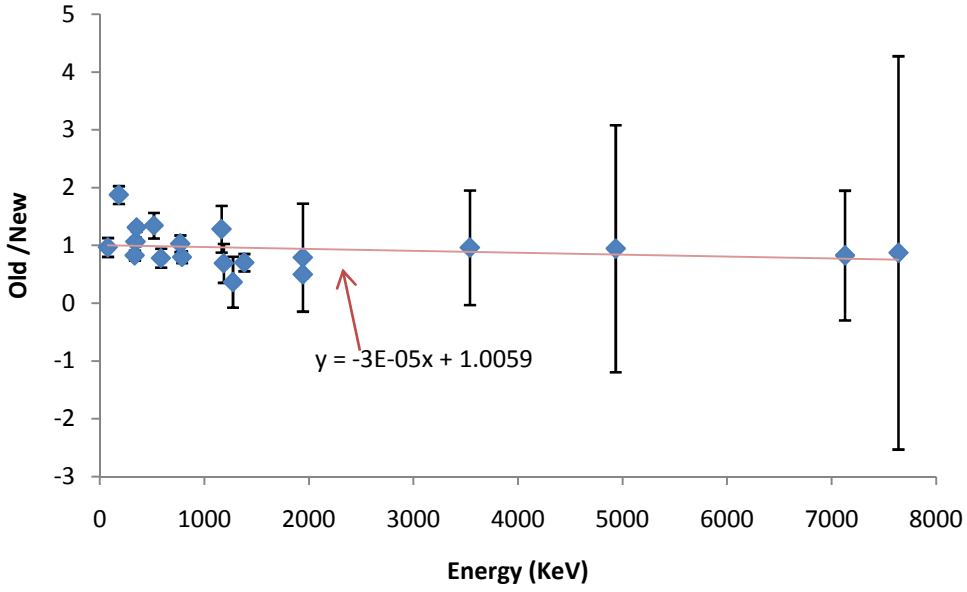


**Figure 7-52: Plot of the ratio of the detection limit before improved detector collimator and after improved detector collimator**

# 8. Conclusions and Future Work

A versatile PGNAA facility has been built, characterized, and put into operation at the Oregon State University TRIGA® reactor. This facility has a thermal neutron flux of 2.81E+7 ± 5.13E+5 neutrons/cm$^2$/s and a cadmium ratio of approximately 106 ± 3. When scaled by the reactor power, it has sensitivities and detection limits which are comparable to the PGNAA facilities at NIST, University of Texas, and Budapest. This facility not only will compliment many of the nuclear analysis methods currently used at the Oregon State University TRIGA® reactor, but it has also provided means for researchers to analyze substances such as B, H, and N which could not be detected with the standard instrumental nuclear analysis methods available to them prior to this instrument. Also, since PGNAA is nondestructive and the samples are analyzed outside the biological shield of the reactor, researchers will be able to perform elemental analysis on a much wider variety of samples, both including samples which cannot be put in the reactor for safety concerns and samples which would be damaged by the higher neutron flux at the reactor core.

Even though this facility is operational, there are still many improvements which can be made to increase the versatility and sensitivity of the instrument. Some of these improvements include the addition of lithium-fluoride or lithium-carbonate enriched in $^6$Li between the sample and the detector to reduce the thermal neutron interactions within the detector. There also may be more work which can be done to reduce the gamma and fast neutron back ground around the detector. This would increase the sensitivity of the instrument and extend the life of the germanium detector.

A flux monitor has been purchased which is going to be used to monitor the neutron beam. This will allow corrections to be made during an analysis which would correct for fluctuations of the neutron flux during an analysis. It will also allow for samples to be analyzed regardless of the reactor power.

In addition to the work which is being continued to improve the facilities prompt - gamma capabilities, efforts are planned to make modifications to the facility which would allow it to be used for Neutron Depth Profiling (NDP). NDP is used to determine the concentration as a function of depth for elements which produce charged particles upon interactions with neutrons. The charged particles are born at the position at which the interaction take place and lose energy as they travel through the sample. The concentration as a function of depth is determined based on the charged energy spectrum emitted by the sample, which is measured using a combination of surface barrier detectors. Even though the number of elements which can be measured with NDP is relatively small, these elements include B, N, Cl, and O which are very important in many biological and chemical systems. However, in order for NDP to be conducted, it is necessary know the elements present in the material and what the bulk composition of the material is in order to be able to know what the originating energy of the charged particles is, and to know how they will lose energy as they travel through the material. Since PGNAA can potentially provide this necessary information, this work is planned with the eventual goal of conducting both PGNAA and NDP simultaneously. Thus for every sample, there would be a prompt gamma spectrum that could be used to determine the elemental composition of the sample. This information, combined with the charged particle spectrum, could then potentially

be used to determine the concentration as a function of depth for the elements within the sample which produce charged particles. Even though NDP and PGNAA are both being used successfully at many facilities, a combining effort to perform both with the same facility has never been implemented. If this work were to be successfully completed, researchers at Oregon State University would have some of the best nuclear analysis techniques available, which could both enhance their work as well as provide additional opportunities for them to collaborate and make these facilities available to other researchers.

# 9. Appendix

Collimator MCNP Deck
c Created on: Saturday, January 27, 2007 at 12:38
c Cell definitions
1 1 -2.6989 1 -2 9 -10 imp:n=1 $six inch pipe
2 1 -2.6989 2 -3 9 -12 imp:n=1 $six to eight inch flange
3 1 -2.6989 3 -4 11 -12 imp:n=1 $eight inch pipe
4 2 -1 1 -2 -5 6 -7 8 10 imp:n=1 $outside collimator six inch end
5 2 -1 2 -4 -5 6 -7 8 12 imp:n=1 $outside collimator eight inch end
6 0 -1:4:5:-6:7:-8 imp:n=0 $outside box
7 3 -1.79E-06 1 -13 -9 imp:n=1 $inside six inch pipe
8 4 -9.8 13 -14 108 -9 imp:n=2 $Bismuth
9 4 -9.8 14 -15 109 -9 imp:n=2 $Bismuth
10 4 -9.8 15 -16 110 -9 imp:n=2 $Bismuth
11 4 -9.8 16 -17 111 -9 imp:n=2 $Bismuth
12 4 -9.8 17 -18 112 -9 imp:n=2 $Bismuth
13 4 -9.8 18 -19 113 -9 imp:n=2 $Bismuth
14 4 -9.8 19 -20 114 -9 imp:n=2 $Bismuth
15 4 -9.8 20 -21 115 -9 imp:n=2 $Bismuth
16 4 -9.8 21 -22 116 -9 imp:n=2 $Bismuth
17 4 -9.8 22 -23 117 -9 imp:n=2 $Bismuth
18 5 -11.34 23 -24 118 -9 imp:n=4 $Lead
19 5 -11.34 24 -25 119 -9 imp:n=4 $Lead
20 5 -11.34 25 -26 120 -9 imp:n=4 $Lead
21 5 -11.34 26 -27 121 -9 imp:n=4 $Lead
22 5 -11.34 27 -28 122 -9 imp:n=4 $Lead
23 5 -11.34 28 -29 123 -9 imp:n=4 $Lead
24 5 -11.34 29 -30 124 -9 imp:n=4 $Lead
25 5 -11.34 30 -31 125 -9 imp:n=4 $Lead
26 5 -11.34 31 -32 126 -9 imp:n=4 $Lead
27 5 -11.34 32 -33 127 -9 imp:n=4 $Lead
28 6 -3.98 33 -34 128 -9 imp:n=8$Sapphire
29 6 -3.98 34 -35 129 -9 imp:n=8$Sapphire
30 6 -3.98 35 -36 130 -9 imp:n=8$Sapphire
31 6 -3.98 36 -37 131 -9 imp:n=8$Sapphire
32 6 -3.98 37 -38 132 -9 imp:n=8$Sapphire
33 6 -3.98 38 -39 133 -9 imp:n=8$Sapphire
34 6 -3.98 39 -40 134 -9 imp:n=8$Sapphire
35 6 -3.98 40 -41 135 -9 imp:n=8$Sapphire
36 6 -3.98 41 -42 136 -9 imp:n=16$Sapphire
37 6 -3.98 42 -43 137 -9 imp:n=16$Sapphire
38 6 -3.98 43 -44 138 -9 imp:n=16$Sapphire
39 6 -3.98 44 -45 139 -9 imp:n=16$Sapphire
40 6 -3.98 45 -46 140 -9 imp:n=16$Sapphire
41 6 -3.98 46 -47 141 -9 imp:n=16$Sapphire
42 6 -3.98 47 -48 142 -9 imp:n=16$Sapphire
43 7 -2.7 48 -49 143 -9 imp:n=32 $Boral

```
   44 7 -2.7 49 -50 144 -9 imp:n=32 $Boral
   45 3 -1.79E-06 50 -51 -9 imp:n=64 $inside six inch pipe
c
   46 7 -2.7 51 -52 146 -9 imp:n=128 $Boral
   47 7 -2.7 52 -53 147 -9 imp:n=128 $Boral
   48 5 -11.34 53 -54 148 -9 imp:n=256 $Lead
   49 5 -11.34 54 -55 149 -9 imp:n=256 $Lead
   50 5 -11.34 55 -56 150 -9 imp:n=256 $Lead
   51 5 -11.34 56 -57 151 -9 imp:n=256 $Lead
   52 5 -11.34 57 -58 152 -9 imp:n=256 $Lead
   53 5 -11.34 58 -59 153 -9 imp:n=256 $Lead
   54 5 -11.34 59 -60 154 -9 imp:n=256 $Lead
   55 5 -11.34 60 -61 155 -9 imp:n=256 $Lead
   56 5 -11.34 61 -62 156 -9 imp:n=256 $Lead
   57 5 -11.34 62 -63 157 -9 imp:n=256 $Lead
   58 7 -2.7 63 -64 158 -9 imp:n=512 $Boral
   59 7 -2.7 64 -65 159 -9 imp:n=512 $Boral
   60 5 -11.34 65 -66 160 -11 imp:n=1024 $Lead
   61 5 -11.34 66 -67 161 -11 imp:n=1024 $Lead
   62 5 -11.34 67 -68 162 -11 imp:n=1024 $Lead
   63 5 -11.34 68 -69 163 -11 imp:n=1024 $Lead
   64 5 -11.34 69 -70 164 -11 imp:n=1024 $Lead
   65 5 -11.34 70 -71 165 -11 imp:n=1024 $Lead
   66 5 -11.34 71 -72 166 -11 imp:n=1024 $Lead
   67 5 -11.34 72 -73 167 -11 imp:n=1024 $Lead
   68 5 -11.34 73 -74 168 -11 imp:n=1024 $Lead
   69 5 -11.34 74 -75 169 -11 imp:n=1024 $Lead
   70 7 -2.7 75 -76 170 -11 imp:n=2048 $Boral
   71 7 -2.7 76 -77 171 -11 imp:n=2048 $Boral
c
   72 3 -1.79E-06 77 -78 -11 imp:n=4096 $inside eight inch pipe
   73 7 -2.7 78 -79 173 -11 imp:n=8192 $Boral
   74 7 -2.7 79 -80 174 -11 imp:n=8192 $Boral
   75 5 -11.34 80 -81 175 -11 imp:n=16384 $Lead
   76 5 -11.34 81 -82 176 -11 imp:n=16384 $Lead
   77 5 -11.34 82 -83 177 -11 imp:n=16384 $Lead
   78 5 -11.34 83 -84 178 -11 imp:n=16384 $Lead
   79 5 -11.34 84 -85 179 -11 imp:n=16384 $Lead
   80 5 -11.34 85 -86 180 -11 imp:n=16384 $Lead
   81 5 -11.34 86 -87 181 -11 imp:n=16384 $Lead
   82 5 -11.34 87 -88 182 -11 imp:n=16384 $Lead
   83 5 -11.34 88 -89 183 -11 imp:n=16384 $Lead
   84 5 -11.34 89 -90 184 -11 imp:n=16384 $Lead
   85 7 -2.7 90 -91 185 -11 imp:n=32768 $Boral
   86 7 -2.7 91 -92 186 -11 imp:n=32768 $Boral
c
   87 3 -1.79E-06 92 -93 -11 imp:n=32768 $inside eight inch pipe
   88 7 -2.7 93 -94 188 -11 imp:n=65536 $Boral
```

```
89 7 -2.7 94 -95 189 -11 imp:n=65536 $Boral
90 5 -11.34 95 -96 190 -11 imp:n=131072 $Lead
91 5 -11.34 96 -97 191 -11 imp:n=131072 $Lead
92 5 -11.34 97 -98 192 -11 imp:n=131072 $Lead
93 5 -11.34 98 -99 193 -11 imp:n=131072 $Lead
94 5 -11.34 99 -100 194 -11 imp:n=131072 $Lead
95 5 -11.34 100 -101 195 -11 imp:n=131072 $Lead
96 5 -11.34 101 -102 196 -11 imp:n=131072 $Lead
97 5 -11.34 102 -103 197 -11 imp:n=131072 $Lead
98 5 -11.34 103 -104 198 -11 imp:n=131072 $Lead
99 5 -11.34 104 -105 199 -11 imp:n=131072 $Lead
100 7 -2.7 105 -106 200 -11 imp:n=262144 $Boral
101 7 -2.7 106 -107 201 -11 imp:n=262144 $Boral
c
102 4 -9.8 13 -14 -108 imp:n=2 $Bismuth
103 4 -9.8 14 -15 -109 imp:n=2 $Bismuth
104 4 -9.8 15 -16 -110 imp:n=2 $Bismuth
105 4 -9.8 16 -17 -111 imp:n=2 $Bismuth
106 4 -9.8 17 -18 -112 imp:n=2 $Bismuth
107 4 -9.8 18 -19 -113 imp:n=2 $Bismuth
108 4 -9.8 19 -20 -114 imp:n=2 $Bismuth
109 4 -9.8 20 -21 -115 imp:n=2 $Bismuth
110 4 -9.8 21 -22 -116 imp:n=2 $Bismuth
111 4 -9.8 22 -23 -117 imp:n=2 $Bismuth
112 3 -1.79E-06 23 -24 -118 imp:n=4 $Helium
113 3 -1.79E-06 24 -25 -119 imp:n=4 $Helium
114 3 -1.79E-06 25 -26 -120 imp:n=4 $Helium
115 3 -1.79E-06 26 -27 -121 imp:n=4 $Helium
116 3 -1.79E-06 27 -28 -122 imp:n=4 $Helium
117 3 -1.79E-06 28 -29 -123 imp:n=4 $Helium
118 3 -1.79E-06 29 -30 -124 imp:n=4 $Helium
119 3 -1.79E-06 30 -31 -125 imp:n=4 $Helium
120 3 -1.79E-06 31 -32 -126 imp:n=4 $Helium
121 3 -1.79E-06 32 -33 -127 imp:n=4 $Helium
122 6 -3.98 33 -34 -128 imp:n=8 $Sapphire
123 6 -3.98 34 -35 -129 imp:n=8 $Sapphire
124 6 -3.98 35 -36 -130 imp:n=8 $Sapphire
125 6 -3.98 36 -37 -131 imp:n=8 $Sapphire
126 6 -3.98 37 -38 -132 imp:n=8 $Sapphire
127 6 -3.98 38 -39 -133 imp:n=8 $Sapphire
128 6 -3.98 39 -40 -134 imp:n=8 $Sapphire
129 6 -3.98 40 -41 -135 imp:n=8 $Sapphire
130 6 -3.98 41 -42 -136 imp:n=16 $Sapphire
131 6 -3.98 42 -43 -137 imp:n=16 $Sapphire
132 6 -3.98 43 -44 -138 imp:n=16 $Sapphire
133 6 -3.98 44 -45 -139 imp:n=16 $Sapphire
134 6 -3.98 45 -46 -140 imp:n=16 $Sapphire
135 6 -3.98 46 -47 -141 imp:n=16 $Sapphire
```

```
   136 6 -3.98 47 -48 -142 imp:n=16 $Sapphire
   137 3 -1.79E-06 48 -49 -143 imp:n=32 $Helium
   138 3 -1.79E-06 49 -50 -144 imp:n=32 $Helium
c
   139 3 -1.79E-06 51 -52 -146 imp:n=128 $Helium
   140 3 -1.79E-06 52 -53 -147 imp:n=128 $Helium
   141 3 -1.79E-06 53 -54 -148 imp:n=256 $Helium
   142 3 -1.79E-06 54 -55 -149 imp:n=256 $Helium
   143 3 -1.79E-06 55 -56 -150 imp:n=256 $Helium
   144 3 -1.79E-06 56 -57 -151 imp:n=256 $Helium
   145 3 -1.79E-06 57 -58 -152 imp:n=256 $Helium
   146 3 -1.79E-06 58 -59 -153 imp:n=256 $Helium
   147 3 -1.79E-06 59 -60 -154 imp:n=256 $Helium
   148 3 -1.79E-06 60 -61 -155 imp:n=256 $Helium
   149 3 -1.79E-06 61 -62 -156 imp:n=256 $Helium
   150 3 -1.79E-06 62 -63 -157 imp:n=256 $Helium
   151 3 -1.79E-06 63 -64 -158 imp:n=512 $Helium
   152 3 -1.79E-06 64 -65 -159 imp:n=512 $Helium
   153 3 -1.79E-06 65 -66 -160 imp:n=1024 $Helium
   154 3 -1.79E-06 66 -67 -161 imp:n=1024 $Helium
   155 3 -1.79E-06 67 -68 -162 imp:n=1024 $Helium
   156 3 -1.79E-06 68 -69 -163 imp:n=1024 $Helium
   157 3 -1.79E-06 69 -70 -164 imp:n=1024 $Helium
   158 3 -1.79E-06 70 -71 -165 imp:n=1024 $Helium
   159 3 -1.79E-06 71 -72 -166 imp:n=1024 $Helium
   160 3 -1.79E-06 72 -73 -167 imp:n=1024 $Helium
   161 3 -1.79E-06 73 -74 -168 imp:n=1024 $Helium
   162 3 -1.79E-06 74 -75 -169 imp:n=1024 $Helium
   163 3 -1.79E-06 75 -76 -170 imp:n=2048 $Helium
   164 3 -1.79E-06 76 -77 -171 imp:n=2048 $Helium
c
   165 3 -1.79E-06 78 -79 -173 imp:n=8192 $Helium
   166 3 -1.79E-06 79 -80 -174 imp:n=8192 $Helium
   167 3 -1.79E-06 80 -81 -175 imp:n=16384 $Helium
   168 3 -1.79E-06 81 -82 -176 imp:n=16384 $Helium
   169 3 -1.79E-06 82 -83 -177 imp:n=16384 $Helium
   170 3 -1.79E-06 83 -84 -178 imp:n=16384 $Helium
   171 3 -1.79E-06 84 -85 -179 imp:n=16384 $Helium
   172 3 -1.79E-06 85 -86 -180 imp:n=16384 $Helium
   173 3 -1.79E-06 86 -87 -181 imp:n=16384 $Helium
   174 3 -1.79E-06 87 -88 -182 imp:n=16384 $Helium
   175 3 -1.79E-06 88 -89 -183 imp:n=16384 $Helium
   176 3 -1.79E-06 89 -90 -184 imp:n=16384 $Helium
   177 3 -1.79E-06 90 -91 -185 imp:n=32768 $Helium
   178 3 -1.79E-06 91 -92 -186 imp:n=32768 $Helium
c
   179 3 -1.79E-06 93 -94 -188 imp:n=65536 $Helium
   180 3 -1.79E-06 94 -95 -189 imp:n=65536 $Helium
```

```
181 3 -1.79E-06 95 -96 -190 imp:n=131072 $Helium
182 3 -1.79E-06 96 -97 -191 imp:n=131072 $Helium
183 3 -1.79E-06 97 -98 -192 imp:n=131072 $Helium
184 3 -1.79E-06 98 -99 -193 imp:n=131072 $Helium
185 3 -1.79E-06 99 -100 -194 imp:n=131072 $Helium
186 3 -1.79E-06 100 -101 -195 imp:n=131072 $Helium
187 3 -1.79E-06 101 -102 -196 imp:n=131072 $Helium
188 3 -1.79E-06 102 -103 -197 imp:n=131072 $Helium
189 3 -1.79E-06 103 -104 -198 imp:n=131072 $Helium
190 3 -1.79E-06 104 -105 -199 imp:n=131072 $Helium
191 3 -1.79E-06 105 -106 -200 imp:n=262144 $Helium
192 3 -1.79E-06 106 -107 -201 imp:n=262144 $Helium tally
193 8 -1.21E-03 107 -208 -205 imp:n=262144 $inside
c  194 8 -1.21E-03 107 -208 -205 203 imp:n=262144 $tally2
c  195 8 -1.21E-03 107 -208 -205 204 imp:n=262144 $tally3
c  196 8 -1.21E-03 107 -208 -206 205 imp:n=262144 $tally4
c  197 8 -1.21E-03 107 -208 -207 206 imp:n=262144 $tally5
198 8 -1.21E-03 107 -208 -11 205 imp:n=262144 $tally6

c   Surface definitions
1      px 0  $front plane
2      px 148.209  $front center plane
3      px 148.479  $back center plane
4      px 321.199  $back plane
5      pz 30.48  $top plane
6      pz -30.48  $bottom plane
7      py 30.48  $rear plane
8      py -30.48  $face plane
9     cx  6.985  $inside six inch pipe
10     cx  7.62  $outside six inch pipe
11     cx  9.8425  $inside eight inch pipe
12     cx  10.16  $outside eight inch pipe
13     px  80
14     px  81
15     px  82
16     px  83
17     px  84
18     px  85
19     px  86
20     px  87
21     px  88
22     px  89
23     px  90
24     px  91
25     px  92
26     px  93
27     px  94
28     px  95
```

```
  29    px 96
  30    px 97
  31    px 98
  32    px 99
  33    px 100
  34    px 101
  35    px 102
  36    px 103
  37    px 104
  38    px 105
  39    px 106
  40    px 107
  41    px 108
  42    px 109
  43    px 110
  44    px 111
  45    px 112
  46    px 113
  47    px 114
  48    px 115
  49    px 116
  50    px 117
c
  51    px 134.47875
  52    px 135.47875
  53    px 136.47875
  54    px 137.47875
  55    px 138.47875
  56    px 139.47875
  57    px 140.47875
  58    px 141.47875
  59    px 142.47875
  60    px 143.47875
  61    px 144.47875
  62    px 145.47875
  63    px 146.47875
  64    px 147.47875
  65    px 148.479
  66    px 149.47875
  67    px 150.47875
  68    px 151.47875
  69    px 152.47875
  70    px 153.47875
  71    px 154.47875
  72    px 155.47875
  73    px 156.47875
  74    px 157.47875
  75    px 158.47875
```

```
  76    px  159.47875
  77    px  160.47875
c
  78    px  213.959375
  79    px  214.959375
  80    px  215.959375
  81    px  216.959375
  82    px  217.959375
  83    px  218.959375
  84    px  219.959375
  85    px  220.959375
  86    px  221.959375
  87    px  222.959375
  88    px  223.959375
  89    px  224.959375
  90    px  225.959375
  91    px  226.959375
  92    px  227.959375
c
  93    px  306.19875
  94    px  307.19875
  95    px  308.19875
  96    px  309.19875
  97    px  310.19875
  98    px  311.19875
  99    px  312.19875
  100     px  313.19875
  101     px  314.19875
  102     px  315.19875
  103     px  316.19875
  104     px  317.19875
  105     px  318.19875
  106     px  319.19875
  107     px  320.199
  108     cx  6.359648
  109     cx  6.3438936
  110     cx  6.3281392
  111     cx  6.3123848
  112     cx  6.2966304
  113     cx  6.280876
  114     cx  6.2651216
  115     cx  6.2493672
  116     cx  6.2336128
  117     cx  6.2178584
  118     cx  6.202104
  119     cx  6.1863496
  120     cx  6.1705952
  121     cx  6.1548408
```

```
  122     cx  6.1390864
  123     cx  6.123332
  124     cx  6.1075776
  125     cx  6.0918232
  126     cx  6.0760688
  127     cx  6.0603144
  128     cx  6.04456
  129     cx  6.0288056
  130     cx  6.0130512
  131     cx  5.9972968
  132     cx  5.9815424
  133     cx  5.965788
  134     cx  5.9500336
  135     cx  5.9342792
  136     cx  5.9185248
  137     cx  5.9027704
  138     cx  5.887016
  139     cx  5.8712616
  140     cx  5.8555072
  141     cx  5.8397528
  142     cx  5.8239984
  143     cx  5.808244
  144     cx  5.7767352
c 145     cx  5.7609808
c
  146     cx  5.517122381
  147     cx  5.501367981
  148     cx  5.485613581
  149     cx  5.469859181
  150     cx  5.454104781
  151     cx  5.438350381
  152     cx  5.422595981
  153     cx  5.406841581
  154     cx  5.391087181
  155     cx  5.375332781
  156     cx  5.359578381
  157     cx  5.343823981
  158     cx  5.328069581
  159     cx  5.312315181
  160     cx  5.296560781
  161     cx  5.280806381
  162     cx  5.265051981
  163     cx  5.249297581
  164     cx  5.233543181
  165     cx  5.217788781
  166     cx  5.202034381
  167     cx  5.186279981
  168     cx  5.170525581
```

```
  169      cx  5.154771181
  170      cx  5.139016781
  171      cx  5.123262381
 c 172     cx  5.107507981
c
  173      cx  4.249198423
  174      cx  4.233444023
  175      cx  4.217689623
  176      cx  4.201935223
  177      cx  4.186180823
  178      cx  4.170426423
  179      cx  4.154672023
  180      cx  4.138917623
  181      cx  4.123163223
  182      cx  4.107408823
  183      cx  4.091654423
  184      cx  4.075900023
  185      cx  4.060145623
  186      cx  4.044391223
 c 187     cx  4.028636823
c
  188      cx  2.796022413
  189      cx  2.780268013
  190      cx  2.764513613
  191      cx  2.748759213
  192      cx  2.733004813
  193      cx  2.717250413
  194      cx  2.701496013
  195      cx  2.685741613
  196      cx  2.669987213
  197      cx  2.654232813
  198      cx  2.638478413
  199      cx  2.622724013
  200      cx  2.606969613
  201      cx  2.591215213
 c 202     cx  2.575460813
  203      cx  0.5
  204      cx  1.5
  205      cx  2.591215213
  206      cx  4.37
  207      cx  6.25
  208      px  321.199
c    Bismuth lead sapphire Boral section

c    Material definitions
m1   13027            1  $Aluminium
m2   8016          0.3333  $water
     1001          0.6667
```

```
m3    2004          1  $Helium
m4    83209         1  $Bismuth
m5    82207           1  $lead
m6    13027             2  $Sapphire
      8016              3
m7    5010        0.06014  $Boral
      13027       0.93986
m8    7014        0.755268  $Air
      8016        0.231781
      18000       0.012827
      6012        0.000124
c     source definitions
sdef sur=1 pos=0 0 0 rad=d1 par=1 erg=d2 axs=1 0 0 vec=1 0 0
si1 0 6.985
si2 H 6.5 7
sp2 d 0 1
f4:n  193 198    $cells
e0    .5e-3 8
wwp:n 5 3 5 0 0 0
wwe:n  1.0000E+02
wwn1:n    5.0000E-01  0.0000E+00  4.3853E-03  5.0851E-01  4.9031E-03
       -1.0000E+00  2.4533E-01  1.6616E-02  1.5389E-02  1.5537E-02
        1.1779E-02  1.0920E-02  1.0890E-02  7.5573E-03  6.3493E-03
        5.9701E-03  5.1099E-03  5.7707E-03  5.7852E-03  4.5015E-03
        4.6147E-03  4.3541E-03  4.1893E-03  3.6710E-03  3.4746E-03
        3.2024E-03  2.4043E-03  2.1664E-03  1.6152E-03  1.3264E-03
        1.0869E-03  9.6887E-04  9.1913E-04  8.2198E-04  8.8687E-04
        8.2258E-04  5.7516E-04  5.3160E-04  6.1688E-04  6.0545E-04
        8.7961E-04  1.0738E-03  3.4789E-03  2.1985E-03  3.4810E-05
        0.0000E+00  0.0000E+00  0.0000E+00  0.0000E+00  5.9768E-03
        5.5860E-03  0.0000E+00  5.9242E-03  5.7233E-03  1.4028E-03
        1.9687E-03  1.6067E-03  0.0000E+00  5.2508E-03  6.3010E-03
        6.8224E-03  6.2217E-03  3.0376E-03  5.2781E-03  0.0000E+00
        5.6983E-03  5.6095E-03  5.2243E-03  4.6085E-03  4.2595E-03
        1.4076E-03  1.2693E-06  0.0000E+00  0.0000E+00  0.0000E+00
        0.0000E+00  0.0000E+00  0.0000E+00  0.0000E+00  0.0000E+00
        0.0000E+00  7.7538E-04  1.0338E-04  9.2483E-05  6.8094E-05
        1.8277E-05  1.2743E-07  6.5111E-06  1.6720E-06  9.9787E-07
        7.9891E-07  6.8880E-07  5.3910E-07  4.7648E-07  4.1240E-07
        3.6509E-07  3.9356E-07  4.1124E-07  4.3776E-07  8.3571E-07
        1.5010E-06  4.5509E-03  3.9557E-03  3.4726E-03  3.0886E-03
        2.6910E-03  2.3477E-03  2.0537E-03  1.8210E-03  1.6068E-03
        1.3919E-03  1.2218E-03  1.1791E-03  1.1055E-03  1.0245E-03
        9.6701E-04  9.0893E-04  8.5491E-04  8.0992E-04  7.7023E-04
        7.3871E-04  6.9657E-04  5.6204E-04  4.7036E-04  3.9021E-04
        3.3032E-04  2.7972E-04  2.2609E-04  1.9035E-04  1.5913E-04
        1.3135E-04  1.0963E-04  9.0259E-05  7.4092E-05  6.0801E-05
        4.9786E-05  3.7856E-05  3.3150E-05  7.5146E-06  6.8322E-06
```

```
      5.8576E-06  5.5178E-06  4.9871E-06  4.6783E-06  4.4360E-06
      4.1526E-06  4.0165E-06  3.6830E-06  3.5047E-06  3.3001E-06
      3.0418E-06  2.8371E-06  2.5736E-06  2.4000E-06  2.2092E-06
      2.1296E-06  2.0002E-06  1.9155E-06  1.8346E-06  1.6801E-06
      1.5495E-06  1.4543E-06  1.3774E-06  1.2978E-06  1.8335E-07
      1.7757E-07  1.7070E-07  1.6562E-07  1.5967E-07  1.5594E-07
      1.5359E-07  1.5013E-07  1.4650E-07  1.4261E-07  1.3805E-07
      1.3454E-07  1.2859E-07  1.2436E-07  2.4756E-08  2.4609E-08
      2.4621E-08  2.4358E-08  2.4041E-08  2.3758E-08  2.1952E-08
      2.1349E-08  2.0730E-08  2.0173E-08  1.9661E-08  1.8931E-08
      1.8248E-08  1.7562E-08  1.7203E-08  7.2514E-06
nps   30000000
print 126
```

# 10.Bibliography

Advanced Measurement Technology, Inc. (2007). *Neutron Radiation Damage in HPGe Detectors*. Retrieved October Wednesday, 2008, from ortec-online: http://www.ortec-online.com/detectors/photon/a8.htm

Anderson, D. L., Faily, M. P., Zoller, W. H., Walters, W. B., Gordon, G. E., & Lindstrom, R. M. (1981). Facility For Non-Destructive Analysis for major and Trace Elements using Neutron-Capture Gamma-Ray Spectrometry. *Journal of Radioanalytical Chemistery* , 97-119.

Audi, W. a. (2003). The AME2003 atomic mass evaluation. *Nuclear Physics A* , 337-676.

Batentschuk, M., Winnacker, A., Schuwartz, K., & Trautmann, C. (2007). Storage Efficiency of BaFBr:Eu2+ image plates irradiated by swift hevy ions. *Journal of Luminescence* , 40-44.

Belgya, T., Revay, Z., & Molnar, G. L. (2004). Gamma-Ray Background at the Budapest PGAA Facility. *Journal of Radioanalytical and Nuclear Chemistery* , 181-191.

Binney, D. S. (Fall 2006). *Radiophysiscs Lecture Notes.*

Brookhaven National Laboratory. (2008). *Evaluated Nuclear Data File (ENDF) Retrieval & Plotting*. Retrieved December 12, 2008, from National Nuclear Data Center: http://www.nndc.bnl.gov/sigma/index.jsp

Brookhaven National Laboratory. (n.d.). *Thermal Neutron Capture Gamma-Rays*. Retrieved January 25, 2009, from NNDC National Nuclear Data Center: http://www.nndc.bnl.gov/capgam/index.html

Chasman, C., Jones, k. W., & Ristinen, R. A. (1965). Fast Neutron Bombardment of a Lithium-Drifted Germanium Gamma-Ray Detector. *Nuclear Instruments and Methods* , 1-8.

Crystal Systems. (2007). 27 Congress street, MA, USA.

Currie, L. A. (1968). Limits for Qualitative Detection and Quantitative Determination. *Application to Radiochemistery* , 586-593.

Duderstadt, J. J., & Hamilton, L. J. (1976). *Nuclear Reactor Analysis.* Ann Arbor, Michigan: John Wiley & Sons, Inc.

Dzubay, T. G. (1977). *X-Ray Fluorescence Analysis of Environmental Samples.* Ann Arbor, MI: Ann Arbor Science Publisher INC.

E. Amaldi, O. D. (1935). Artificial Radioactivity Produced by Neutron Bombarment-II. *Proceedings of the Royal Society of London* , 522-558.

ELK Premium Products for Security & Automation. (n.d.). *ELK Premium Products for Security & Automation*. Retrieved February 1, 2009, from http://www.elkproducts.com/products/elk-924.htm

*ENDFPLOT: online graph plot for neutron cross section*. (2008, September 16). Retrieved September 16, 2008, from ENDFPLOT: online graph plot for neutron cross section: http://atom.kaeri.re.kr/endfplot.shtml

Failey, M. P., Anderson, D. L., Zoller, W. H., & Gordon, G. E. (1979). Neutron-Capture Prompt Gamma-ray Activation Analysis for Multielemental Determination in Complex Samples. *Analytical Chemistry* , 2209-2221.

FUJIFILM Global. (2008). *Basics if IP*. Retrieved December 17, 2008, from FUJIFILM Global: http://www.fujifilm.com/products/life_science/si_imgplate/whatis03.html

G. A. Bartholomew, A. D. (1967). Compendium of Thermal Neutron Capture Gamma-Ray Measurments. *Nuclear Data Section A* , 367-650.

G. L. Molnar, Z. R. (2000). The new prompt gamma-ray catalogue for PGAA. *Applied Radiation and Isotopes* , 527-533.

G. Shirane, S. M. (2002). *Neutron Scattering with a Triple-Axis Spectrometer: Basic Techniques.* Cambridge University Press, 2002.

Gadd, M. S. (2007). *Characterization of the Oregon State University Neutron Radiography Facility.* Las Alamos, New Mexico: Las Alamos National Laboratory.

Hamermesh Bernard, H. V. (1952). Neutron Capture Gamma-Ray Spectra from the Elements z=17-30 and z=45-57. *Physical Review* , 916-919.

I. E. Stamatelatos, S. M. (2000). Sapphire filter thickness optimization in neutron scattering instruments. *REVIEW OF SCIENTIFIC INSTRUMENTS* , 70-73.

Jurney, E. T., & Motz, H. (1966). Gamma-Ray Spectrum From Pb-204(n,gamma)Pb-205. *Nuclear Physics A* , 351-365.

Kapetka, P. A., Rowe, J. M., & Williams, R. E. (2005). Cold Neutrons at NIST. *Nuclear Engineering and Technology* , 427-432.

Keisuke Sueki, K. K. (1996). Nondestructive Determination of Major Elements in a Large Sample by Prompt Gamma Ray Neutron Activation Analysis. *Analytical Chemistry* , 2203-2209.

KFKI Atomic Energy Research Institute. (n.d.). *KFKI Reactor Department*. Retrieved December 11, 2008, from http://www.kfki.hu/brr/indexen.htm

L. V. Groshev, A. M. (1959). *Atlas of Gamma-Ray Spectra from Radiative Capture of Thermal neutrons.* Los Angeles, California: Pergaman Press INC.

Lambar, S. M., & Isenhour, T. L. (1968). Neutron Capture Gamma-Ray Activation Analysis Using Lithium Drift Germanium Semiconductor Detectors. *Analytical Chemistry* , 1990-1994.

Lambard, S. M., Isenhour, T. L., Heintz, P. H., Woodruff, G. L., & Wilson, W. E. (1967). Neutron-Capture Gamma-Ray Activation Analysis. Design of Apparatus for Trace Analysis. *International Journal of Applied Radiation and Isotopes* , 15-22.

Lea, D. E. (1934). Combination of Proton and Neutron. *Nature* , 24.

M. Adib, M. K. (2002). On the use of bisumth as a neutron filter. *Radiation Physics and Chemistry* , 81-88.

Mackey, E. A., Anderson, D. L., Liposky, P. J., Lindstrom, R. M., Chen-Mayer, H., & Lamaze, G. P. (2004). New Thermal Neutron Prompt Gamma-ray Activation Analysis Instrument at the ational Institute of Standards and Technology Center for Neutron Reasearch. *Nuclear Instruments and Methods in Physics Research B* , 426-440.

Molnar, G. L. (2004). *Hand Book of Prompt Gamma Activation Analysis.* Boston/ London: Kluwer Academic Publishers.

Oregon State University. (2008). *Safety Analysis Report for the Oregon State University TRIGA® Reactor.* In review.

R. C. Greenwood, J. H. (1965). *Prompt Gamma Rays from Radiative Capture of Thermal Neutrons (Vols. 1 & 2).* US Atomic Energy Commission & IIT Research Institute .

Revey, Z., Harrison, R. K., Alvarez, E., Biegalski, S. R., & Landsberger, S. (2007). Construction and Characterization of the Redesigned PGNAA Facility at The University of Texas at Austin. *Nuclear Instruments and Methods in Physics Research A* , 611-618.

Sears, V. F. (1989). *Neutron Optics.* New York oxford: Oxford University Press.

Skoro, G. P., Anicin, I. V., Kukoc, A. H., Krmpotic, D., Adsic, P., Vukanovic, R., et al. (1992). Environmental Neutrons as Seen by a Germanium Gamma-Ray Spectrometer. *Nuclear Instruments & Methods in Physics Research (Section A)* , 333-336.

Svikis, V. D. (1963). Dense Lithium Fluoride for Gamma-Ray-Free Neutron Shielding. *Clear Instruments and Methods* , 93-105.

t. (n.d.).

T. L. Isenhour, G. H. (1966). Modulation Technique for Neutron Capture Gamma Ray Measurements in Activation Analysis. *Analytical Chemistry* , 162-167.

Thomas W. Raaudorf, R. C. (February 1984). Performance of Reverse Electrode PHGe Coaxial Detectors After Light Damage by Fast Neutrons. *IEE Transactions on Neuclear Science, Vol. NS-31, No. 1* , 253-257.

U.S.NRC. (n.d.). *10 CFR 20.1003*. Retrieved October 24, 2008, from http://www.nrc.gov/reading-rm/doc-collections/cfr/part020/part020-1003.html

W. G. Lussie, J. L. (1965). The Measurement and Utilization of Neutron-Capture Gamma Radiation. *Modern Trends in Activation Analysis*, (pp. 194-199). College Station, Texas, U.S.A.

X-5 Monte Carlo Team. (2005). *MCNP - A General Monte Carlo N-Particle Transport Code, Version 5.* Oak Ridge: Los Alamos National Laboratory.